DOCTOR OF PHILOSOPHY

Quantitative assessment of elasticity properties of skin using surface acoustic wave (SAW) method

Li, Chunhui

Award date:
2014

DOCTOR OF PHILOSOPHY

Quantitative assessment of elasticity properties of skin using surface acoustic wave (SAW) method

Chunhui Li

2014

University of Dundee

Quantitative assessment of elasticity properties of skin using surface acoustic wave (SAW) method

Mrs Chunhui Li

BSc (Hons) MSc

School of Engineering, Physics and Mathematics

College of Art, Science and Engineering

University of Dundee,

Dundee,

Scotland.

Abstract

Mechanical properties are important tissue parameters of skin that are useful for understanding skin patho-physiology, and aiding disease diagnosis and treatment. They are indicators of functional changes and pathological variations in the micro-structure.

This research thesis studies the intersection of acoustics, optics and biomechanics for skin mechanical properties measurement. Surface acoustic wave (SAW) is induced and applied to a range of different tissue mimicking phantom models, Thiel cadavers and *in vivo* human skin. Different optical systems, i.e. low coherence interferometer and phase sensitive optical coherence tomography (PhS-OCT), are employed to detect the SAW. The Young's moduli and thicknesses of model layers are assessed by the analysis of the wave phase velocity curves. The PhS-OCT detection system can also provide the real time high resolution depth-resolved cross-sectional microstructure imaging of the interrogated sample to assist the elasticity evaluation of the heterogeneous tissue.

Results prove that the novel combination of optical imaging technology with SAW method is able to assess the elasticity change in both axial and transverse directions in soft material. It can be used to evaluate the mechanical properties of single, double-layer soft tissue mimicking phantoms and different sites of human skin *ex vivo* and *in vivo* non-invasively. This study also demonstrates that the SAW method can be successfully utilized to map the elasticity of soft heterogeneous tissues quantitatively. The results represent an important step towards the development of SAW method as a clinical diagnosis tool in dermatology, and may offer potential in diagnostic and therapeutic clinical applications.

Declaration

I hereby declare that this thesis is my own work and effort and that it has not been submitted anywhere for any award. Where other sources of information have been used, they have been acknowledged.

……..

Chunhui Li

Certificate

This is to certify that Chunhui Li has done this research under my supervision and that she has fulfilled the conditions of Ordinance 39 of the University of Dundee, so that she is qualified to submit for the Degree of Doctor of Philosophy.

……..……

Dr. Zhihong Huang

Copyright

Acknowledgements

This is a great opportunity to express my respect to everybody who contributed to this dissertation. I owe my gratitude to my adviser, Dr Zhihong Huang, for giving me the opportunity to involve into such an exciting project and the chance to work in the laboratory with leading facilities, also the cares of my life. I also thank Professor Ruikang K. Wang very much, for his support, guidance, and mentoring through every step of this work. Both of my advisers lighted up the way of conducting research for me, especially from their expertise in both engineering and medicine.

I am pleased to thank the workmates in both of the laboratories in University of Dundee and University of Washington. Dr Yi Wang, Mrs Jia Qin, Mr Lin An, Mr Zhongwei Zhi, Dr Guozhong Liu, Dr Suzan Dziennis, Dr Roberto Reif and Dr Yumin Liu from University of Washington Bio-photonics and Imaging Laboratory as a great collaborators, who went through many studies with me and shared their wealth of knowledge. I also thank Mr Sinan Li, Mr Shaozhen Song, Mr Cheng Wei, and Mrs Yuting Ling in Optical lab in University of Dundee. They have been great team members and friends. I thank Professor Steven Jacques for his one short meeting, which is of great importance for all of my work. I also thank Dr Tong Shen, Professor Murray Johnstone for the opportunity for fruitful months of collaborative work in eye research. I would like to record my gratitude to all friends. Many thanks go to Mr Xu Xiao for all the helps in life. I also thank Mr Peng Qian, Mr Rui Cao, Miss Zhen Qiu, Mr Yongqiang Qiu, Mrs Doudou Xu, Mr Pengjue Fan, Miss Yi Cheng and Mr Jiang You and all the friends.

Last and most, I thank my mother and father for their support and help throughout my Ph.D. study. My parents deserve the most and special mention for their unshakable support and love. I would like to express my deepest gratitude to them. I thank my husband, Mr Guangying Guan, for his love, dedication, persistent confidence, understanding and all the help in work.

Table of Content

List of Figures

List of Tables

List of Abbreviations and Symbols

BC	Basal keratinocytes
CSLM	Confocal Scanning Laser Microscopy
CW	Continuous Wave
CWT	Continuous wavelet transform
C_L	Velocity of longitudinal wave
C_R	Velocity of Rayleigh wave
C_S	Velocity of shear wave
d	Diameter
DFT	Discrete Fourier Transform
DP	Dermal papilae
E	Young's Modulus
EMD	Empirical mode decomposition
f	Frequency
F	Nuclei folds
FD-OCT	Frequency domain optical coherence tomography
FE	Finite Element
FEM	Finite Element Model
FFT	Fast Fourier Transform
HHT	Hilbert-Huang transform
HTS	High-temperature superconducting
I_0	Irradiation of laser pulse
IMF	Intrinsic mode functions
IOP	Intraocular pressures
k	Wave vectors
MM	Malignant melanoma
MRE	Magnetic resonance elastography
MRI	Magnetic Resonance Imaging
NDE	Non-Destructive Evaluation

NDT	Non-Destructive Testing
Nd:YAG	Neodymium-doped yttrium aluminium garnet
OCT	Optical Coherence Tomography
OCE	Optical coherence elastography
OPD	Optical path delay
OPL	Optical path length
P-wave	Longitudinal wave
PA	Photo acoustic
PAM	Photoacoustic imaging
PD	Papillary dermis
PhS-OCT	Phase sensitive optical coherence tomography
t	Time
r	Radius
s	Strain
S-wave	Shear wave
SASW	Spectral analysis of SAW
SAW	Surface Acoustic Wave
SC	Stratum Corneum
SNR	Signal to noise ratio
SSc	Systemic Sclerosis
STFT	Short time discrete Fourier transform
TD-OCT	Time domain optical coherence tomography
TR	Time of repetition
λ	Wave length
μ_a	Absorption coefficient
ν	Poisson's ratio
ρ	Density
σ	Stress
φ	Phase change

Chapter 1: Introduction

1.1 Motivation and research objectives

The alteration of mechanical properties with the change of tissue condition is commonly observed in tissue pathologies, such as in skin disorders. Thus, assessing skin mechanical properties is useful in improving our understanding of skin patho-physiology, which will aid medical diagnosis and treatment of, e.g., skin cancer and scleroderma [1-3]. Skin cancer prognosis is important because treatment at its early stages can improve five-year survival rate and increase the chance for cure [4, 5]. For example, malignant melanoma (MM) is the most dangerous in the skin cancers, accounting for the majority (75%) of deaths. In early stages of skin cancer, the lesion is often confined within the epidermis and dermis (1 mm thickness), with relatively higher Young's modulus than normal skin tissues. A diagnosis at this stage can improve the survival rate up to 90%-100% [6]. However, if diagnosed at a later stage, the tumour will have already invaded subcutaneous fat with a drastic increase of stiffness, and become fatal [7-9]. Tissue geometry and stiffness are therefore important parameters for the clinical prognosis of skin diseases. Currently in the clinic, diagnosis of skin diseases largely depends on visual assessment by a trained dermatologist. However, quantitative information on the skin mechanical properties is necessary. To meet this requirement, a sensitive, non-destructive and non-invasive method that is capable of assessing the skin mechanical properties as well as geometry information is needed.

A number of elastography technologies have been developed recently for qualitative and quantitative assessment of tissue mechanical properties [10-15]. The main idea in elastography is to use a sensitive device to quantify the image of mechanical disturbance, which is induced directly or indirectly by a mechanical stimulation, such as compression, vibration, or acoustic radiation [10]. Ultrasound elastography [11-13] and magnetic resonance elastography (MRE) [14, 15] are the most common methods in medical diagnosis that involve either ultrasound or magnetic resonance imaging (MRI) to measure the passive tissue disturbances, from which the mechanical properties of tissue are obtained. Despite their success in cardiac applications, these methods are difficult to quantify skin mechanical properties because of their low spatial resolution, which is not sufficient to detect small lesion in thin skin layers. In addition, the methods described above tracking shear wave that propagates within the body and thus it may present

limitations in the assessment of material surface, and it is still problematic for shear wave method to provide the Young's modulus of different thin layers of skin tissue.

The surface acoustic wave (SAW) technology has been used in industrial applications such as analysing surface structure, composition, geometry, roughness, flatness and elastic properties of metallic specimens [16-20]. SAW method is mainly used to evaluate the mechanical properties of materials because it has advantages to quantitatively assess Young's modulus. SAW has great superiority in characterisation of skin because: 1) the domain wave energy locates at near-surface region; 2) the propagation of SAW in layered materials shows a dispersive behaviour, where dispersion means that different frequency components have different phase velocities which penetrate into different depths of the tissue. The phase velocity values are directly related to the Young's modulus, then, the quantitative elasticity information of skin layers the SAW propagate into can be obtained. To detect the SAW, the most common method is to employ ultrasound transducer [21], which requires physical contact with the sample. This requirement leads to a number of drawbacks: the sensing area is limited by the transducer, wave energy leakage occurs at the tissue-transducer boundary, and wave distortion will be caused by the weight of the transducer on the sample, *etc.* To mitigate these problems, a preferred method is to use a non-contact and non-destructive approach to detect the SAW. One of such methods is optical interrogation. Optical interrogation method has been widely used because it is non-contact and remote, therefore no surface loading. The sensitivity of optical measuring system is inherently high which allows detection of significantly small displacement. Also it provides a broad detection bandwidth. As a remote sensing approach, at the same time it provides access to the samples in a hostile environment and generally not sensitive to surface orientation.

The aim of this research project presented in this thesis is to develop innovative non-invasive systems which combine impulse stimulated SAW method and optical interrogation method that allow the rapid functional characterization of different layers of soft tissue mimicking phantoms, and *ex vivo* and *in vivo* human skin tissue. Phantoms are made using different concentrations of agar solution and different layer thickness to mimic the elastic properties typically found in skin. The SAW are generated by shaker or a Q-switched laser pulse, and detected by optical approaches, including low coherence

interferometry and phase sensitive optical coherence tomography (PhS-OCT). The behaviours of SAW in the soft materials are observed and analysed. Dispersion phase velocity curves are calculated to obtain the elastic properties from well-defined layers, including different kinds of agar phantoms, different skin sites of cadavers and *in vivo* human skin, which exhibit different mechanical properties. The system also provides depth-resolved microstructure information of the interrogated sample to assist the elasticity evaluation of the heterogeneous tissue.

1.2 Outline of Thesis

Chapter 2 of this thesis introduces the structure and properties of each layer of human skin. Skin diseases, including skin cancers and scleroderma are introduced. The effects that these diseases have on the mechanical and geometrical properties of the individual layers of skin are discussed. Since the aim of the project is to provide diagnosis and treatment monitor of such skin diseases, this chapter introduces current available methods employed in the field of dermatology for the diagnosis of skin disease. Advantages and disadvantages between different methods are discussed.

Chapter 3 presents an overview of wave motions in elastic solids. Different kinds of waves, including longitudinal wave and shear wave are introduced as well as their applications in medical applications. The theory of SAW is presented in details along with some applications in industry and medicine. In this chapter fundamental characterization technique of SAW is also discussed, which forms the basis of this research.

Chapter 4 provides an overview of finite element method (FEM) and simulation procedures used in this research. An FE model is developed to simulate the generation and propagation of SAW, which is generated by a laser pulse, in both hard and soft solid materials. The experimental systems which include both generation and detection of SAW are developed, including a Q-switched laser pulse and a mechanical shaker for SAW generation, and low coherence interferometry and PhS-OCT for SAW detection. SAW obtained from experiments are compared with that from finite element simulation for cross validation, to prove the generation and detection system function properly for the next experimental procedures.

Chapter 5 introduces signal processing procedures including frequency analysis, de-noise of SAW signals and calculation of phase velocity. In this chapter different kinds of de-noised methods will be compared, including average, wavelet de-noising and empirical mode decomposition (EMD) de-noising. In this chapter inversion procedures of SAW signals to elasticity information are presented, in order to characterise the property of layers in human skin and to monitor changes in the mechanical and geometrical changes of these layers due to skin disease.

Chapter 6 analyses the behaviour of SAW in heterogeneous materials, in both axial and transverse directions, to simulate the localised lesion in skin tissues. Skin is layered material with the alteration of axial elasticity. Skin lesions are usually localized, with transverse elasticity alteration. In this chapter, different kinds of agar phantoms will be manufactured to mimick skin and skin lesions. The aim is to prove the SAW is sensitive for the elasticity change in both of the directions, thus prove the SAW is promising in dermatology applications.

Chapter 7 presents the SAW application in dermatology. The experiments involve different skin sites of *in vivo* human skin. By the signal processing it is able to obtain the phase velocity curves of SAW obtained from human skin. In addition, it is desirable that the mechanical properties of the tissue are mapped, to provide direct visualization of the tissue stiffness for ease of biomedical diagnosis. To fulfil this requirement, this chapter also reports on the use of SAW method, coupled with PhS-OCT, to enable the SAW elastography.

Chapter 8 presents the conclusions of this work along with some suggestions for further study.

1.3 List of publications

Peer-reviewed full Journal Articles

1. **Chunhui Li**, Shaozhen Song, Guangying Guan, Ruikang K Wang, Zhihong Huang, “Frequency dependence of laser ultrasonic SAW phase velocities measurements”, Ultrasonics, 53 (1) 191-195 (2013).

2. **Chunhui Li**, Guangying Guan, Zhihong Huang, Murray Johnstone, and Ruikang Wang, "Noncontact all-optical measurement of corneal elasticity," Opt. Lett. 37, 1625-1627 (2012).
3. **Chunhui Li**, Guangying Guan, Sinan Li, Zhihong Huang, and Ruikang K. Wang, "Evaluating elastic properties of heterogeneous soft tissue by surface acoustic waves detected by phase-sensitive optical coherence tomography" J. Biomed. Opt. 17, 057002 (2012).
4. **Chunhui Li**, Guangying Guan, Xi Cheng, Zhihong Huang, and Ruikang K. Wang, "Quantitative elastography provided by surface acoustic waves measured by phase-sensitive optical coherence tomography", Optics Letters, Vol. 37, Issue 4, pp. 722-724 (2012).
5. **Chunhui Li**, Guangying Guan, Roberto Reif, Zhihong Huang, and Ruikang K. Wang, "Determining elastic properties of skin by measuring surface waves from an impulse mechanical stimulus using phase-sensitive optical coherence tomography", Journal of the Royal Society Interface, vol. 9 no. 70 831-841, (2012).
6. **Chunhui Li**, Sinan Li, Guangying Guan, Cheng Wei, Zhihong Huang, and Ruikang K. Wang, "A comparison of laser ultrasound measurements and finite element simulations for evaluating the elastic properties of tissue mimicking phantoms", Optics and laser technology, 44(4), 866-871 (2012).
7. Yi Wang, **Chunhui Li**, and Ruikang Wang. "Non-contact photoacoustic imaging by using a low coherence interferometer as the acoustic detector" Optics Letters 36(20), 3975-3977 (2011).
8. **Chunhui Li**, Zhihong Huang, Ruikang K. Wang, "Elastic properties of soft tissue-mimicking phantoms assessed by combined use of laser ultrasonics and low coherence interferometry", Optics Express Vol. 19, Iss. 11, pp. 10153–10163 (2011).

Conference Papers:

1. **Chunhui Li**, Guangying Guan, Zhihong Huang, Ruikang Wang,"Quantitative elastography of skin and skin lesion using phase-sensitive OCT (PhS-OCT) and surface wave method", Proc. SPIE 8213, Optical Coherence Tomography and

Coherence Domain Optical Methods in Biomedicine XVI, 82132E (February 9, 2012); doi:10.1117/12.910985.

2. **Chunhui Li**, Zhihong Huang, Ruikang K. Wang, "Characterisation of skin layer properties using laser-generated surface acoustic waves validated by FEM method", BIOS SPIE Photonics West 2011, Paper 7898-30.
3. **Chunhui Li**, Sinan Li, Zhihong Huang, Wenbin Xu, "Skin Thermal Effect by FE Simulation and Experiment of Laser Ultrasonics", Applied Mechanics and Materials 2010, Vols. 24-25, pp 281-286.

Chapter 2: Tissue imaging and characterisation methods for skin and skin diseases

2.1 Introduction

The development of a non-invasive method of characterising mechanical properties of skin has several clinic applications, since the majority of pathological changes result in change of elastic properties and/or morphology of the affected skin layers. This chapter provides a brief introduction to skin structure and skin diseases. In addition, different technologies employed and currently in development for the *in vivo* characterisation of skin and soft tissues in general, including imaging and the mechanical properties measurements are reviewed and compared.

2.2 Structure of human Skin

The skin is the body's largest organ comprising of between 15% and 20% of the total body weight, with a surface area of about 1.8m^2 in the adult human [24]. It has significant functions, including: 1) providing a strong physical barrier from the environment, 2) controlling the inward and outward passage of water and chemicals, 3) providing electrolytes and various substances while protecting against toxic agents, ultraviolet radiation, mechanical insults and micro-organisms. It also helps control body temperature and stores water, fat and vitamin D [24-30]. Skin can be roughly classified into three layers: the epidermis, dermis and subcutaneous fat. A schematic diagram of the skin layers is shown in Figure 2.1.

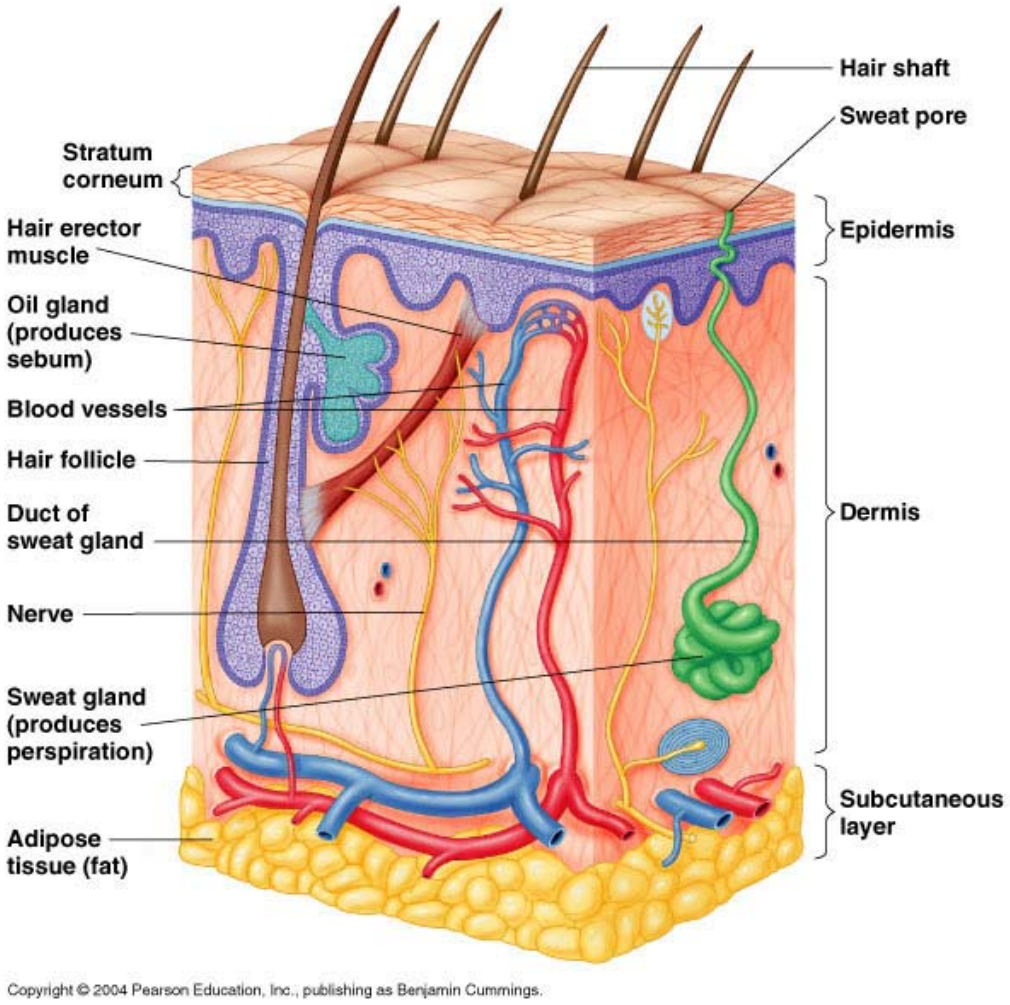

Fig. 2.1 Anatomy of the skin, showing the epidermis, dermis, and subcutaneous fat tissue [31]

The epidermis is located on the surface of skin. It serves as the physical and chemical barrier between the interior body and exterior environment [26-30]. The thickness of the epidermis ranges from 0.07mm to 0.12mm. However it is only 0.05 mm thick on the eyelids, and in the soles of the feet and palms of the hand it can range from 0.8mm up to 1.4mm. In general it is considered as 0.08-0.1mm. The outermost layer of the epidermis is known as stratum corneum, which is consisting of corneocytes. The purpose of the stratum corneum is to form a barrier to protect underlying tissue from infection, dehydration, chemicals and mechanical stress.

The dermis contains a number of different structures including hair follicles, blood vessels, smooth muscle glands, nerves and lymphatic tissue [24, 30]. It consists of loose connective tissue made up of collagen, elastin and reticular fibres. The main functions of the dermis are to regulate temperature and to supply the epidermis with nutrient-saturated blood. The body's water mostly is stored within the dermis [25, 27, 28]. The dermis varies in thickness, ranging from 0.6 mm on the eyelids to 3 mm on the back, palms and soles. The average thickness of the dermis is considered to be 1mm. It is also thicker on the posterior of the body than the anterior, and is thicker in men than in women.

The third layer, with fat and connective tissue, is called the subcutaneous layer. It is the innermost layer of the skin, which consists of a network of collagen and fat cells. The subcutaneous fat layer functions as an insulator, a shock-absorber, the inner organs protector, and also an energy reserve for the body. The nerves, blood vessels, hair follicles, and lymph vessels also cross through this layer [26-28]. The thickness of the subcutaneous fat layer varies throughout the body and from person to person. The mechanical functions of the subcutaneous adipose tissue include allowing the overlying skin to move as a whole in both vertical and horizontal direction, and the attenuation and dispersion of externally applied pressure.

Although the stratum corneum in epidermis is believed to be stiffer than dermis, the contribution of the epidermis to the mechanical properties of full thickness of skin is usually neglected [26]. The dermis together with the subcutaneous fat layer gives skin its toughness and elasticity. This property of human skin is attributed to the intra and intermolecular cross-links of collagen, elastic and reticulin fibres which are embedded in tissue substance.

2.3 Skin diseases

Skin disease is an illness of the skin, such as a bacterial or fungal infection, a cancer, or an allergic reaction [31], some of these diseases can be very serious and even fatal while some diseases are annoying to the patient, some are disfiguring and some are not really visible and do not have a large impact on the lives of those affected. The majority of pathological changes in the skin result in a change in the elastic properties, especially the stiffness of the tissues and/or thickness of the affected skin layers.

The diagnoses for many dermatological conditions are carried out by clinical observation and palpation. For example, Rodnan score evaluates patient's skin thickness rated by pinching and summing the scores for different skin areas of the body in system sclerosis assessment [32]. In complex and serious skin conditions, e.g. skin cancer, a skin biopsy is often used which is followed by a histological analysis to determine the condition in order to resolve any ambiguities. However when it is required to detect very small changes in the thickness and mechanical properties of the skin layers, measuring by *in vitro* methods does not give an accurate picture of what is happening in the body *in vivo* as the properties of the tissue change when removed from the body's environment. It is hoped that by utilising novel imaging methods a non-intrusive, non-invasive method of accurately measuring skin properties *in vivo* will be developed.

Two kinds of serious skin diseases are discussed here, including skin cancer and scleroderma. Both of the diseases significantly change the skin elasticity, which can be served as ideal target diseases of this study.

2.3.1 Skin cancer

Currently, the incidences of skin cancer, including melanoma, basal cell skin cancer and squamous cell skin cancer are rising dramatically. Between 2 and 3 million non-melanoma skin cancers and 132,000 melanoma skin cancers occur globally each year [33]. The mortality rate of basal cell and squamous cell carcinoma are around 0.3 percent. In comparison the mortality rate of melanoma is 15-20 percent [33, 34]. Even though it is much less common, malignant melanoma is responsible for 75 percent of all skin cancer-related deaths [4, 5, 9]. In fact, between 40 percent and 50 percent of people who suffer from skin cancers develop non-melanoma cancer, such as basal cell carcinoma and squamous cell carcinoma. These kinds of skin cancers rarely spread to other parts of the body, and are highly treatable when diagnosed in its early stages [35-39]. Staging of skin cancer is determined by the size and depth of the cancerous tissue and whether the tumour has certain "high-risk" features. Stages of skin cancers include [4, 5]:

- **Stage 0:** In the squamous cell or basal cell layer of the epidermis, abnormal cells can be found. These abnormal cells may become cancerous and spread to nearby normal tissue, with only transverse direction, but not grow deeper into other layers of the skin. If not treated, the cancer may grow deeper into the skin.

- **Stage I:** Cancer has formed and begins to affect the dermis layer. The growth is as large as 2 centimetres wide (more than three-quarters of an inch or about the size of a peanut). It may have one high-risk feature.
- **Stage II:** The growth is larger than 2 centimetres wide.
- **Stage III:** The cancer has invaded below the skin to muscle, cartilage, or bone. Cancer cells also have begun to spread to lymph nodes nearby. But they have not spread to other places in the body.
- **Stage IV:** The cancer cells have spread to other parts of the body. Squamous cell cancer and melanoma can spread to lymph nodes and other organs but basal cell cancer rarely spreads to other parts of the body.

In early stage of skin cancers (stage 0 and I), the lesion is often confined within epidermis and dermis (1 mm thickness), whilst the stiffness of infected layer begins to change compared to the normal skin tissue, such as an increase in the stiffness of squamous cell carcinomas and malignant melanoma, and a decrease in the stiffness of basal cell carcinomas [37-39]. The stiffness of lesions will not change much after stage III. Early diagnosis and treatment is necessary which can improve the survival rate up to 90%-100% at stage I and 50%-85% at stage II [4, 35, 36]. However, if diagnosed at a later stage, the tumor will invade subcutaneous fat with a drastic change of stiffness, and become fatal.

2.3.2 Scleroderma

Scleroderma is a variable, slow and long-term disorder of the immune system, blood vessels and connective tissue [40-44]. There are two types of scleroderma which are classified as localised scleroderma and systemic scleroderma. The systemic form are also referred to as systemic sclerosis (SSc) and includes subcategories such as “diffuse” and “limited” depending on the degree and location of scleroderma.

The diffuse form of scleroderma involves the symmetric thickening of the skin of the extremities, face, trunk (chest, back, abdomen, or flanks) which can rapidly progress to hardening after an early inflammatory phase. Organs can be affected in diffuse form, include the oesophagus, bowels, lung with scarring (fibrosis), heart and kidneys. The limited form of the disease tends to be confined to the skin on the fingers and face. The

skin changes and other feature of the disease tend to occur more slowly than in the diffuse form.

Skin affected by scleroderma show impaired skin mechanical properties such as reduced extensibility and increased stiffness. There are three phases of skin involvement that can be identified in systemic sclerosis, which will generally follow one another as the disease progresses. These are: oedematous phase, indurative phase and atrophic phase.

In the oedematous phase the initial symptoms are “tight” or “puffy” fingers. These symptoms can be either only a sensation, or accompanied by visible swelling. These swellings usually become more obvious and constant as the disease progresses, although this varies in degree. Either pitting or non-pitting oedema is present in fingers and can affect the dorsum of hands, forearms, legs, feet, and face. Such oedema may last indefinitely, and are typically painless.

In the indurative phase the oedema is replaced by thickened and tight skin. Along with the thickening of the skin the affected areas become shiny and taut and tightly adhere to the subcutis. During this phase the dermis becomes markedly thickened, but the epidermis is thinned, leading to a loss of skin creases and the hair follicles, sebaceous glands and sweat glands. The thickening of the skin indirectly impairs the mobility of muscles, joints and tendons.

Skin thickening and tightness are the only major diagnostic criterion used to measure disease progression in early disease also permits the diagnostic distinction between limited and diffuse scleroderma. Some of the techniques that are available for the evaluation of skin thickness are the Rodnan skin score or the UK scleroderma Group’s score [32], however these methods are subject to inter and intra- observer error as they are dependent on the expertise of the individual. Research in this area has been significantly impeded by the inability to monitor skin with any degree of precision. Therefore there is a need for a reliable technique not only to assess the extent and degree of skin thickening but also to recognise the different stages of the disease.

2.4 Mechanical properties of soft tissue

In soft tissues, important parameters of mechanical properties include elasticity (Young’s modulus), Poisson ratio and density. The Poisson’s ratio and density do not vary much, as it is usually in the range of 0.490 to 0.499 as biological soft tissues are usually

uncompressible [28-30], and the corresponding values of density are 920 to 1060 kg/m^3 [28-30]. The elasticity varies with different kinds of soft tissues (as shown in Table 2.1). It is one of the most important parameters as it reveals the stiffness of the tissue, thus indicating the pathological conditions.

Table 2.1 Young's modulus of various types of human tissue from literature

Tissue	Type	E (kPa)	Tissue	Type	E (kPa)
Breast	Unspecified	29 [45]	Kidney	Unspecified	10 [46]
		21 – 23 [47]			6 [47]
	Adipose	19 [48]	Liver	Unspecified	13 [49]
	Glandular	33 [48]			10 – 17 [50]
	Fibrous	110 [48]			7 – 10 [47]
		1.8 [51]			1 – 3 [52]
Muscle	Unspecified	14 – 16 [47]			0.4 - 1.7 [53]
		10 – 40 [52]		Normal	10 [56]
		7 – 57 [55]			0.6 - 1.1 [56]
		1.2 – 1.8 [53]		Focal nodular	1.2 - 2.5 [56]
	Intercostal	100 [54]		Hyperplasia Chronic Hepatitis	35 [49]
	Cardiac (systole)	100 [55]			
	Intercostal	100 [54]		Cirrhosis	52 [49]

Destructive testing is most traditional way to understand the mechanical properties and behaviours of a material. As a result, material stress-strain curve can be obtained. A typical stress-strain curve is shown in Fig. 2.2. Here, Stress is the external force acting on the object per unit area. Strain is the result of a stress, defined as the change in length per unit length. At the beginning phase of tension test of soft tissue, it can be observed so called toe region. Typical strain value of toe region is ranging from 0-1.5% [56]. In this region,

the relation between stress and strain is nonlinear and the slope is increasing with increased loading. The reason for the increasing slope is the straightening of the wave-like collagen fibrils.

After the collagen fibrils are completely straightened begins the elastic region. In this region, the stress and strain are linearly related and the slope of the curve is called the Young's modulus of tissue. Thus, the Young's modulus (E) is defined as:

$$E = \frac{\sigma}{\varepsilon} = \frac{F/A}{\Delta L/L_i} \tag{2-1}$$

where $\sigma = F/A$ is the stress, F is the external force applied to the cross-sectional area A, and $\varepsilon = \Delta L/L_i$ is the strain. The unit Young's modulus is Newton per square metre (Nm^{-2}) or Pascal (Pa). In the elastic range, all changes of a tissue are reversible, i.e. if the stress is removed tissue returns to the original strain. The linear region of stress-strain curve is usually used for an accurate estimation of the tissue elasticity, where strain (ε) is controlled lower than 5% [56]. Thus, material would be kept safe without fail.

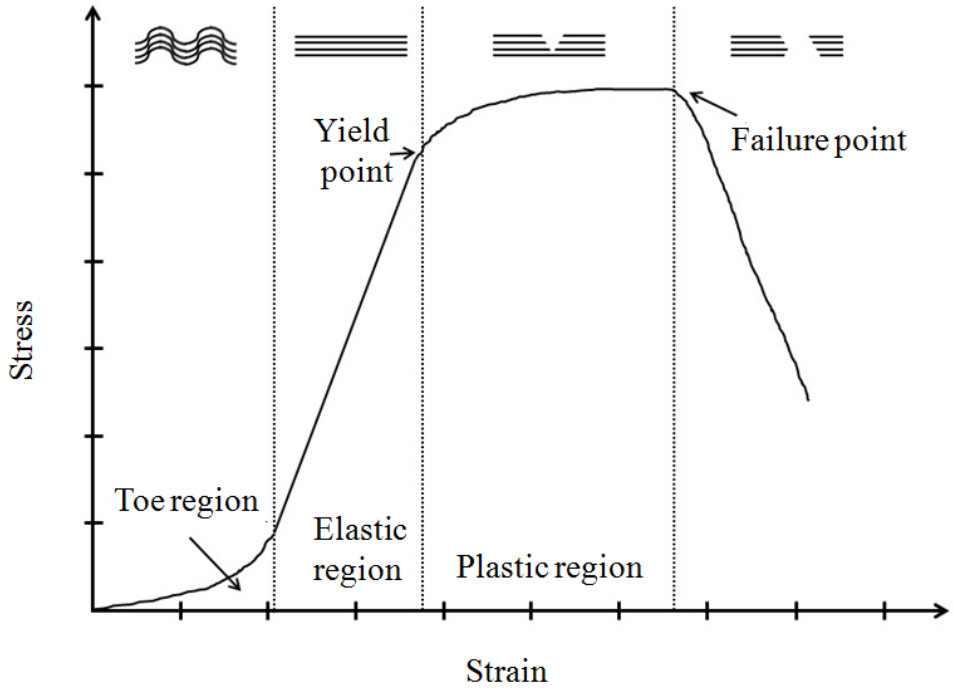

Fig. 2.2 Typical stress-strain relation in soft biological tissues [56]

When the stress is further increased from the elastic region, the slope of the curve changes and the plastic region begins, with the yield point separates elastic region and

plastic region of the graph. After the yield point tissue begins to experience destructive changes. In the plastic region irreversible changes have occurred in a tissue and it does not return to the original shape when the stress is completely removed. After the plastic region, failure of the tissue occurs. Strain and stress of tissue disappear. The location of the breakdown is called the failure point.

Skin behaves as a non-homogeneous, anisotropic, non-linear viscous-elastic material subjected to pre-stress with the experimentally obtained Young's modulus of the layers varying considerably. The mechanical properties of skin depend on the nature and organization of [59, 60]:

- Dermal collagen and elastic fibres network;
- Water, proteins and macromolecule embedded in the extracellular matrix;
- Factors like individual's age, body site, gender, race, exposure to UV irradiation, the use of creams and, health and nutritional status.

A number of techniques have been developed to detect the mechanical properties of human skin, which are generally based on stretching, traction, indentation, torsion or suction. Tangential traction method is used to determine the biomechanics of finger pad tissue [61]. A mechanical model under suction was used to characterize initial stress, Young's modulus, and index of non-elasticity of skin [62]. A twistometer was used to determine human skin-related mechanical properties [63]. Strain-stress relationships were studied to determine the role of elastin in single-axis extension method [64−67]. These techniques have some disadvantages: 1) except for extension method, only qualitative elasticity information was provided, quantitative information (true Young's moduli) were not available; 2) stretching and extension are not applicable to *in vivo* human skin elasticity measurement. Other techniques like traction and torsion lead strong deformation of skin and bring uncomfortableness; 3) skin were treated as homogeneous material, no layer or localized information was analysed.

There are lacks of techniques in non-destructive, localised and quantitative mechanical properties measurements of different skin layers *in vivo*. Thus currently in clinic, the diagnosis of skin diseases largely depends on visual assessment and palpation performed by a trained dermatologist; however, palpation results vary from person to person. There are often conditions where there is a clinical need for quantitative information on the skin

mechanical properties. Elastography begin to attract medical application from last decade. The main idea of this technology is to combine imaging modalities with different mechanical stimulations to generate tissue responses in the form of displacement that can be subsequently measured, so that mechanical properties may be evaluated and mapped with anatomic information of the biological tissue. Different tissue imaging and elastography techniques will be reviewed in the next section.

2.5 Techniques used for tissue imaging and characterisation

Various *in vivo* tissue imaging techniques have been developed for imaging tissue in a less time consuming way and without the necessity of taking biological biopsies. Non-invasive imaging of has several applications in dermatology including the determination of tumour margins prior to any surgery, tumour staging and the evaluation of non-tumour lesions and diseases of the skin. The selection of a suitable skin characterisation or imaging technique is required. Due to variations in the skin at different parts of the body and variations due to disease, any technique should ideally be capable of monitoring skin thickness from skin surface to a few millimetres with a resolution in the order of tens of microns in order to differentiate sub-layers and variations in thickness of the layers.

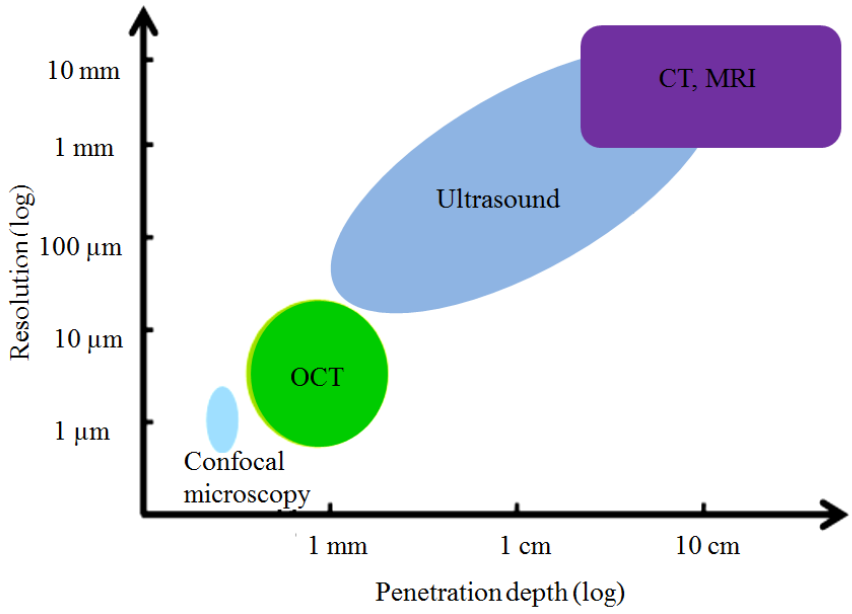

Fig. 2.3 Resolution and penetration of different imaging modalities [68]

Currently, the most popular approaches to image tissue include ultrasound imaging, high-resolution magnetic resonance imaging (MRI), optical coherence tomography and confocal microscopy, etc. The resolution and the penetration depth of the approaches are shown in Fig. 2.3.

2.5.1 Current skin imaging techniques

2.5.1.1Ultrasound imaging

Ultrasonic technique in medicine is a widely accepted tool aiding the diagnosis and treatment of a variety of medical conditions. The advantages including being non-invasive, inexpensive and inherently safe. Ultrasound can be used to image the skin and measure its thickness [69-71]. Typical diagnostic sonography operates in the frequency range of 2 to 18 MHz with the choice of frequency chosen as a trade-off between the spatial resolution of the technique and the imaging depth of the technique.

There are four main methods that are used in medicine for the presentation of data in imaging techniques namely the A-scan, B-scan, M-scan and Doppler mode. The A-scan is the simplest form of presentation of data and consists of a display of the amplitude of echoes against distance. The B-scan or brightness scan is made up of a number of A-scans and results in the production of a pictorial display of the area under inspection. It is produced by moving the transducer probe over the body so that the body is viewed from a range of angles resulting in a range of brightness points. These are then automatically correlated with information relating to the position and orientation of the probe building a 2-D picture of the body. The M-scan is repeated A-scans in a time period. Doppler Ultrasound takes advantage of the Doppler Effect the assessment and measurement of flow and relative velocity can be measured.

The physical principle of an ultrasound scanner is the emission of high frequency acoustic waves, generated from electrical signals in a piezo-electric ultrasound transducer. An alternating electric field causes thickness variations in of the piezo-electric material. When ultrasound waves travel through tissues, part of them transmit to deeper structures, part of them reflect back to the transducer as echoes, part of them scatter, or transform to heat. For imaging purposes, we are mostly interested in the echoes reflected back to the transducer. A change in the acoustic impedance of the tissue causes some of the sound to

be reflected back to the transducer at the interface between different tissues in the skin, whilst the rest of the energy continues to the next interface. The amount of sound being reflected depends on the acoustic impedance differences between the materials. A large difference causes a large reflection. The sound emission is pulsed, indicating that the equipment switches automatically and very rapidly between emission of sound and the registration of sound coming back to the same transducer from the object being studied. The result is a train of pulses returning to the transducer. The time lag between emitted and reflected sound waves is a measure for the thickness of the skin. It depends on the physical distance between the interfaces and the tissue material, and can be converted into a distance once the speed of the sound is known. Estimates of the sound velocity in skin are: stratum corneum 1550 m/s; epidermis 1540 m/s; dermis 1580 m/s and subcutaneous fat 1440 m/s. As an average for normal full-thickness skin, 1577 m/s can be used [69, 70].

If the ultrasound pulse encounters reflectors whose dimensions are smaller than the ultrasound wavelength, or when the pulse encounters a rough, irregular tissue interface, scattering occurs. In this case, echoes reflected through a wide range of angles result in reduction in echo intensity. However, the positive result of scattering is the return of some echo to the transducer regardless of the angle of the incident pulse.

As ultrasound pulses travel through tissue, their intensity is reduced or attenuated. This attenuation is the result of reflection and scattering and also of friction-like losses. Longer path length and higher frequency waves result in greater attenuation. Attenuation also varies among body tissues, with the highest degree in bone, less in muscle and solid organs, and lowest in blood for any given frequency. Fluid-containing structures attenuate sound much less than solid structures so that the strength of the sound pulse is greater after passing through fluid than through an equivalent amount of solid tissue.

The ultrasound frequency decides the resolution and penetration depth of the imaging. Proper selection of transducer frequency is important for providing optimal image resolution in diagnostic ultrasound. High-frequency ultrasound waves with short wavelength generate images of high axial resolution. Increasing the number of waves of compression and rarefaction for a given distance can more accurately discriminate between two separate structures along the axial plane of wave propagation. However, high-frequency waves are more attenuated than lower frequency waves for a given

distance; thus, they are suitable for imaging mainly superficial structures. Conversely, low-frequency waves with long wavelength offer images of lower resolution but can penetrate to deeper structures due to a lower attenuation. For this reason, it is best to use high-frequency transducers (up to 10–15 MHz range) to image superficial structures and low-frequency transducers (2–5 MHz) for imaging the deep tissue.

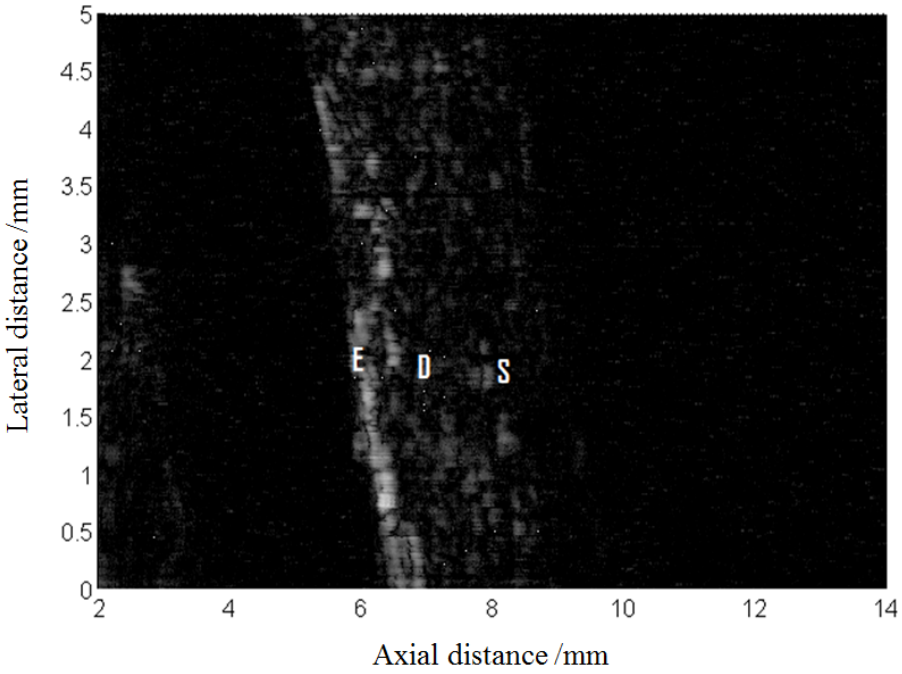

Fig. 2.4 B-scan of the different layers of a section of forearm from high frequency ultrasound imaging system with 50MHz; E: epidermis, D: dermis and S: subcutaneous fat

Recently, high frequency ultrasound imaging system, which has the ultrasound frequency over 15 MHz, is developed for high resolution imaging of skin tissue. Ultrasound waves of 15 MHz can penetrate deep enough to visualise the subcutaneous fat, while a 50 MHz ultrasound wave allows a better and detailed study of the epidermis layer. Frequencies from 15 to 20 MHz provide a good compromise between resolution and imaging depth to visualize the entire skin. Generally, 20 MHz scanners have a lateral resolution of 0.15-0.35 mm and an axial resolution of 0.05 mm in skin. The imaging depth is typically 15-25 mm [1, 11-13, 70, 71].

By moving the transducer over the skin, a two-dimensional ultrasound image can be obtained. The one dimensional pulse trains are processed electronically to obtain a cross-sectional image of the skin (Fig. 2.4).

2.5.1.2 High-resolution magnetic resonance imaging (MRI)

MRI is based principally on sensitivity to the presence and properties of water. The properties and amount of water in the human body differs in different tissues and pathological conditions, which changes are reflected in the obtained MR image. This makes MRI extremely sensitive diagnostic tool. MRI is mainly concerned with the Hydrogen nucleus, which consists of a single proton. Without external magnetic field, the spins have random direction. When the spins are exposed to an external magnetic field, they align with the direction of the external field. Magnetic field strength (with the unit T) is one of the key dynamics that contributes to production of higher quality images, thinner slice thickness and potentially earlier detection of pathology. When an electromagnetic field is exposed to stable spin system, it brings these spins from the equilibrium and energy can be introduced into such a stable spin system. This is called the resonance condition. MR signal rapidly fades and thus cause a return to the stable state present before excitation. Different receiving coils are designed for detecting the spin fading procedures of different parts of body, thus imaging the different amount of Hydrogen nucleus which can represent the tissue structure.

As a non-invasive modality, MRI is attractive for *in vivo* skin imaging. *In vivo* skin imaging has been investigated at 0.5T, 1.5T, 2T, and 2.4T. One feasibility study (36 volunteers) at 3T has been recently conducted [72-74]. To achieve high resolution, small (typically 1-inch-diameter) surface receiver coils are used. A typical image of skin under a 3T MRI imaging system can be found in Fig. 2.5.

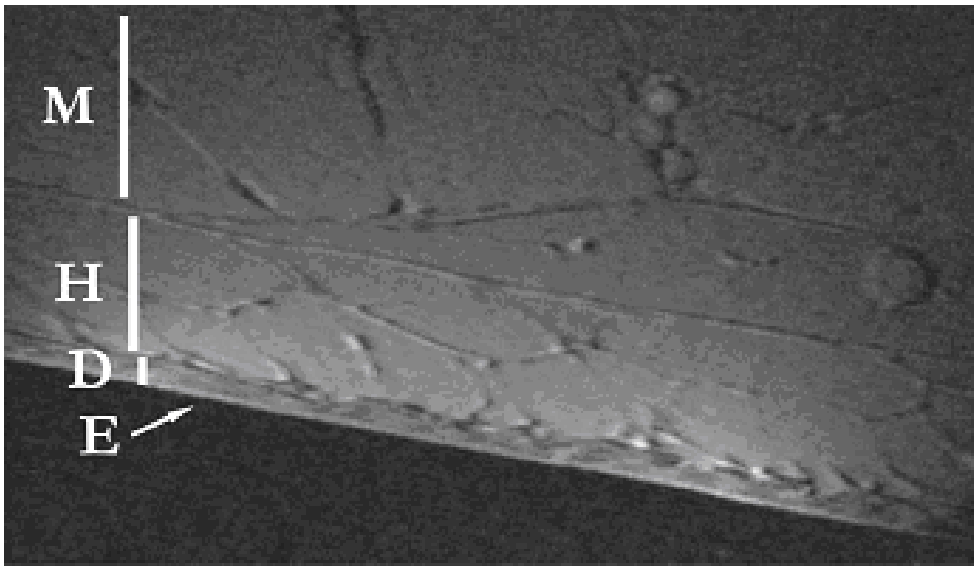

Fig.2.5 At 3 T (female, 23 years old), in 6 min using a GRE sequence, the following structures can be recognized: E: epidermis; D: dermis; H: hypodermis; M: muscle [75].

Querleux [72] adapted a standard MR scanner to enable epidermis investigation. He obtained an axial resolution in the order of 35-70μm and was therefore able to differentiate the epidermis, dermis and subcutaneous fat and a thickened stratum corneum on the palm and heel. Ginefri *et al.* [73] used a high-temperature superconducting (HTS) coil to image human calf skin *in vivo* in a whole-body NMR scanner with 1.5T. They obtained a spatial resolution of 40μm perpendiculars to the skin surface and 80 μm parallel to the skin surface. The slice thickness was 900μm. With this method, structures as fine ramifications connected to the papillary, dermis hair follicles, and the subcutaneous fat can be differentiated. Images that were obtained with the HTS surface coil provided higher quality than those obtained with a copper surface coil.

2.5.1.3 Optical coherence tomography (OCT)

Optical coherence tomography (OCT) is a non-invasive interferometric optical tomographic imaging technique offering mm penetration (approx. 2-3mm in tissue). Both lateral and axial resolutions are in the order of 5-10μm. The OCT pictures are represented as two-dimensional cross sectional images. OCT techniques allow the investigation of the

stratum corneum, epidermis, upper dermis along with skin appendages and blood vessels, a typical image of skin under OCT imaging system can be seen in Fig. 2.6.

The OCT system is based on the principle of the Michelson interferometer which is used in combination with low coherent light. Its detection is based on the optical backscattering properties within the imaging region of interest. Performing a transverse and lateral scan two-dimensional image is produced by optical scattering and refection of photons from the internal tissue microstructures. In this system light from a low coherent light source passes through a single mode fibre, which is equally split into the probe and a reference arm (2x2 coupler). Interference from the reference beam and the probing beam on the detector surface occurs only when the photons are backscattered from the tissue and photons being reflected from the mirror in the reference arm travel exactly the same length. The light reflected from the tissue structure is combined in the fibre optic beam splitter with light from a scanning reference mirror. When the optical path between both beams is the same, the combination of the light from sample beam and the reference beam give rise to an interference pattern.

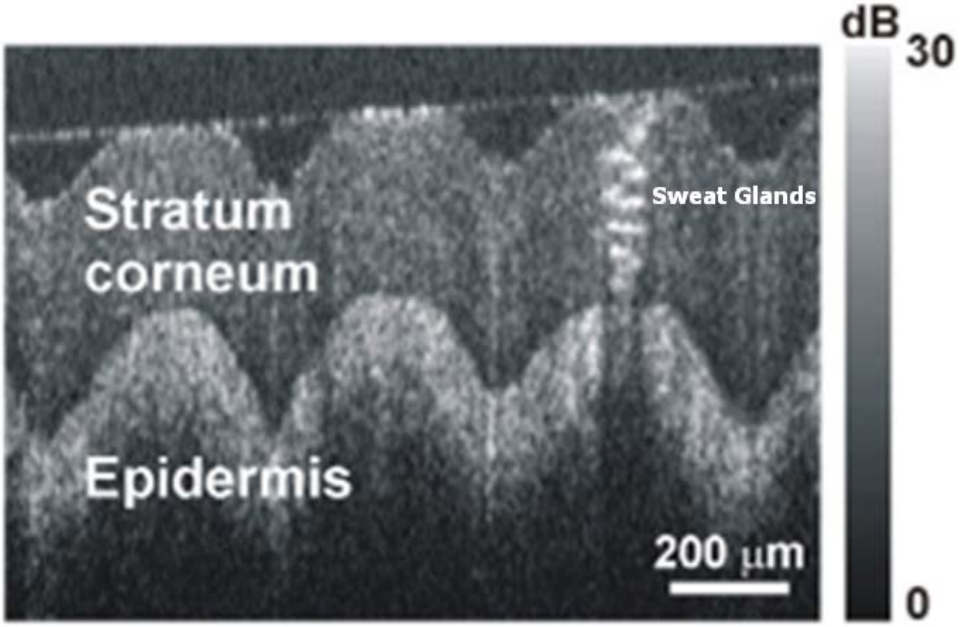

Fig. 2.6 OCT images of skin of in vivo human fingertip. Stratum corneum, epidermis and dermis can be seen, with visible sweat glands [76]

Currently, the OCT system can be a time-domain OCT (TD-OCT) or a frequency domain OCT (FD-OCT) system. Light beam of a superluminence diode (SLD) is coupled into a single-mode fibre optic interferometer. In TD-OCT, within the reference arm, the light is collimated and directed through a scanning mirror system to a reference mirror mounted on a stepper motor. The reference mirror determines the scan position. Coherent interference signal occurs only when the path length between those arms are matched to within the coherence length of the light source. While in FD-OCT, the broadband interference is acquired with spectrally separated detectors, e.g. a grating and a linear detector array. Due to the Fourier relation the depth scan can be immediately calculated by a Fourier-transform from the acquired spectra, without movement of the reference arm the system can image samples. FD-OCT greatly improves the imaging speed, while the reduced losses during a single scan improve the signal to noise proportional. The parallel detection at multiple wavelength ranges limits the scanning range, while the full spectral bandwidth sets the axial resolution.

2.5.1.4 Other imaging techniques

Other imaging modalities with major relevance to skin imaging include dermoscopy, and confocal microscopy, etc.

Dermoscopy, also called dermatoscopy, is a diagnostic technique that is used worldwide in the identification and diagnosis of numerous skin lesions [77, 78]. It used for a more accurate diagnosis of early skin cancers and also known as skin surfacing microscopy, a non-invasive diagnostic technique for the observation of pigmented skin lesions, allowing a better visualization of surface and subsurface structures. This diagnostic tool permits the recognition of structures not visible by the naked eye.

Confocal microscopy is a very high resolution optical technique that can be used to image the epidermis parallel to the skin surface [79]. The images made by confocal microscopy are not perpendicular, but parallel to the skin surface. Real time confocal microscopy can be used for 'optical sectioning' of the tissue, i.e., the imaging of thin sections at a high resolution and a high contrast without the need of physically dissecting the tissue. Confocal microscopy can be developed into fluorescence confocal microscopy, which enables the direct imaging of skin fluorophores *in vivo*.

The wide variety of methods shows that there is no best universal visualisation. Therefore, the choice of method depends on what features are wanted to visualise. This study is focus on the combination of an imaging modality with elastography method to measure and map the elasticity properties of different layers of skin. Thus, an imaging modality which is able to combine with elastography method is necessary. Although the skin imaging techniques, e.g. dermoscopy and confocal microscopy may be successfully applied in dermatology, they are not able to be developed to provide functional elastography. Thus, they are not further discussed in this study. In the next coming section different elastography methods based on the imaging techniques available are described.

2.5.2 Current skin mechanical properties characterization method

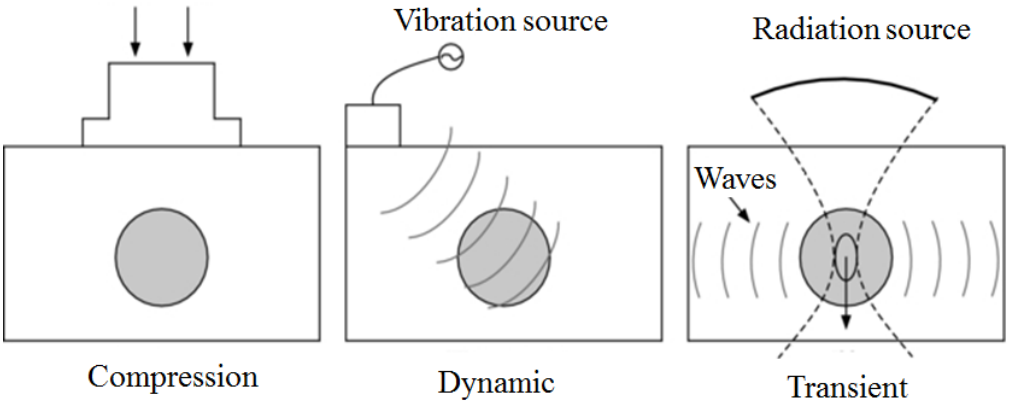

Fig. 2.7 Schematic representation of current approaches to elastographic imaging: compression elastography (left), Dynamic elastography (middle) and transient elastography (right).

Elastography is a technique used to estimate and/or map the biomechanical (elastic) properties of tissue samples by use of imaging techniques. It can provide elastic as well as anatomic information of the biological tissue non-invasively. The main idea of elastography is to combine imaging modalities (e.g. ultrasonic, magnetic resonant and optical) with different mechanical stimulations (e.g. compression, vibration and transient stimulation) [76, 80, 81]. Mechanical stimulation generates tissue responses in the form of displacement, strain or vibration that can be subsequently measured by imaging systems so that the tissue mechanical properties can be evaluated and mapped. Currently, there are

three kinds of elastography techniques: compression elastography, dynamic elastography and transient elastography (Fig. 2.7).

A mechanical mode of compression elastography shows in Fig. 2.8. When a spring is compressed (Fig. 2.8(a)), displacement in each section of the spring depends on the stiffness of the spring (Fig. 2.8(b)). Darker colour spring indicates spring with a higher stiffness a higher K (force constant) and lighter colour spring indicates tissue with a lower stiffness and a lower K. When a force is given to the spring, based on the Hooke's Law, a relationship between K, supplied force (F) and deformation distance (x) of the spring is: $F = -x \times K$, the deformation curve of springs can be obtained a soft spring compresses more than a hard spring. The strain distribution (Fig. 2.10(c)) can be measured by spatially differentiating the displacement at each location. Then, different parts of soft and hard spring can be separated and mapped based on the different deformation value.

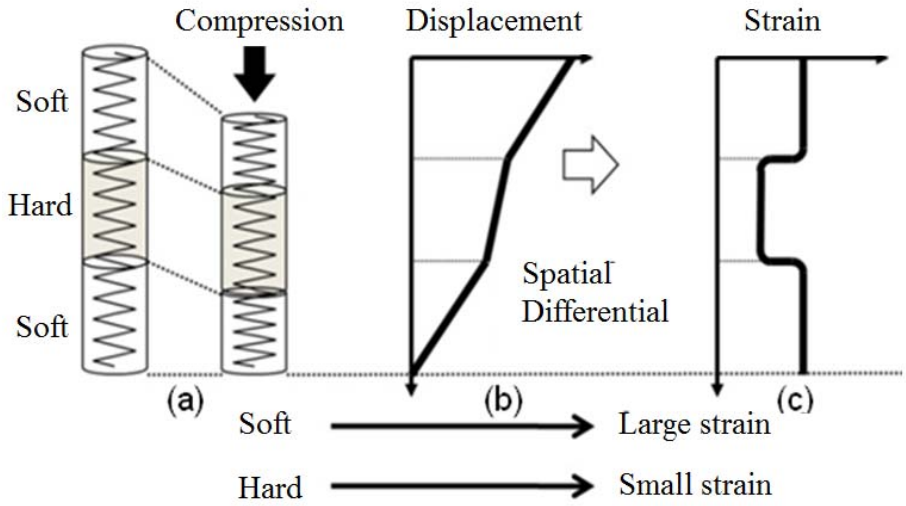

Fig. 2.8 the principle of real time tissue elastography, illustrated here by a spring model. [87]

In dynamic elastography, the material is submitted to low-frequency ((typically between 50 and 10,000 Hz) mechanical vibrations applied with an external vibrator. The vibration induce displacement of tissue, as mentioned before, based on Hooke's Law, the induced vibration amplitude and the corresponding strain of soft material is larger than that of hard material. By tracking the vibration amplitude by imaging systems, the strain distribution of material can be calculated and mapped.

Compression and dynamic elastography techniques have limitations, as they can just provide the strain mapping of sample. With unknown stress, the true Young's modulus value cannot be estimated. However, transient elastography is able to provide the real stiffness of materials. In transient elastography, a transient (pulsed) load is applied to material. The transient load can be generated by a mechanical shaker, a short laser pulse or focused ultrasound. The load generates mechanical waves, including shear waves and surface acoustic waves. By tracking the waves using different imaging systems, wave speed can be measured. The wave speed is directly related to stiffness of material. Thus, the real stiffness of material can be estimated.

2.5.2.1 Ultrasound elastography

Ultrasound elastography involves the use of ultrasound to produce measurements and provide mapping of tissue stiffness. A variety of methods are used to create the displacement in the tissue with the resultant displacement or strain can then displayed as a colour overlay on a conventional B-Mode ultrasound image [82-99]. With the help of digital signal processing and image processing techniques combining with ultrasound imaging technology, different elastic properties of tissue can be obtained and mapped.

Take ultrasound compression elastography as an example, a static and uniform stress is offered to the tissue from one direction by a compressor installed at the end of ultrasound transducer shown as Fig. 2. 9 (a), the tissue will then deform (Fig. 2. 9 (b)) [88]. As explained in last section, stiffer tissues (tissue with high Young's modulus) suffer from a smaller strain than softer tissues.

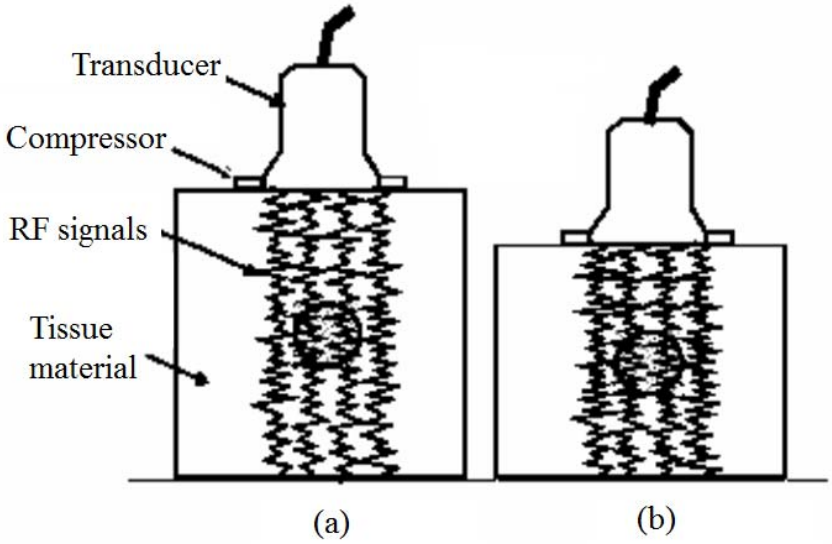

Fig. 2.9 (a) compression elastography practical experiment; (b) static and uniform stress is applied to the tissue [88].

Strain is measured by ultrasound combining signal processing technology. As in Fig 2.9, before and after compression, ultrasound detects two sequences of signals (Fig 2.10 (up)). In signal processing, cross-correlation is a measure of similarity of two waveforms as a function of a time-lag applied to one of them. With a chosen signal which represented the interested area of sample, a cross-correlation between the chosen signal and the whole signal after compression can be calculated:

$$R(\tau) = \frac{\sum_{k=1}^{t_1+T-1} s_1(k)s_2(k+\tau)}{\sqrt{\sum_{k=1}^{t_1+T-1} s_1^2(k)\cdot s_2^2(k+\tau)}} \tag{2-2}$$

where s_1 and s_2 are the signal sequences of tissue before and after compression, t_1 is the starting time of signal recording and T is the length of sample signal. Cross-correlation curve can be obtained as in Fig 2.10 (down) with the highest value spotted. Highest cross-correlation value indicates the location of sample signal after the compression. By measuring the displacement of ultrasound sample signal, we can obtain the strain of corresponding tissue [93] from the followed equation:

$$\varepsilon = \frac{\Delta t_b - \Delta t_a}{\Delta T} = \frac{(t_{1b} - t_{2b}) - (t_{1a} - t_{2a})}{t_{1b} - t_{1a}} \tag{2-3}$$

Where t_{1a} and t_{1b} are the beginning and ending locations of the signal before compression, t_{2a} and t_{2b} are the beginning and ending locations of the signal after compression. Repeating the signal processing procedure, displacements of the whole tissue can be calculated.

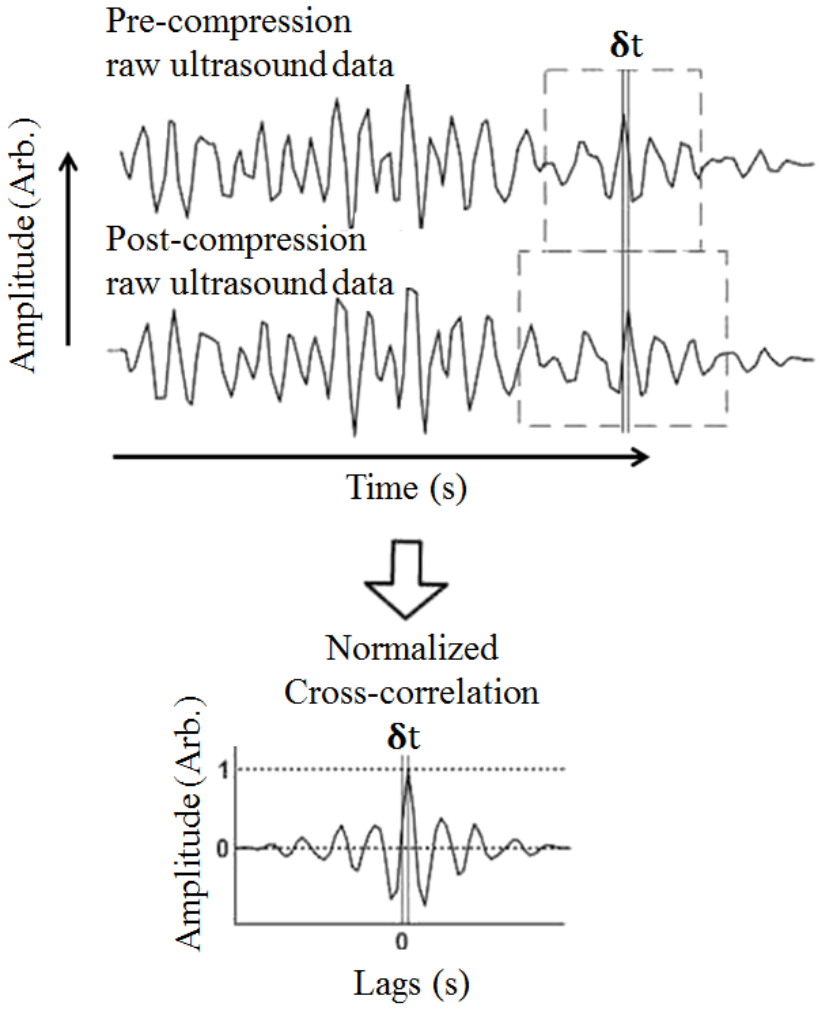

Fig. 2.10 (up) A-mode signal of tissue detected before compression and after compression; (down) cross-correlation curve of two signals

For 2-D compression elastography, B-mode linear array transducer is used to detect signals from every array element of the transducer before and after compression, and

process the signals to find different strains. Then the information would pass a strain filter, and be re-arranged into 2-D by expressing the Young's modulus as different grey scale pixel values or different colours [89]. For example, the ultrasound elastography system developed by Hitachi Company in Japan uses red, green and blue to express soft, normal and stiff parts of tissues.

Besides compression elastography, dynamic elastography and transient elastography also developed in ultrasound elastography. Early in 1987, Krouskop*et et al.* reported a dynamic approach combining external mechanical stimulation of target tissues with Doppler ultrasound displacement detection to get the information of the relative tissue motion [100]. Then, shear wave combine ultrasound imaging has been widely studied, developed and successfully applied in clinical environments with the improvement of the resolution and speed ultrasound imaging system, e.g. improvement of the transducer frequency bandwidth and adoption of multi-array transducer. Both the amplitude and the shear wave speed (calculated from phase of the internal vibrations) were measured from Doppler frequency modulation of transmitted probing ultrasound waves from ultrasound transducer.

2.5.2.2 Magnetic resonance elastography (MRE)

Similar to ultrasound elastography, magnetic resonance elastography (MRE) uses phase-sensitive magnetic resonance methods that measure the inner vibration of the tissue caused by a mechanical excitation at the body surface [14, 15].

In general, two different approaches to MRE can be differentiated: a static MRE, with similar principles with compression ultrasound elastography, measures the differences in Hydrogen spin location before and after an applied static compression. The other approach is dynamic MRE, which uses continues excitation generate a mechanical wave.

In the static elastography is usually performed quasistatically, using very low excitation frequencies (0–1 Hz) [14, 15]. In this case, wave propagation is assumed to be negligible, with the tissue in an approximate static stress. The compression is alternated between the two states during each individual acquisition [time of repetition (TR)] of the MR experiment. The main drawback of the static approach is that it is very sensitive to motion such as breathing.

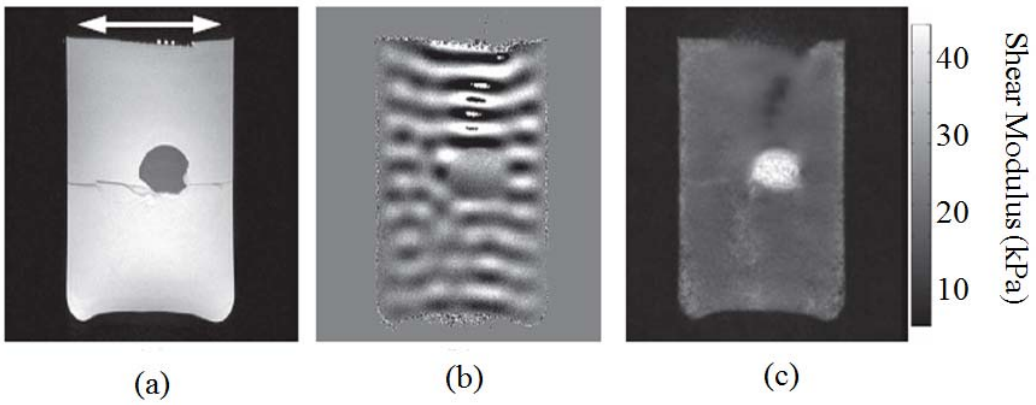

Fig. 2.11 (a) A magnitude image, (b) phase image, and (c) elastogram of a 2% agar inclusion imbedded within 1% agar gel [15].

The principle of transient MRE is based on the fact that the velocity of the propagation mechanical waves (especially the shear wave) depends on the elasticity of the medium. MR techniques exist to quantify this Hydrogen spin motion, usually captured in the phase of the detected MR signal, with sensitivities down to tens of micrometres. Using such a technique, it is possible to determine the wavelength/wave speed of a propagating mechanical wave and consequently calculate the elasticity of the tissue. The principle of MRE is demonstrated well using an agar gel phantom containing compartments with two different concentrations (Fig. 2.11). Fig. 2.11(a) shows the mechanical excitation of the agar phantom. The mechanical excitation was performed transversely (white arrow) with the piezoelectric actuator on top of the phantom. Fig. 2.11(b) shows phase image. The wavelength of the propagating mechanical wave is distinctly longer in the hard inclusion, representing higher elastic modulus. The shear modulus, as reconstructed from the phase image, is visualized directly in the elastogram (2.11(c)) [14]. The grey values of the acquired phase images represent the encoded spin motion and consequently the propagating mechanical wave in the tissue.

2.5.2.3 Optical coherence elastography (OCE)

Beside ultrasound elastography and MR elastography, elastography using optical imaging attract applications in dermatology and ophthalmology. Optical coherence tomography (OCT)–based elastography, which is termed optical coherence elastography

(OCE), is the technique that employs optical coherence tomography (OCT) to detect and mapping depth-resolved sample elasticity using compression, dynamic or transient method. OCE was first introduced by Schmitt in 1998 [101, 102]. OCE shows great potential for micron and submicron imaging applications because of its benefits from the high resolution of OCT, while additionally providing the elastic properties of the sample. OCT provides structural images approaching histology, where the microstructures of biological tissues can be quantified. This beneficial high-resolution, non-invasive imaging modality allows OCE to evaluate the mechanics of intact tissue with ultra-high resolution (3-10 μm) that cannot be offered by elastograms produced by the competing imaging modalities of ultrasound or MRI.

In the last decade, several studies have demonstrated the ability of OCE to provide valuable information about the micromechanical properties of tissue. OCE has been used to investigate the microscopic deformation of tissue phantoms, porcine muscle, and human skin as a function of depth under compressive loads [103]; define the properties of collagen organisation in musculoskeletal tissue [104]; provide the material properties of the cornea [105]; and develop strain maps of engineered tissue at different stages of embryonic development [106]. Finally, one of the current research directions in OCE imaging has been to develop intravascular OCE for rupture-prone (vulnerable) plaque detection [107].

In previous studies of OCE in dermatology applications, measurement of vibration amplitude has been used to map the elastic properties of skin which can be used for monitoring sex- and age-related skin changes, and for the follow up of dermatologic disorders or other systemic diseases [108-111]. An example of vibration OCE is shown in Fig. 2.12, which are 3D-OCT and OCE images of skin from the middle finger of the same subject. In Figs. 2.12 (a) and 2.12 (d), two perspective views of the OCT data are presented, with one corner cut away to a depth of 300 μm, revealing internal structure. In Figs. 2.12 (b) and 2.12 (e), the OCE signal is displayed and, in Figs. 2.12 (c) and 2.12 (f), the OCE data is overlaid on the OCT data. In these images, the highest OCE signal is visible in the living epidermis and the sweat glands.

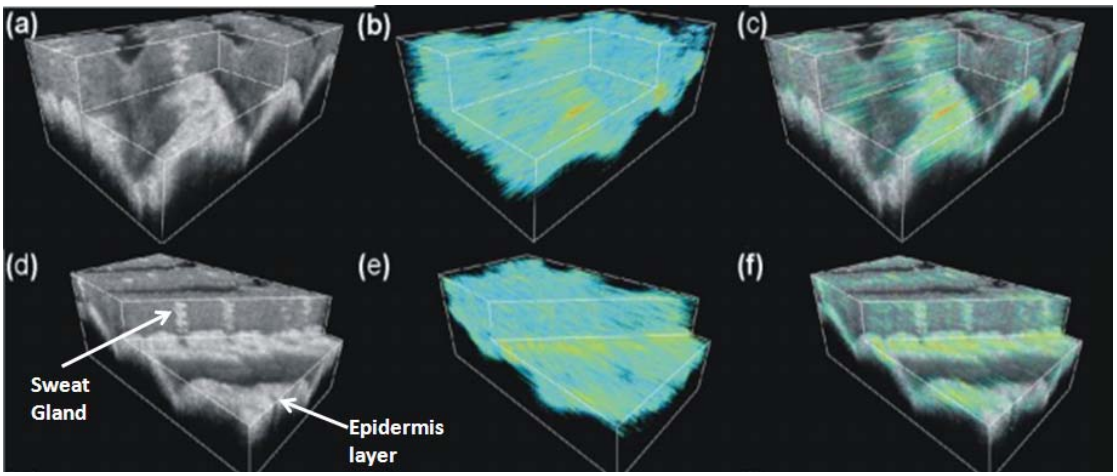

Fig. 2.12 3D visualization of in vivo human finger skin (a) OCT, (b) OCE and (c) overlay from first perspective view; (d) OCT, (e) OCE and (f) overlay from second perspective view [111].

OCE systems use an external shaker to induce mechanical shear waves or standing waves that subsequently travel within a sample. Through evaluating the strain rate of shear energy, OCE has been shown capable of differentiating tissues with differing stiffness [108-111], delivering a promise to achieve 3-D elastography of superficial human skin [110-111] for dermatological applications. Liang and Boppart [106, 108] reported that with the combination of optical coherence tomography (OCT), shear wave speed can be utilized in measuring Young's moduli of skin which are site. Although analysis of the strain rate of shear wave is quite popular, skin is treated as a homogeneous material and it is difficult to provide the elasticity of every skin layer quantitatively.

2.5.3 Comparison of the imaging techniques

The advantages of ultrasound and ultrasound elastography over other imaging techniques relate to its capability, versatility, portability, safety, and economic feasibility. Commercially available ultrasound imaging systems are capable of spatial resolution approaching that of magnetic resonance microscopy as a result of advances in transducer and computing technology. However, there are limitations of ultrasound technique in dermatological applications. Although high frequency ultrasound imaging greatly improve the resolution, it is still limited by very little tissue differences between normal skin and lesion. In addition, ultrasound imaging requires the contact between ultrasound

transducer and sample. It is not ideal in clinical environments, and most importantly, the contact may bring mechanical load to skin, which will impact the elasticity measurement of skin.

MRI is more advantageous over other radiological techniques in analysing some tissue. One of the most advantages of MRI is its capacity for displaying soft tissue contrast. Image contrast can be tailored to the specific clinical application so that specific types of pathology are emphasized. The cellular distribution of water with or without increase in global tissue water is different in cancerous tissue than that of normal skin. The increase in total proton density associated with changes in water structure alters free mobile protons in epidermis, dermis, and subcutaneous tissue. These changes reflect as contrast and brightness in MRIs. However, at this moment a major drawback of MRI is that special skin-surface coils are not commercially available. The cost of this method is much higher than other imaging methods. The MRI systems are not portable now. In addition, there are hazards intrinsic to the MR environment. It takes relatively longer time to obtain a MR image than other imaging techniques. The above disadvantages bring significant difficulties for the developing of MR elastography in dermatology.

OCT can provide image in deeper layers of the skin with an ultra-high resolution than ultrasound. OCT can provide imaging spatial resolution of 1-10 μm, which is much high enough to image the structure to differentiate skin layers and skin structures. Another large advantage of OCT is that it is a portable and non-contact imaging technique with relatively low cost, which is ideal in clinic. OCT provides fast two-dimensional (2D) image acquisition rates in kHz range, and potentially even higher. Thus, real time imaging can be fulfilled. The only limitation of OCT is the imaging depth is around 1-4mm, which can cover the epidermis and dermis of skin. However it is acceptable as most of the skin diseases happen these two layers. These features of OCT make it an ideal tool for dermatological applications. However, current OCE techniques cannot provide quantitative and localised elasticity information of different layers.

The advantages and disadvantages of different imaging modalities is summarised in Table 2.2.

Table 2.2 The comparison of different skin imaging method

Imaging method	Resolution	Imaging depth	Advantages	Disadvantages
Ultrasound/ Ultrasound elastography	50-500 μm	mm to cm	3D datasets, Real-time, low cost, portable	Limited spatial resolution, contact
MRI/MRE	30-500 μm	Not limited	3D datasets	High cost, commercially unavailable, long scan time, low spatial resolution, not portable
OCT/OCE	5-10 μm	2-3mm	3D datasets, real time, portable, low cost, high resolution	Limited imaging depth

2.6 Conclusion

Although different imaging and elastography techniques available now, very limited applications have been taken place in dermatological applications. It is because there is no ideal technique available to provide high resolution depth-resolved structural image as well as quantitative elasticity of different layers of skin tissue. It would be of great advantage to have the ability to monitor changes of the mechanical properties of skin layers which provides the dermatologist with relevant data about changes in the properties of the affected area allowing better diagnosis, and disease progression to be monitored and to study the effect of any treatment.

Comparing to other imaging techniques, OCT imaging technique has great advantages: it can provide high resolution of skin structure images, with low cost, portable nature and relatively acceptable imaging depth. It is also a non-contact method which applicable in varies clinical environments. Thus, this study chooses OCT as a base, and develops elastography using SAW method, which aims to provide quantitative and localised elasticity information of different skin layers. Taking advantages of high resolution image provided by OCT technique, a system will be developed, which allows the rapid quantitative functional characterisation of skin using SAW method. Due to its non-contact nature of generation and detection of SAW, unlike traditional elastography methods, there is no requirement for a coupling medium and there is almost no sensitivity to surface orientation. The method also studied the geometrical and quantitative mechanical

properties to be monitored simultaneously which other existing methods utilised today are not capable of measuring.

Chapter 3: Surface acoustic wave (SAW) theory, characterisation and applications

3.1 Introduction

The application or variation of a force on a body produces a stress and strain response, and might generate mechanical waves that behave different in the body, e.g. the travel path and directions, partial trajectory, travel speed and energy distribution. These are body waves and surface waves. Body waves, i.e., longitudinal waves and shear waves propagate body of material, which means the deep interior of material. On the other hand, surface acoustic wave propagates on the material surface.

Longitudinal waves (also known as P-wave) are compressional waves. In longitudinal waves, the motion of particles is parallel to the direction of propagation, as shown in Fig. 3.1(a). Fig. 3.2 (a) shows propagating directions of pulse stimulator generated mechanical waves on a solid. Among mechanical waves, the longitudinal wave travels the fastest in the material bulk body. Fig. 3.2 (b) shows energy distribution of longitudinal waves in the body.

The second form of body wave is known as the shear wave (also known as S-wave), where particles oscillate in a direction perpendicular to the direction of propagation of the wave (Fig. 3.1(b)). The shear wave is so named because it arises when particles in the first plane are moved in a periodic manner under a shear force as shown in Fig. 3.1(b). The energy distribution of pulse generated shear wave in body can be found in Fig. 3.2 (c).

When the medium is bounded by a free surface, also another kind of phenomena occurs: surface acoustic waves (SAW, also known as Rayleigh wave) are generated and propagate near the surface. They induce a different particle motion as it will be shown in Fig. 3.1(c). They do not irradiate energy toward interior, SAW induce a particle motion in the vertical plane that contains the direction of propagation, and in a homogeneous body is, at the free surface, a retrograde elliptic orbit. SAW velocity in a homogeneous medium is less than the shear wave velocity. If there are variations of the elastic properties with depth, SAW become dispersive: the SAW with different wavelength propagate with different velocities.

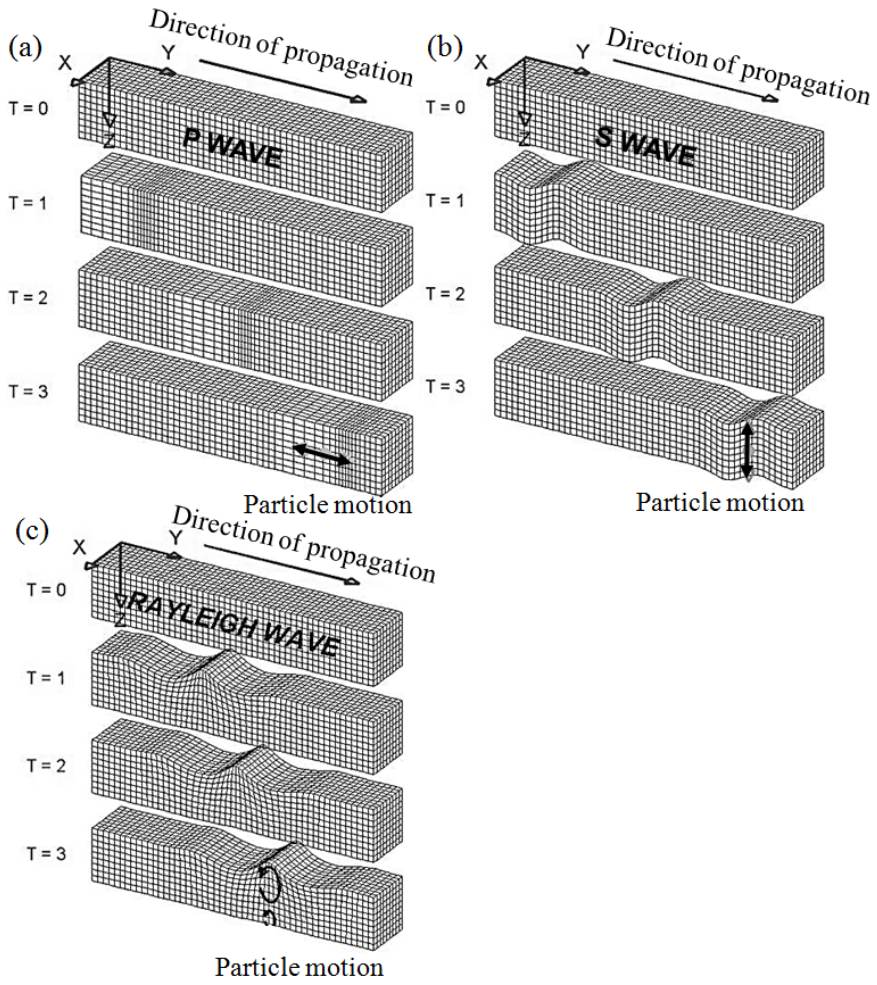

Fig. 3.1 Particle trajectory of longitudinal waves (a), shear waves (b) and surface acoustic waves (c) [120].

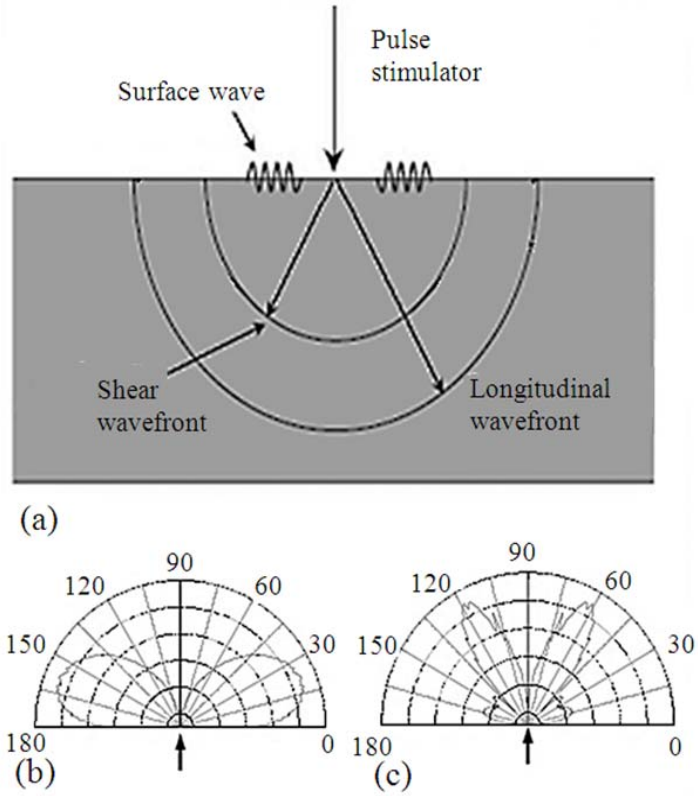

Fig. 3.2 waves generated by a pulse stimulator on a solid (a), and energy distributions of longitudinal waves (b) and shear waves (c) [121]

Mechanical waves have been successfully used in a very wide variety of applications over an extended range in geometry [112, 113] and industry [114-116]. Recently, mechanical wave methods have attracted increasing attention in biomedical applications, including angiography [117], mechanical properties estimation [118], elastography which combines different means of imaging techniques [119].

This chapter reviews a basic introduction of mechanical wave theory. An overview of the exciting applications of the most commonly used mechanical waves, i.e. longitudinal wave, shear wave and SAW in biomedical area that appeared in the literature is introduced. More importantly, the characterisations of SAW, including velocity, displacement, energy distribution, geometric spreading and dispersion, frequency range and applications will be introduced in this chapter, which serves as the theoretical basis of subsequent chapters.

3.2 Theoretical principles and backgrounds of mechanical waves

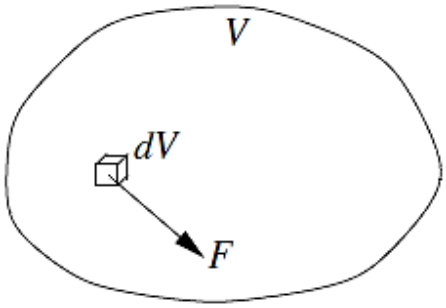

Fig. 3.3 Element volume dV in a body V, with applied body force $\boldsymbol{F}$.

To obtain wave equations of mechanical waves in solid materials, it is useful to suppose a particle in isotropic material and analyse the stress-strain relationships. In three dimensional Cartesian coordinate system, it assumes that body force is acting throughout the element volume (Fig. 3.3). Here, the body force ($\boldsymbol{F}$) is a force that acts throughout the volume of a body, and the element volume (dV in Fig. 3.3) is the smallest volume over which a measurement can be made that will yield a value representative of the whole ($\boldsymbol{V}$). The motion equations of this element volume are given according to Newton Second Law:

$$\left.\begin{aligned}\rho\frac{\partial^2\xi}{\partial t^2}&=\frac{\partial T_{xx}}{\partial x}+\frac{\partial T_{yx}}{\partial y}+\frac{\partial T_{zx}}{\partial z}\\ \rho\frac{\partial^2\eta}{\partial t^2}&=\frac{\partial T_{xy}}{\partial x}+\frac{\partial T_{yy}}{\partial y}+\frac{\partial T_{zy}}{\partial z}\\ \rho\frac{\partial^2\zeta}{\partial t^2}&=\frac{\partial T_{xz}}{\partial x}+\frac{\partial T_{yz}}{\partial y}+\frac{\partial T_{zz}}{\partial z}\end{aligned}\right\} \tag{3-1}$$

where ρ is the mass density of the body, ξ, η and ζ are displacements of particles along x axis, y axis and z axis, respectively. Stress is denoted by T_{ij}, where the subscripts stand for that corresponding stress component is acting on the plane of i and j axis. In a homogeneous material, the simplified Hooke's Law can be given as:

$$\left.\begin{aligned} T_{xx} &= \lambda(\frac{\partial \xi}{\partial x}+\frac{\partial \eta}{\partial y}+\frac{\partial \zeta}{\partial z})+2\mu\frac{\partial \xi}{\partial x} \\ T_{yy} &= \lambda(\frac{\partial \xi}{\partial x}+\frac{\partial \eta}{\partial y}+\frac{\partial \zeta}{\partial z})+2\mu\frac{\partial \eta}{\partial y} \\ T_{zz} &= \lambda(\frac{\partial \xi}{\partial x}+\frac{\partial \eta}{\partial y}+\frac{\partial \zeta}{\partial z})+2\mu\frac{\partial \zeta}{\partial z} \\ T_{yz} &= \mu(\frac{\partial \eta}{\partial y}+\frac{\partial \zeta}{\partial z}) \\ T_{zx} &= \mu(\frac{\partial \xi}{\partial x}+\frac{\partial \zeta}{\partial z}) \\ T_{xy} &= \mu(\frac{\partial \xi}{\partial x}+\frac{\partial \eta}{\partial y}) \end{aligned}\right\} \tag{3-2}$$

Where λ and μ are Lame constants. Combined Eq. 3-1 with generalised Hooke Law, we can get equations:

$$\left.\begin{aligned} \rho\frac{\partial^2 \xi}{\partial t^2} &= (\lambda+\mu)\frac{\partial \Delta}{\partial x}+\mu\nabla^2\xi \\ \rho\frac{\partial^2 \eta}{\partial t^2} &= (\lambda+\mu)\frac{\partial \Delta}{\partial y}+\mu\nabla^2\eta \\ \rho\frac{\partial^2 \zeta}{\partial t^2} &= (\lambda+\mu)\frac{\partial \Delta}{\partial z}+\mu\nabla^2\zeta \end{aligned}\right\} \tag{3-3}$$

Where $\Delta=\frac{\partial \xi}{\partial x}+\frac{\partial \eta}{\partial y}+\frac{\partial \zeta}{\partial z}$ and $\nabla^2=\frac{\partial^2}{\partial x^2}+\frac{\partial^2}{\partial y^2}+\frac{\partial^2}{\partial z^2}$.

Here, define that $\mathbf{s}=\xi\mathbf{i}+\eta\mathbf{j}+\zeta\mathbf{k}$ is the particle displacement vector and $\mathbf{v}=v_x\mathbf{i}+v_y\mathbf{j}+v_z\mathbf{k}$ is the particle velocity vector, Eq.3-3 can be expressed in terms of particle displacement:

$$\rho\left(\frac{\partial^2\xi}{\partial t^2}+\frac{\partial^2\eta}{\partial t^2}+\frac{\partial^2\zeta}{\partial t^2}\right)=(\lambda+\mu)\left(\frac{\partial\Delta}{\partial x}+\frac{\partial\Delta}{\partial y}+\frac{\partial\Delta}{\partial z}\right)+\mu(\nabla^2\xi+\nabla^2\eta+\nabla^2\zeta) \tag{3-4}$$

Then this equation can be expressed as:

$$\rho\frac{\partial^2\mathbf{s}}{\partial t^2}=(\lambda+\mu)\nabla(\nabla\cdot\mathbf{s})+\mu\nabla^2\mathbf{s} \tag{3-5}$$

Because for vector $\mathbf{s}$, $\nabla(\nabla\cdot\mathbf{s})=\nabla^2\mathbf{s}-\nabla\times(\nabla\times\mathbf{s})$, thus Eq. 3-5 can be expressed as:

$$\rho\frac{\partial^2\mathbf{s}}{\partial t^2}=(\lambda+2\mu)\nabla(\nabla\cdot\mathbf{s})-\mu\nabla\times(\nabla\times\mathbf{s}) \tag{3-6}$$

Since the velocity $\mathbf{v}=d\mathbf{s}/dt$, wave equation can also be given in terms of particle velocity:

$$\rho\frac{\partial^2\mathbf{v}}{\partial t^2}=(\lambda+2\mu)\nabla(\nabla\cdot\mathbf{v})-\mu\nabla\times(\nabla\times\mathbf{v}) \tag{3-7}$$

Based on Helmoltz's theorem, a vector field can be decomposed into the gradient of a scalar field and the curl of vector field with zero divergence, thus, $\mathbf{v}$ in Eq. 3-7 can be

substituted by $\mathbf{v} = \nabla\Phi + \nabla \times \Psi$ and $\nabla \cdot \Psi = 0$, where Φ is scalar potential and $\Psi=\Psi_x\mathbf{i}+\Psi_y\mathbf{j}+\Psi_z\mathbf{k}$ is vector potential. Then separating scalar potential Φ from vector potential Ψ, two equations can be obtained from Eq. 3-7:

$$\begin{aligned} \rho\frac{\partial^2\Phi}{\partial t^2} &= (\lambda + 2\mu)\nabla^2\Phi \\ \rho\frac{\partial^2\Psi}{\partial t^2} &= \mu\nabla^2\Phi \end{aligned} \tag{3-8}$$

The two equations describe plane waves that propagate in a specific direction with Φ describing longitudinal waves while Ψ describing shear wave. Eq. 3-7 can also be expressed as:

$$\left.\begin{aligned} \nabla^2\Phi &= \frac{1}{C_L^2}\frac{\partial^2\Phi}{\partial t^2} \\ \nabla^2\Psi &= \frac{1}{C_S^2}\frac{\partial^2\Psi}{\partial t^2} \end{aligned}\right\} \tag{3-9}$$

By solving Eq. 3-8 and Eq. 3-9, the phase velocities of longitudinal wave (C_L) and shear wave (C_S) are given by:

$$C_L = \sqrt{(\lambda + 2\mu)/\rho},\ C_S = \sqrt{\mu/\rho} \tag{3-10}$$

Apart from longitudinal waves and shear waves known as bulk waves, there is another kind of wave that travels along the solid-air interface (free surface). It is surface acoustic wave (SAW), which is also well known as Rayleigh wave. To obtain the potential function of SAW, a two dimensional plane containing *x* axis and *z* axis is taken into consideration for simplicity, where *x* axis indicate the depth and *z* axis indicate the surface. Assuming the solution to equation set by:

$$\left.\begin{aligned} \Phi &= \Phi_a e^{-\alpha x} e^{j(wt-k_s z)} \\ \Psi &= \Psi_a = \Psi_a e^{-\beta x} e^{j(wt-k_s z)} \end{aligned}\right\} \tag{3-11}$$

It has the same phase term as that of longitudinal wave and shear wave. However, an additional real exponential term accounts for the rapid attenuation of SAW along *x* axis (depth of the body), which is a main characterisation of SAW. In addition, SAW can be viewed as the combination of shear energy and longitudinal energy that propagate on the material surface, which makes the material particle move in an elliptical trajectory. Substituting Eq. 3-11 with Eq. 3-9, the relationship between attenuation coefficient and wave vector can be obtained:

$$\alpha^2 = k_R^2 - k_L^2, \quad \beta^2 = k_R^2 - k_S^2 \tag{3-10}$$

where k_L, k_S, k_R are wave vectors of longitudinal wave, shear wave and SAW, respectively. Here, we set:

$$\left.\begin{aligned} g &= \left(\frac{C_R}{C_S}\right)^2 \\ q &= \left(\frac{C_S}{C_L}\right)^2 = \frac{\mu}{\lambda+2\mu} = \frac{1-\upsilon}{2(1-2\upsilon)} \end{aligned}\right\} \tag{3-11}$$

Where υ is Poisson's ratio of the body. With boundary conditions that there is no stress at solid-air interface, we can have:

$$\left.\begin{aligned} &\left[\frac{\partial^2\Phi}{\partial t^2} + 2C_S\left(\frac{\partial^2\Psi}{\partial x\partial z} - \frac{\partial^2\Phi}{\partial z^2}\right)\right]_{x=0} = 0 \\ &\left[\frac{\partial^2\Psi}{\partial z^2} - \frac{\partial^2\Psi}{\partial x^2} + 2\frac{\partial^2\Phi}{\partial x\partial z}\right]_{x=0} = 0 \end{aligned}\right\} \tag{3-12}$$

Combine Eq. 3-12 with Eq. 3-9 and Eq. 3-11, then we can get:

$$\left.\begin{aligned} &\omega^2\left[1-2\left(\frac{C_S}{C_R}\right)^2\right]\Phi_A + 2j\beta\omega\frac{C_S^{\,2}}{C_R}\Psi_A = 0 \\ &2\omega\frac{\alpha}{C_R}\Phi_A - j\left(\beta^2 + \frac{\omega^2}{C_R^{\,2}}\right)\Psi_A = 0 \end{aligned}\right\} \tag{3-13}$$

In order to obtain C_R, we can obtain to solve Eq. 3-13:

$$\begin{vmatrix} \omega^2\left[1-2\left(\frac{C_S}{C_R}\right)^2\right] & 2j\beta\omega\frac{C_S^{\,2}}{C_R} \\ 2\omega\frac{\alpha}{C_R} & j\left(\beta^2 + \frac{\omega^2}{C_R^{\,2}}\right) \end{vmatrix} = 0 \tag{3-14}$$

From Eq. 3-14, we can have the Rayleigh equation:

$$\left[1-2\left(\frac{C_S}{C_R}\right)^2\right]\left(\beta^2 + \frac{\omega^2}{C_R^{\,2}}\right) + 4\alpha\beta\left(\frac{C_S}{C_R}\right)^2 = 0 \tag{3-15}$$

Together with Eq. 3-11, the equation then can be re-written as:

$$g^6 - 8g^4 + 8(3-2q^2)g^2 + 16(q^2-1) = 0 \tag{3-16}$$

Given Poisson's ratio υ, Eq. 3-16 can be numerically solved to get $C_R = \sqrt{g}C_S$, where g has an approximate expression of $g = \frac{0.87+1.12\upsilon}{1+\upsilon}$.

Because $g<1$, thus, the SAW velocity is always slower than the shear wave velocity.

3.3 Characterisation and application of longitudinal wave and shear wave

3.3.1 Longitudinal wave

Longitudinal waves can be induced in solids, gas as well as liquids since the energy travels through the atomic structure by a series of compressions and expansion movements. The relationship between velocity of longitudinal waves (C_L) and material elasticity is given by the expression, which is widely used in industry for metallic material elasticity measurement [122]:

$$C_L = \sqrt{\frac{(\lambda + 2\mu)}{\rho}} \approx \sqrt{\frac{E(1-\upsilon)}{\rho(1+\upsilon)(1-2\upsilon)}} \tag{3-17}$$

where ρ is the density and υ is the Poisson's ratio of the material.

Compared to shear waves and SAW, typical longitudinal waves have relatively higher speed (5850m/s in steel, 1480m/s in water and 1550m/s in most of biological tissues) and a much broader frequency bandwidth (GHz in hard solid material [123] and >100MHz in biology tissues [124]) and thus, a longer wavelength. The typical waveforms of pulse generated longitudinal wave in steel and tissue mimicking agar phantom can be found in Fig. 3.4 (a) and (c), respectively. Their corresponding frequency spectrums are shown in Fig. 3.4 (b) and (d). The detected frequency bandwidth is lower than theoretical value from literature because it is limited by the frequency bandwidth of measuring equipment.

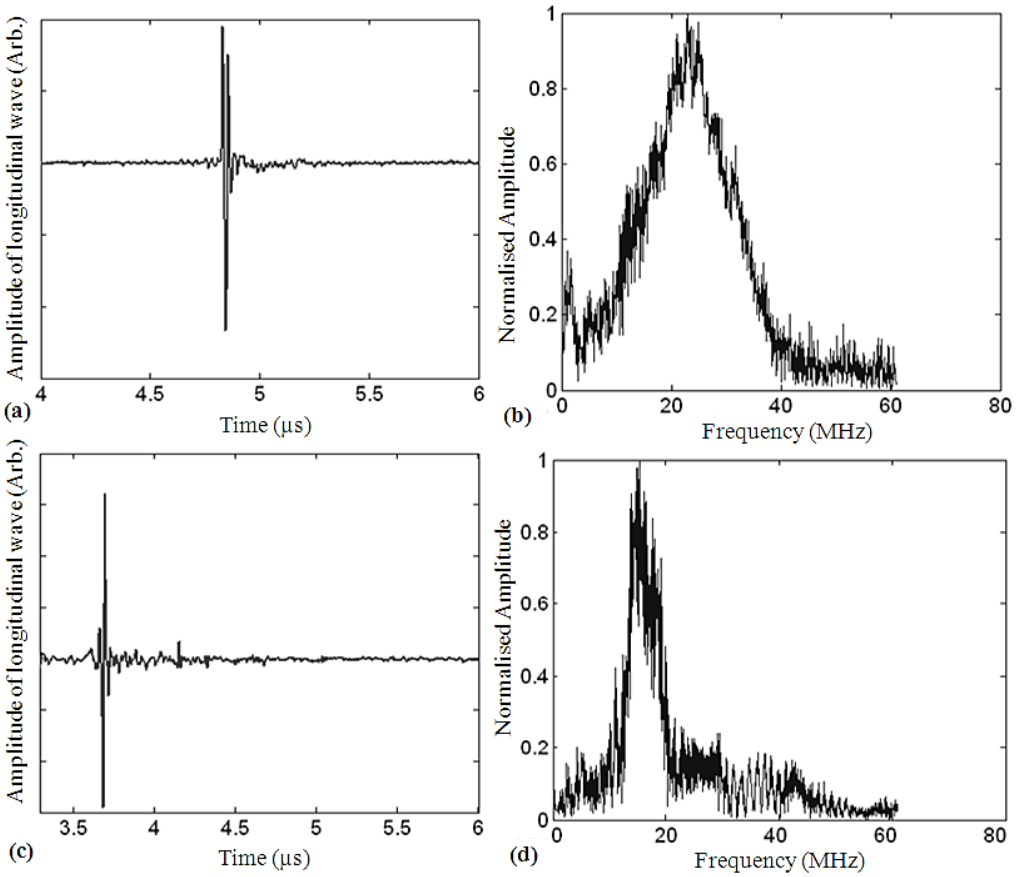

Fig. 3.4 Typical longitudinal waveform and corresponded frequency spectrum of steel (a, b) and tissue mimicking agar phantom (c, d)

Longitudinal waves have many biomedical applications. One well known application is the ultrasound imaging [125-127], since ultrasound wave is a typical longitudinal wave. Currently, ultrasonic technology is widely applied in biomedical area, e.g. high frequency ultrasound imaging [125], Doppler ultrasound imaging [126-127] and high focus ultrasound for cancer treatment [128-131], *etc.* Combined with optical technologies, laser generated longitudinal waves can be utilised in photoacoustic imaging (PAM) [132-142], which is a relatively new hybrid imaging modality. It provides both a high contrast and a high spatial resolution images. PAM has been widely applied in biomedical area, including high resolution photoacoustic imaging and photoacoustic microscopy [137, 138,143], angiography [139, 140], flow detection and measurement [141], blood oxygenation measurement [141, 142] and nano-particle tracking [142].

For elastic materials, it is possible to detect the Young's modulus directly by analysing longitudinal wave speed as long as we know the Poisson's ratio, because Young's modulus is directly related to it by Eq. 3-17 [144-146]. But it is not suitable for measuring the Young's modulus of soft uncompressible materials, of which Poisson' ratio approximates to 0.5. Because for Eq. 3-17, a Poisson's ratio approximate to 0.5 will lead to a potentially large error in calculation. As most of biological tissues are soft uncompressible materials (articular cartilage and liver.), currently there is no application of longitudinal waves to evaluate the quantitative elasticity information of soft tissue directly.

3.3.2 Shear wave

Shear waves can only propagate effectively in solid materials and not in liquids or gases. The velocity of shear waves, C_S is given by the expression [147-148]:

$$C_S = \sqrt{\frac{\mu}{\rho}} \approx \sqrt{\frac{E}{2\rho(1+\upsilon)}} \tag{3-18}$$

The shear wave speed is slower than longitudinal waves (2 times slower in hard solids and hundreds times slower in soft solids), e.g. shear wave's speed in steel is 3240m/s in steel [122] 20m/s in muscle [149] and 2m/s in liver [150]. Shear waves generated by pulse have a wider frequency bandwidth (up to 6MHz in metal and 5-20 kHz in biology tissues [149, 150]). The shear wave which consists of many pulses can be generated when stimulated by a vibration source for a long period of time, named continues wave (CW) source. Under such conditions an initial pulse is followed immediately by another pulse, which is known as a wave train. The typical shear waveforms generated by CW source within the agar phantom can be observed in Fig. 3.5 (left). In this case, the frequency bandwidth would be narrow which mainly represent the frequency of vibration source (Fig. 3.5 (right)).

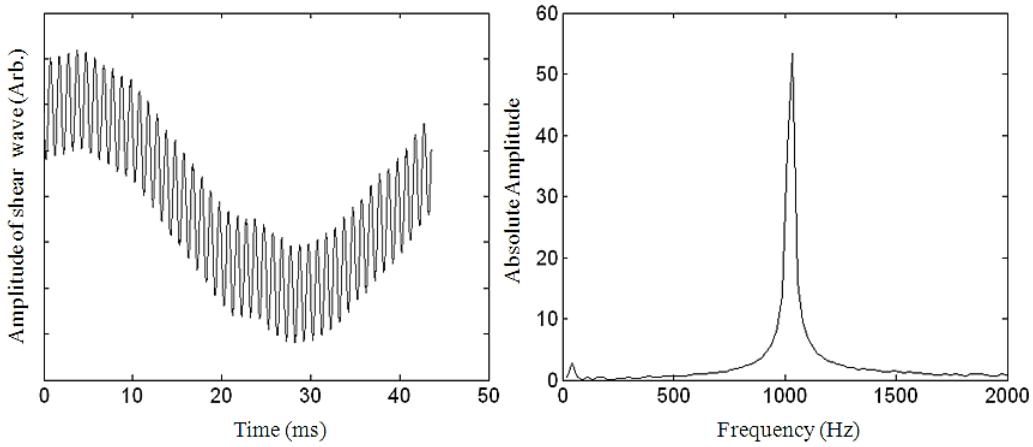

Fig. 3.5 (left) typical shear waveform generated by CW source in tissue mimicking agar phantom and the corresponding frequency content (right)

Shear wave method has been widely used in elastography techniques, in which the shear waves are mainly induced by acoustic radiation force [151] or external vibrating shaker [152]. The main idea is to combine an imaging technology, e.g. ultrasound imaging, MRI or optical imaging with shear waves generated by mechanical stimulation. Shear wave velocity is mainly influenced by Young's modulus. By obtaining the shear wave speed in target tissue medium, localised stiffness of tissue can be conveniently converted by Eq. 3-18. As a relatively developed technique, shear wave elastography is already applied in diseases diagnosis, especially in tumor detections in liver and breast [153, 154]. However, shear wave elastography is not suitable to apply to superficial tissue since shear wave energy on material surface is weak.

3.4 Characterisation and application of SAW

3.4.1Velocity

Most commonly used SAW is stimulated by impulse stimulation. An impulse responded SAW is normally bipolar, strong in amplitude, broadband in frequency, and propagates on the surface of a material. On ideal homogeneous flat elastic solid, SAW shows no dispersion and travels at a constant velocity as described in Eq. 3-19.

$$C_R = \sqrt{g}C_s \approx \frac{0.87+1.12\upsilon}{1+\upsilon}\left(\frac{E}{2\rho(1+\upsilon)}\right)^{\frac{1}{2}} \tag{3-19}$$

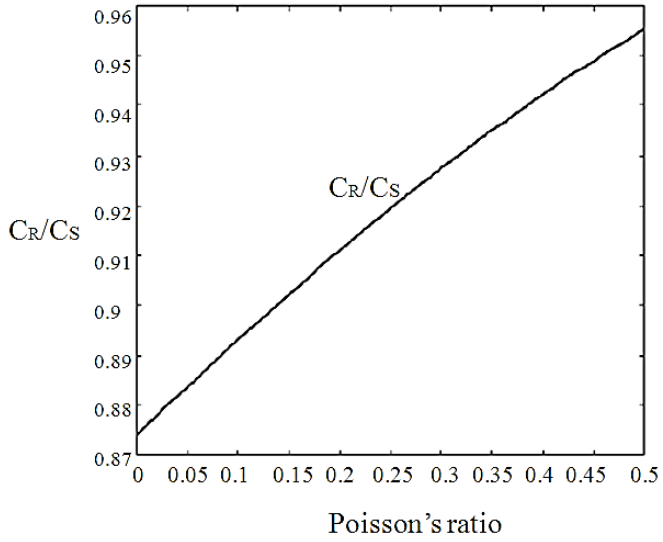

Fig. 3.6 The ratio C_R/C_S as a function of the Poisson ratio

Similar to shear waves, the speed of SAW is much slower than longitudinal waves. The ratio between the shear wave velocity and SAW velocity as a function of the Poisson ratio are illustrated in Fig. 3.6. The exact range of variation of the SAW velocity is $0.87<C_R/C_S<0.96$ when Poisson's ratio varies from 0-0.5. As shear wave speed can be easily found in literatures for materials (steel, iron and agar), thus, this figure can be served as a cross-validation for measured SAW that used for feasibility study in this study.

From Eq. 3-19 it can be observe that the Young's modulus has the most significant impact to the SAW velocity in soft tissues, as the density and Poisson's ratio in soft tissue do not vary much (0.45-0.49 for Poisson's ratio and 1000-1400 kg/m^3 for density). Thus in most of this study, the density and Poisson's ratio are assumed from literatures, to estimate the Young's modulus of the material.

3.4.2 Dispersion

SAW propagate on the stress-free surface, for example the interface of air-solid. The particle displacement decays exponentially with depth and becomes negligible for a penetration depth of more than a few wavelengths. The particle motion can be decomposed into two orthogonal components, one in the direction of SAW propagation and one perpendicular to the free surface.

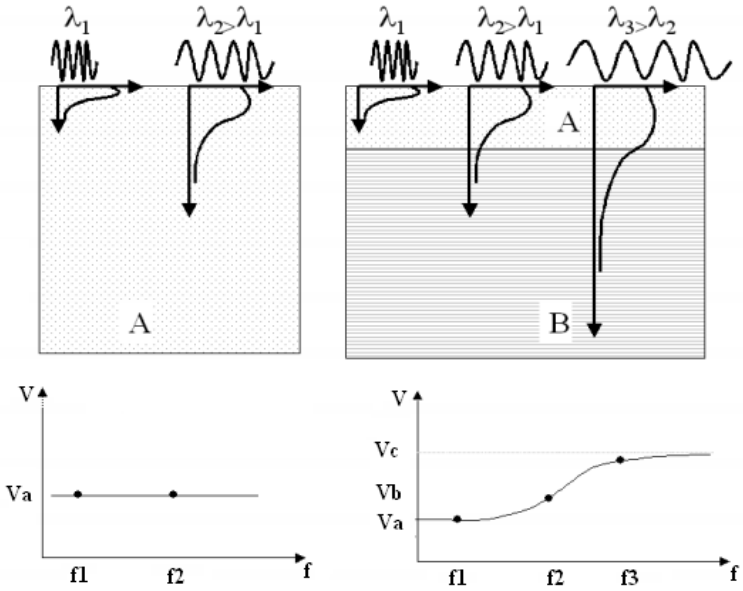

Fig. 3.7. In homogeneous material (left), the phase velocity is constant while in layered material (right), the wave dispersion occurs because the phase velocity depends on the frequency. f is the corresponding frequency of the SAW component with a wavelength of λ.

In homogeneous materials (Fig. 3.7 right), SAW is non-dispersive and therefore its phase velocity is independent of the frequency. However, a layered material perturbs SAW's propagation at the surface. The propagation of SAW in layered materials shows a dispersive behaviour, where dispersion means that in SAW the different frequency components have different phase velocities. For a multilayer medium (Fig. 3.7 left), in which different layers have different elastic properties, the phase velocity of SAW is influenced by the mechanical properties of all the layers it penetrates into. By analysis the phase velocity curve, the true elasticity conditions of a material can be revealed, where a phase velocity dispersion curve can be defined as the phase velocity associated to the maximum spectral density at each frequency, that is, at each frequency, the phase velocity at which most of the energy propagates. The elastic properties that affect the phase velocity dispersion curve include not only the Young's modulus, Poisson's ratio and density of each layer, but also the thickness of each layer. In this case, SAW with shorter wavelengths (higher frequency) penetrates in shallow depth with the phase velocity depending on the superficial layers. On the other hand, SAW with longer wavelengths

(lower frequency) penetrates deeper in the material as the phase velocity will be influenced by the elastic properties of the deeper layers.

It is this characteristic which allows SAW to be used for material characterisation of thin layered materials as waves of different frequencies can be used for the characterisation of different length scales [155-157]. The probing depth can be estimated by the following relation:

$$z \approx \lambda = C_R / f \tag{3-20}$$

where f is the signal frequency.

3.4.3 Frequency range

With impulse stimulation, a broad band SAW can be generated. The max frequency component is shown in Eq. 3-21 (where r_0 indicates the radius of pulse stimulation).

$$f_{\max} = \frac{2\sqrt{2}C_R}{\pi r_0} \tag{3-21}$$

The maximum frequency component that a SAW signal can reach is proportional to the SAW velocity of the material, and inversely proportional to the radius of pulse stimulation. Thus, stiffer materials have broader frequency band than softer materials. In addition, the frequency bandwidth that stimulator can generate also decides the maximum frequency a SAW signal can reach. The shorter impulse stimulation, the broader frequency bandwidth a SAW can be generated. The balance between material stiffness, stimulator radius and stimulator pulse time is important.

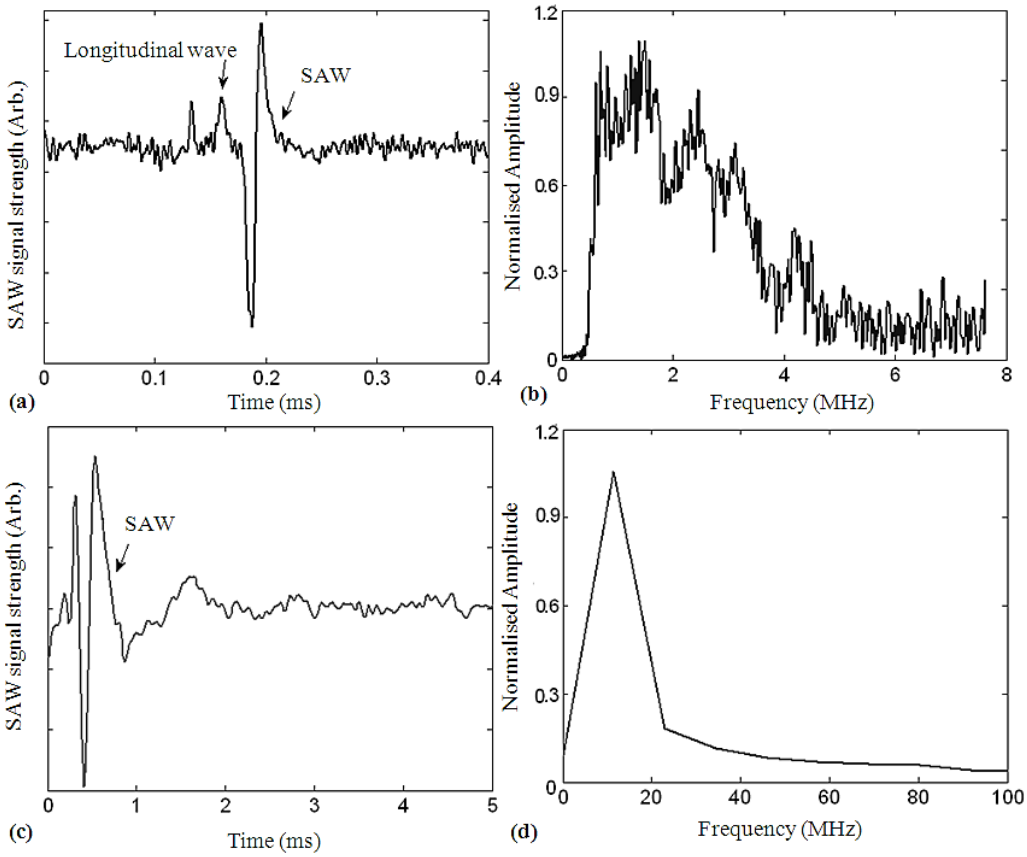

Fig. 3.8 Typical surface waveform and corresponded frequency spectrum of steel (a, b) and tissue mimicking agar phantom (c, d)

SAW have broad bandwidth of frequency (up to 6MHz in hard solid, e.g. metal and 5-50 kHz in soft biology tissues) and different frequency components indicate the corresponding depth propagate into the sample surface. The typical impulse generated SAW waveforms steel and agar phantom can be observed in Fig. 3.8 (a) and (c). Fig. 3.8 (b) and (d) shows the corresponding frequency bandwidth. SAW signals have strong amplitude and can propagate very far from the stimulator. In addition, there are researches about the CW source generated SAW [158-160]. However, CW generated SAW have no dispersion behaviour and very limited frequency bandwidth, thus it is not commonly used and has limited applications.

3.5 Applications of SAW method

SAW method is mainly used to evaluate the mechanical properties of material because of its advantages in quantitatively assessing Young's modulus of both axial and lateral directions, which cannot be fulfilled by longitudinal wave and shear wave. The propagation of SAW in heterogeneous medium (e.g. layered materials) shows a dispersive behaviour, which has been explained in pervious sections. The phase velocity values are directly related to the Young's modulus so that the quantitative elasticity information of every layer the SAW propagate into can be obtained. With these intrinsic properties of SAW, SAW method has a promising potential in estimating the properties of layered material, e.g. coated material [161-166] and layered biomedical tissues (e.g. skin) [167-171].

In addition to being widely used in industry applications such as non-destructive examination/testing (NDE/NDT) of the metallic specimens [167-171], SAW also attract medical applications. Wang *et al.* was the first to describe an application of laser induced SAW for clinical dental diagnosis [172, 173]. In their study simulations the laser damage threshold and the appropriate laser pulse repetition rate have been determined. They concluded that dental enamel has two consistent absorption peaks. The calculated absorption coefficients and thickness suggest that this method shows potential for the NDE of dental enamel. This work is being followed by some initial tests using an erbium doped fibre laser operating at 1550nm wavelength to generate SAW on human enamel specimens to gain further understanding of the wave characteristics.

The first report to evaluate the elastic properties of soft tissue rather than solid materials was by L'Etang and Huang [167, 168]. With the use of finite element (FE) modeling, a three layers' two dimensional skin model has been made with some assumptions and simplifications made. The laser pulse with a Gaussian spatial and temporal distribution with light intensity decreasing axially is directly illuminated onto the skin, thus being a source in the FE analysis. With the simulation combining thermal field and strain-stress field, the SAW waveforms and data can be obtained. However, SAW has not been applied to soft material/soft tissue elasticity measurement practically. Thus, the behaviours of SAW in soft material remain unknown.

3.6 Conclusion

SAW has been widely used in industry for layered metallic material elasticity measurement. Limited applications been developed in clinic field, i.e. dental diagnosis. Except for the FE simulation, no research about SAW' application in soft tissue has been reported.

However, there are great potential to use SAW method in skin elasticity measurement: 1) domain energy of SAW is located near surface of material; 2) SAW has dispersion behavior, elasticity information of different layers of skin can be obtained from one data set by analysis SAW phase velocity curve. In the following chapter it will use the finite element method to simulate the generation and propagation of laser induced SAW in some material models with known results which will be used for verification purposes. The work in the following chapter will aid the development of an accurate method of simulating the generation and propagation of ultrasound in human skin models which will help develop the method and its use for the characterization of human skin properties.

Chapter 4: Development of SAW method in soft solid

4.1 Introduction

SAW method has been widely applied in industry to analysis the mechanical properties and layered structures in hard solid (especially metals), but rarely in medical area with soft solid. Thus, in this project, the simulation appears to be even more important: 1) to determine if the detected wave is SAW in practical experiment; 2) to show the behaviour of SAW in soft material; 3) to optimise SAW generation and detection systems and 4) provides guidance for the future experiments. In this chapter, the finite element method (FEM) as well as its process in ANSYS is introduced firstly to give a general sense of the simulation technique.

In this study, different sets of modelling have been done. It starts with metallic models (one layer steel), aiming to verify the FE method with a published results. Afterwards, it can move onto soft solid models (agar phantoms and *in vivo* human skin).

As mentioned before, the results from simulation can provide as a good reference for the experimental results cross validation. After the simulation study, the experimental stimulation and detection of SAW will be introduced in this chapter. The stimulation approaches include pulse laser and home-made shaker, while the detection approach include low coherence interferometry, laser vibrometer and phase sensitive optical coherence tomography (PhS-OCT). Different samples will be tested, from homogeneous metal to soft agar phantoms. The experimental results will be compared to the computer simulation results to prove the SAW can be successfully generated and detected in soft solid, thus prove the feasibility of the project.

4.2 Finite Element Simulation using ANSYS

ANSYS is a powerful software for FEM, which is an analysis tool incorporating pre-processing (geometry creation, meshing), solver and post-processing modules either in a graphical user interface or through codes. These are general-purpose finite element modeling packages for numerically solving mechanical problems, including static or dynamic structural analysis (both linear and non-linear), heat transfer and fluid problems, as well as acoustic and electro-magnetic problems. ANSYS is chosen for the simulation as a computer aided tool.

In this study, the FE simulation with ANSYS starts with a single layer steel model and then moves to soft tissue mimicking phantom. The results from single layer steel model will be compared with literature, thus procedures of FE simulation in this study will be validated. The study of soft tissue mimicking phantom can be then regarded as a guidance to verify following experimental results of soft tissue and skin. To realise a simulation, there are generally three phases involved in the ANSYS: pre-processing, solver and post-processing.

The pre-processing part of the finite element analysis involves preparing the data required in order to run the simulation. There are three main steps in the pre-processing stage of the analysis

- Definition of the key points/lines/areas/volumes. This includes the nodal coordinates, connectivity, boundary conditions;
- Definition of element type and material/geometrical properties;
- Mesh preparation of lines/areas as required.

In the pre-processing, the axisymmetric model is analysed here instead of a real 3-D model to save the calculation time of ANSYS. The model is 4 cm in radius and 1cm in thickness and axisymmetric to the input laser pulse as showed in Figure 4.1.

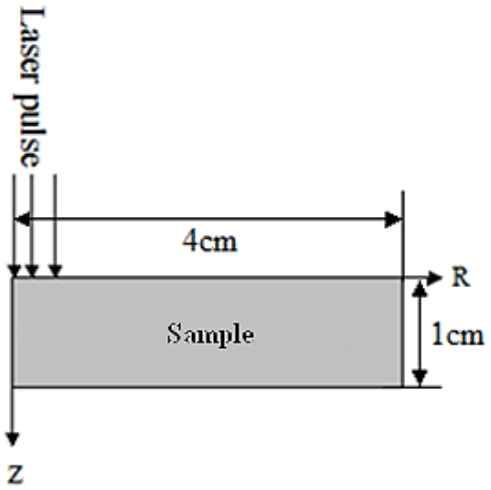

Fig. 4.1 Schematic of the laser interaction on the single layer model

PLANE 55 elements (Fig. 4.2(a)) are used throughout the thermal analysis. This element is a 2D thermal plane solid with four nodes and a single degree of freedom

(Temperature) at each node. This element was chosen due to its axisymmetric behaviour capability which significantly reduces the required computer resources and the run time for the simulations from using a 3D solid element. This element is applicable to a 2D steady-state or transient thermal analysis and is replaced in the structural analysis with the equivalent structural element (PLANE42 (Fig. 4.2(b)). PLANE 42 is a 2-D element used for the modelling of solid structures. This element can be used as a plane element (with plane stress or plane strain) or with axisymmetric behaviour. In the simulations presented in this work it is assumed to have axisymmetric behaviour. PLANE 42 is defined by four-nodes with two degrees of freedom at each node: translations in the nodal x and y directions. This element has plasticity, creep, swelling, stress, stiffening, large deflection and large strain capabilities.

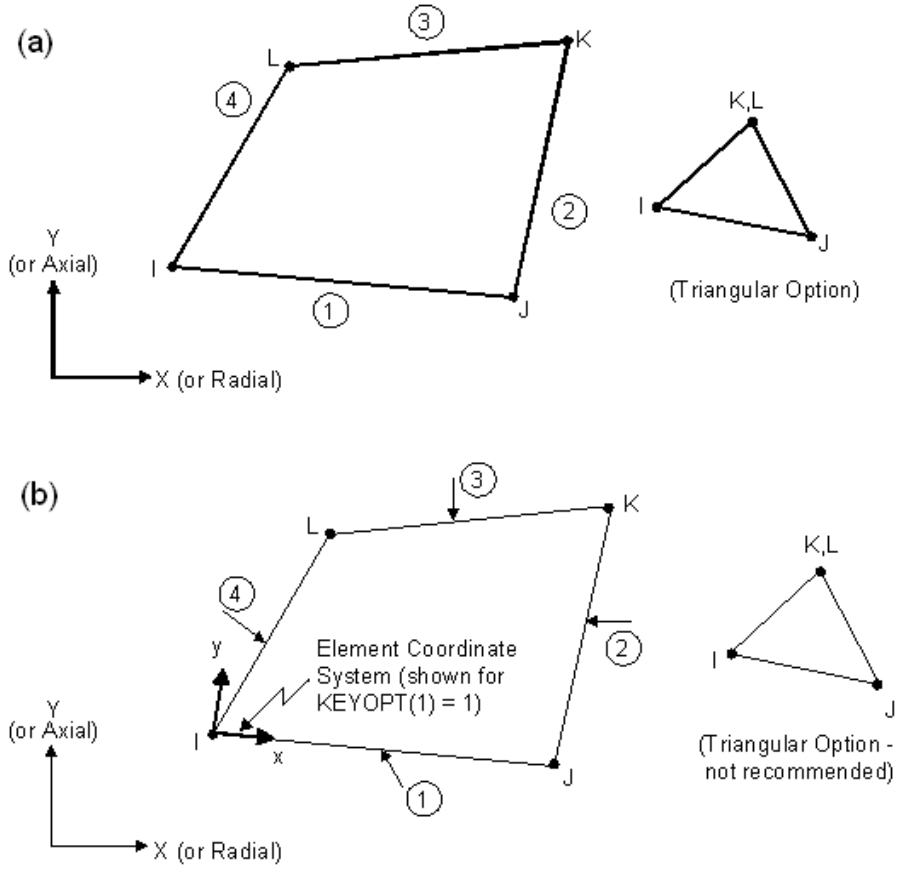

Fig. 4.2 Geometry of plane 55 (a) and plane 42 (b) in ANSYS [167]

Temporal and spatial resolution of the finite element method is critical for the convergence of the finite element model. The optimisation is critical in order to avoid

unnecessarily high hardware requirements and enormous calculation times. For generated SAW in this study, the highest frequency determines the integrate time and the lowest wavelength determines the element length. For a compromise of accuracy and time saving, Newmark time integration scheme is applied here to calculate the integrate time and element length as follows:

$$\Delta t = \frac{1}{20 f_{\max}} \tag{4-1}$$

$$l_e = \frac{\lambda_{\min}}{20} \tag{4-2}$$

where Δt is the integrate time and l_e is the element length. The f_{max} refers to the highest frequency and λ_{min} refers to the lowest wavelength.

Even though the Newmark time integration scheme provides a good reference for meshing control, testing is still needed to verify its convergence. Therefore some convergence testing of the models is performed where a set of models are simulated with different meshing densities. First a relative coarse meshing will be done and analysed once. Then a finer meshing is processed the same way for a comparison with the previous result. If they varied considerably, it indicates that the meshing are still required to be improved, so the same procedure is repeated. But if they are similar, the prior meshing is appropriate. Otherwise, there are two meshing types in ANSYS, free mesh and mapped mesh. Free mesh is a default meshing technique by the software, but without restriction to shape which is suitable for meshing irregular models. On the contrary, mapped mesh will confine elements either to a triangle or a quadrilateral for a 2-D model (hexagon for a volumetric model) and typical for meshing a regular model. Thus, the mapped mesh is selected here. The areas near the laser irradiation and near sample surface is the most sensitive section hence should be meshed with the minimum elements in the size of 5 μm. And with an increasing distance further away laser source, the areas are less sensitive to laser and heat. Thus, they are meshed with larger elements from 20 μm to 100 μm, which is still small enough to meet the demand of the accuracy of generated SAW propagation. Time increments in the simulation are kept very small, in the order of 0.1ns during the duration of the pulse, and are allowed to increase after the termination of the pulse. The thermal analysis was run for a time of 1 μs in order to provide temperature histories for the full time duration of the mechanical analysis due to the slow diffusion of heat. The

mechanical analysis was run for a time of 500 μs in order to track the full generated SAW within 2.5mm away from the laser pulse.

There are a number of assumptions that are made in this simulation, including:

- Thermal expansion that occurs due to laser heating occurs over a time span close to that of the pulse duration;
- Material is treat as pure elastic material, viscosity is ignored;
- Thermal losses due to radiation and convection are ignored;
- Material properties are independent from thermal change.

The laser pulse is assumed as a Gaussian laser pulse. The factor of spatial distribution is described as follow:

$$F(r) = \exp(-r^2/r_0^2) \tag{4-3}$$

where r is the radius coordinate, r_0 is the radius of laser pulse. The factor of the Gaussian temporal distribution is described as:

$$G(t) = (t/t_0)\exp(-t/t_0) \tag{4-4}$$

where t the laser exposure is time and t_0 is the pulse rise time. The laser pulse has different effects on optically dense medium and optically thinner medium. For example, metals are generally optically dense thus the laser pulse can hardly go through the metallic surface. During the short pulse duration, the laser energy can just be absorbed by a depth strictly confined to the surface. The thickness of the absorption area is typically in the order of 5-10nm. In other words, the laser affected area in metallic samples is very thin and this type of laser effect is called the heat flux. An expression used to describe the heat flux irradiance is as below,

$$I_d = I_0 \cdot F(r) \cdot G(t) \tag{4-5}$$

where I_0 refers to the central irradiance of laser pulse. In the steel simulation, Eq. 4-5 is used. However, the case is not the same with soft biomaterials, where the laser pulse will penetrate a significant depth into the tissue. Accordingly, the laser affected area is extended into the materials interior and this kind of mechanism is defined as the heat generation. In this case, the irradiance can be described as follows,

$$I_d = I_0 \cdot \mu_a \cdot F(r) \cdot G(t) \cdot \exp(-\mu_a z) \tag{4-6}$$

where μ_a is the absorption coefficient and z is the coordinate describes the depth below surface. Eq. 4-5 is used in steel simulation while Eq. 4-6 is suitable in agar simulation.

The set-up in thermal analysis is kept the same with the available laser pulse source available in the lab where the applied laser energy is 3 mJ, the laser pulse rise time is 3 ns. The thermal and mechanical parameters of steel and tissue mimicking agar phantoms with concentrations of 2% are listed in Table 4.1.

Table 4.1 Properties of steel and tissue mimicking agar phantoms used in FE Analysis [171, 175]

Parameters of material	Steel	2% agar phantom
Young's Modulus (kPa)	6.9×10^{7}	180
Poisson's Ratio	0.34	0.47
Density (kg/m^3)	2.77×10^{3}	1.04
Thermal Expansion coefficient (K^{-1})	2.31×10^{-5}	$3.0\text{x}10^{-4}$
Specific Heat ($Jkg^{-1}K^{-1}$)	875	3590
Thermal Conductivity ($Wm^{-1}K^{-1}$)	394	24

4.3 Preliminary FE simulation results

Fig. 4.3 shows out of plane displacement at various surface points across the time-history which is also a representation of the laser induced SAW. It can be seen that the wave amplitude is in the order of nm and decreases exponentially. This conclusion is a good guidance to choose an appropriate measuring instrument and valid detecting points. In this case, the optical interferometer should be an ideal instrument for detecting such a tiny displacement.

As mentioned in Chapter 3, the SAW and the shear wave are always coupled with each other however the longitudinal wave will be distinguished during the propagation of the SAW. This point is also proven by the simulation result. As it can be seen in Fig. 4.3, at first the three waves are mixed together near the original point, however after the point at 2.5mm, the longitudinal wave starts to be separated from the other two and the separated longitudinal wave is marked by ' L '.

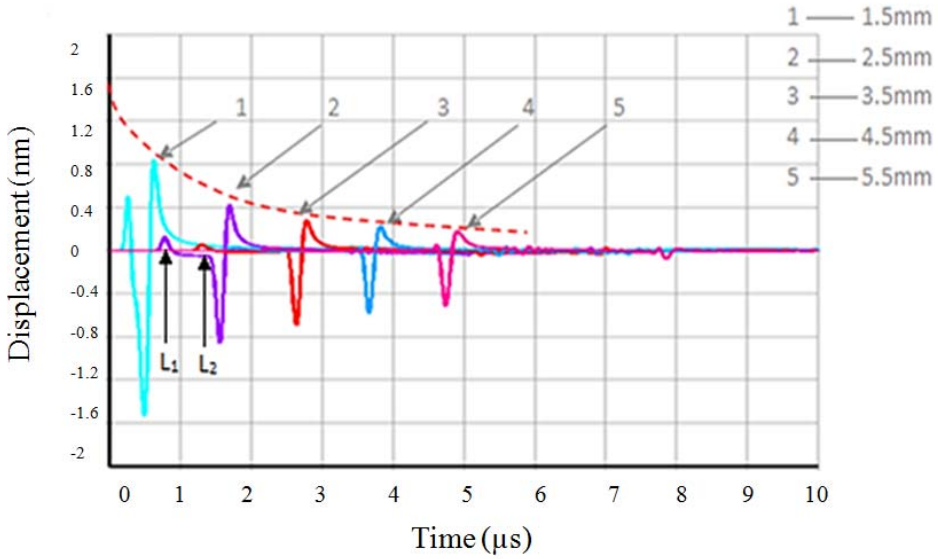

Figure 4.3 Out of plane displacement of generated waves detected at various surface points on the single layer steel model. Number 1-5 indicate detection points from 1.5mm to 5.5mm to laser pulse; L_1 and L_2 indicate the longitudinal wave of SAW.

Fig. 4.4 shows the typical SAW signal of one layer 2% agar phantoms from FEM analysis. Each signal waveform is purposely shifted vertically by equal distance in order to better illustrate the results captured at different positions. The horizontal dotted lines indicate the baseline (this will apply for the SAW signal figures of rest of the thesis). The first detection point was from 0.5mm to the laser pulse, the detection point will be moved with 0.5mm/step to 2.5mm away. It could be easily seen that the SAW was moving away from the laser pulse. Because the sample was one layer homogeneous sample, thus no dispersion could be found in the waveforms. Compared with the SAW signals in hard materials such like metal, SAW in soft solid have much greater wavelength and travel at a much slower speed. The amplitude of SAW from FEM results was around 5nm. In addition, a clear attenuation between the waveforms was observed.

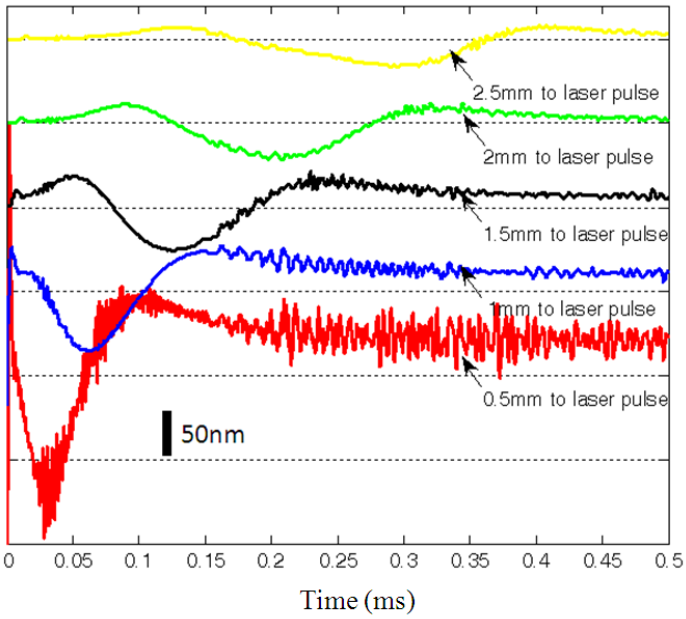

Figure 4.4 SAW of one layer 2% agar phantom with the distance of 0.5mm to 0.3mm to laser pulse, with 0.5mm/step from FEM simulation

The key features of SAW generated from FE simulation will cross-validate the detected SAW from practical experiment, i.e. the wave form, velocity and frequency range of the waves.

4.4 Experimental Stimulation

As mentioned in Chapter 3, many approaches can be utilised to stimulate SAW. In the whole project, high energy Q-switched laser pulse and a mechanical shaker are used to induce the SAW which propagates on the material surface.

4.4.1 Q-switched laser pulse

When a material is illuminated with a short laser pulse, the energy is absorbed through various mechanisms. These mechanisms include radiation pressure, electrostriction, Brillouin Scattering and the thermoelastic mechanism. The mechanism involves a change of state of the material, i.e. the ablation (Fig. 4.5(a)) which is caused by the high laser energy illumination. On the other hand, in lower laser energy illumination, the mechanism will not alter the tested material, which is called thermoelastic mechanism (Fig. 4.5(b)).

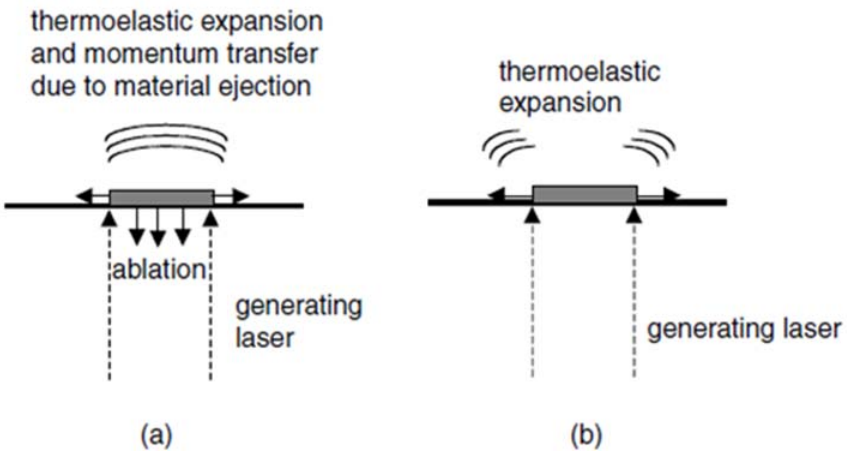

Fig, 4.5 Laser generation of SAW in (a) ablative regime and (b) thermoelastic regime.

The ablative regime will destroy the sample surface. For example, it will destroy steel with approximately 0.3 mm each time. The plasma that is generated from the ablative regime will cause a continued heating and destroy steel surface within about 1 μs. Thus, it is typically unacceptable for non-destructive characterization of materials.

The laser generated SAW by the thermoelastic mechanism is a complex process that involves the optical, thermal and mechanical properties of the material being tested. The thermoelastic mechanism is generally the most dominant method in NDT. A pulsed laser beam impinges on a material and is partially absorbed by it, which results in a rapid increase in temperature of the irradiated area that in turn causes a rapid thermal expansion. Because there is no restraining force to the surface of the sample, the sample is free to expand outward away from the bulk of the material. The material is not free to expand parallel to the surface of the sample, which leads to a generation of strong elastic wave pulses. The generated elastic waves act radially outward from the centre of the heated zone in the plane of the surface. The consequence is the generation of ultrasonic waves that propagate within the material, such as body waves, and propagate on the material surface, such as SAW. The amplitude of the SAW is linearly proportional to the power density of the laser pulse.

If the duration of exposure to laser radiation is long, significant quantities of heat will diffuse out of the target volume during irradiation, reducing the efficiency of the SAW generation. For efficient SAW generation, the duration of the optical pulse should be

sufficiently short so that both thermal and stress confinements take place. In order to fulfil the condition of thermal confinements, the optical pulse duration should be short compared to the thermal relaxation time of the heated volume so that there is no significant loss of heat by thermal diffusion during the heating process and the process of heat deposition is faster that of thermal expansion.

The advantages of laser induced SAW include:

- Noncontact (coupling problems eliminated and no surface loading);
- Remote (access to sample in hostile environments);
- Rapid scanning capability;
- Allowing operation on geometrically awkward specimens;
- Broadband;

The disadvantages of such method include:

- Relatively expensive;
- Generation efficiency is a function of material optical absorption properties;
- Requiring laser safety precautions;

In the experiment, a solid state Nd:YAG laser (532 nm central wavelength) (Continuum Surelite Laser) was used as the high energy laser pulse source. The short laser pulse was set to duration of 6 ns (rise time 3ns) with an average energy of 2.6-3 mJ and repetition rate of 0.5 Hz. During the experiment, the laser irradiation on the samples (i.e. metals and tissue mimicking phantoms) was continuously monitored by a recording camera to make sure that there was no surface damage or melt under the energy level which is used. Before laser pulses impinge to the sample, a cylindrical lens was employed to generate a line source with the line length of 2-2.5 mm. From the literature [191, 192], it is proven that line source generated by a cylinder lens has the following advantages:

- It permits an improved signal/noise ratio for measured surface wave-forms compared with that for a circularly symmetric source;
- Compared with the focused laser pulse, more energy can be injected into the specimen because the power density is greatly reduced. It will help to avoid damage of material;
- The resulting wave field is highly concentrated in the direction normal to the line source.

To fulfil that, reflection mirror and cylindrical lens (shown in Fig. 4.6) were mounted on a translation stage, so that the excitation laser beam was translated to the required distances for the measurement of generated SAW signals. In this way without moving the detection arm, the stability of measured signals from the sample was well kept.

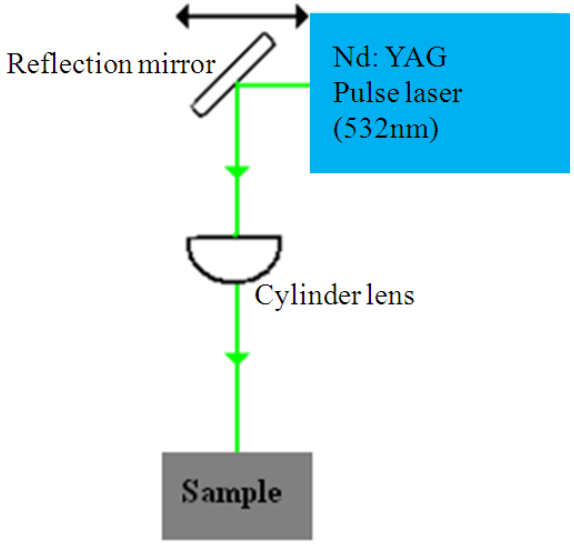

Fig. 4.6 Typical setup of laser stimulation of SAW

4.4.2 Shaker

Impulse stimulated SAW can also be fulfilled by a mechanical shaker. Compared to the high energy laser source, a mechanical shaker inducing SAW is a safer, portable and simpler approach. It directly passes the vibration to samples and generates waves. In addition, the amplitude of SAW generated by mechanical shaker is easily controlled and enhanced. In this study, the SAW amplitude was controlled below 100 nm to avoid the tissue behaviour out of linear elastic region that the measurement is not pure elasticity information. The disadvantages of using a mechanical shaker to induce SAW include the contact with the sample during detection. It brings surface loading which is inapplicable in certain clinic environments. It thus has requirements of specimens' geometry and material conditions. In addition, it has limited frequency bandwidth.

A specially designed shaker was used as the mechanical impulse stimulator in this study, which included a signal generator, and a single element piezoelectric ceramic with

a metal rod (length of 20 mm and diameter of 2 mm) connected in the end as the shaker head (Fig. 4.7).

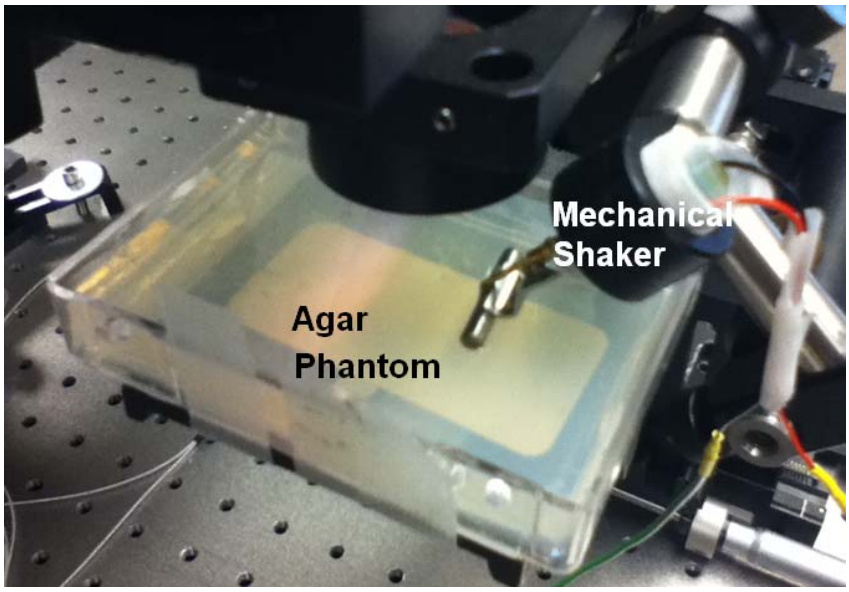

Fig. 4.7 Mechanical shaker induced SAW for measuring agar phantom elasticity

During the experiments, the metal rod was directly in touch with the sample to pass the vibration from the piezoelectric ceramics to stimulate the SAW on the sample surface. The stimulus was applied with a 45 degree angle to the tissue surface, which provided equal longitudinal and shear energy to the sample, and improved the amplitude of the SAW. Compared to the point source, the line source (provided by the metal rod) improved the SNR, and reduced the attenuation of the SAW, which enabled the SAW to propagate longer distances. The shaker applied a tissue displacement of 100nm maximum in the axial direction. The tissue displacement is proportional to the SAW amplitude. The amplitude has no influence to the shape and velocity of SAW.

To analyse all the frequencies from the SAW, the shaker is required to generate a pulse with a short duration. For this study an external trigger is used to control the shaker which generated pulses of 20Hz with a 0.2% duty cycle; producing frequencies up to 10 kHz.

4.5 Experimental data Acquisition

In the project, optical methods were used to detect SAW, which include low coherence interferometry and phase sensitive optical coherence tomography (PhS-OCT). Optical

detection methods are non-contact and have broader bandwidth, which is ideal for the clinical applications.

4.5.1 Low coherence interferometry

Detection of the laser-induced SAW can be performed by a low coherence interferometry system (Fig. 4.8). There are several reasons to adopt the low coherence interferometry as the detection method in this project. Firstly, compared to conventional interferometry, the low coherence interferometry is able to lock the detecting point on the sample surface within a depth defined by axial resolution of the system (which is determined by the coherence length of the light source). This is advantageous because when the probe beam is aiming at the surface of the sample, only the SAW signal is detected, which reduces noise from environment. In addition, it can be developed into an OCT imaging system to provide the geometrical structure of samples, i.e., the thickness of layers and the flatness of surface of samples. Thus, this novel combination gives a possibility to offer imaging the geometry and inner layer conditions and elastic properties of tissue at the same time.

Interference is the superposition of two or more waves, resulting in a new wave pattern. When two light beams are combined, their fields add and produce interference. The principle of low coherence interferometry can be analysed in terms of the theory of two-beam interference for partially coherent light. The light field from a low temporally coherent but high spatially coherent light source is directed onto a beam splitter that divides the beam into a reference beam and a measurement beam. Assuming that the sample is a perfectly reflecting mirror and the polarisation effects of light are ignored, the scalar complex functions $E_s(t-L_s/c)$ and $E_r(t-L_r/c)$ represent the optical field of sample beam reflected from the specimen under measurement and the optical field of reference beam from the reference mirror, respectively. L_s and L_r are the corresponding optical path lengths of the arms of the interferometer and c is the speed of light. If assume that the photo detector collects all the light from the arms, the resultant intensity I_d can be written as:

$$I_d(\tau) = \langle [E_s(t) + E_r(t+\tau)][E_s(t) + E_r(t+\tau)]^* \rangle \tag{4-7}$$

where the angular brackets denote the time average over the integration time at the detector and $\tau=\Delta L/c$ is the time delay corresponding the round-trip optical path length

difference between the two arms, i.e. $\Delta L = L_s - L_r = 2n(l_s - l_r)$, and the asterisk symbol means the complex conjugate operation. n ≅ 1 is the refractive index of air, and l_s and l_r are the geometric lengths of the arms.

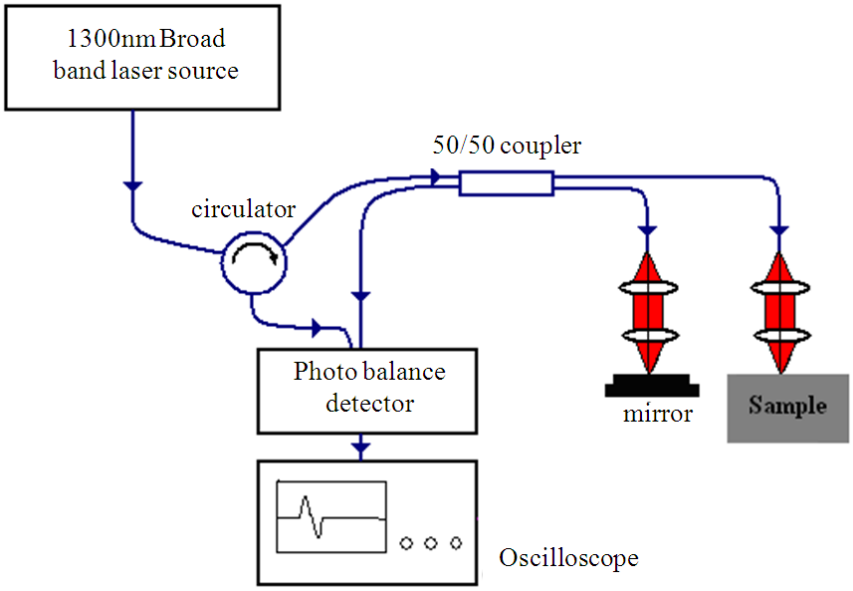

Fig. 4.8 Typical setup of low coherence interferometry

In the experiment, the low coherence interferometry system (Fig. 4.8) consists of a 1310±28 nm broadband superluminescent diode (SLD, Dense Light Ltd.) as the light source, a 3-port optical fibre circulator, a 4-port 50/50 optical fibre coupler, a balanced amplified photo detector (PDB120C-75MHz), a reference arm and a sample arm. To summarise, light from low-coherence broadband light source split into two paths in a 50/50 fibre based Michelson interferometer. One beam is coupled onto a stationary reference mirror and the other is focused onto the phantom samples via an object lens. As mentioned before, the sample arm and agar phantom are fixed in order to maintain the stability of measured signals.

The measured signal can be expressed as:

$$I(k) = 2\sqrt{I_1 \cdot I_2}\cos(\varphi + 2k\Delta z + \varphi_{noise}) \tag{4-8}$$

where $k = 2\pi/\lambda$, Δz is the change of optical path caused by laser induced SAW signals, φ is the initial phase difference due to the optical path length difference between the sample and reference arms, which was carefully adjusted to be $\pi/2$, and φ_{noise} is a random low frequency phase noise due to the optical system noise and environment vibration. The

value of $I(k)$ changed constantly due to the random noise φ_{noise}. During the detecting procedure, $I(k)$ was monitored by a digital oscilloscope (Tektronix TDS5104B Digital phosphor oscilloscope). The detection system record the SAW signals only at the times that $\varphi+\varphi_{noise}=\pm k\pi+\pi/2$ when the system became most sensitive. However, ambient vibrations, e.g., building vibration and room temperature fluctuation, often cause an additional optical path length change, which sometimes can be more than what is expected to detect, leading to a fluctuating sensitivity for the system. To mitigate the problem of ambient vibrations, a synchronisation method is used to lock the system working at its highest sensitivity to the surface displacement caused by the SAW. Because the highest sensitivity of the OCT system to the vibration is at the point when the OPL equals to $k\pi+\pi/2$, the zero crossings of the DC output signal of the balanced detector are tracked. Only when the DC output crosses the zero point will the excitation laser be triggered, and at the same time a trigger signal is sent to the digital oscilloscope for sampling the signals. As a result, the system was locked to its highest sensitivity. This allowed the detection of SAW signals under similar conditions. However, the real displacement cannot be obtained by low coherence interferometry system.

4.5.2 Phase sensitive optical coherence tomography system (PhS-OCT)

Detection of SAW can also be performed using a phase sensitive optical coherence tomography (PS-OCT) system. The OCT imaging system can provide the structural image of the samples as a function of depth, i.e., the thickness of each layer. This system allows imaging the tissue's inner layer structures as well as its elastic properties simultaneously.

The PS-OCT system (Fig. 4.9) employed a spectral-domain OCT (SD-OCT) system with a centre wavelength of 1310 nm and a bandwidth of 46 nm from a superluminecent diode (SLD, Dense Light Ltd.) as the light source. It provided an axial resolution of 15 μm in air (10 μm within the skin, assuming the refractive index is 1.4). Via an optical circulator, the light from the SLD broadband light source was split into two paths in a 50/50 fibre based Michelson interferometer. One beam was coupled onto a stationary reference mirror and the second was focused onto the phantom samples via an objective lens. The focal length of the objective lens was 50 mm to provide a transverse resolution of 18 μm.

The coupler recombined the backscattered light from the sample arm and the reflected light from the reference arm into a home-built, high-speed spectrometer via the optical circulator. The interference light was then coupled into a fast spectrometer equipped with a 14-bit, 1024 pixel InGaAs line scan camera with a maximum acquisition rate of 47 kHz. A computer was used to synchronously control the acquisition of the camera and the impulse excitation of the shaker. In this study, the SAW stimulation system and camera are triggered at the same time.

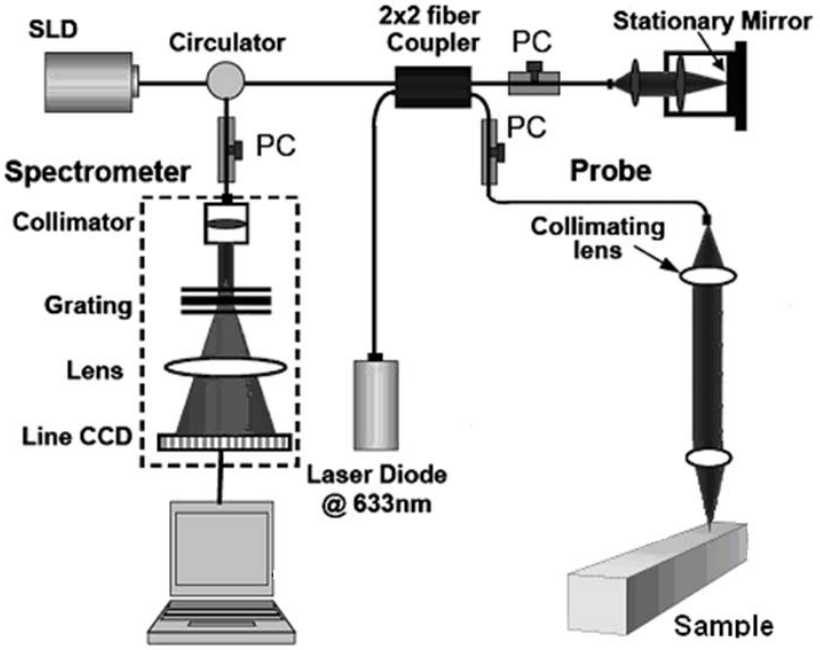

Fig. 4.9 Setup of PhS-OCT system

The interference spectral data that is collected by the PhS-OCT system contains both amplitude and phase information of the light beam. It estimates the axial position of the internal reflective structures in the sample by taking the magnitude of the Fourier function in the space domain. PhS-OCT goes one step further and uses the phase information of the obtained Fourier transform as well. This phase information allows measuring very small time-dependent variations in the optical path delay (OPD). This information is already contained in the PhS-OCT images and does not require additional hardware setup. The intensity of the interference pattern on the spectrometer can be expressed as follows:

$$I(k) = S(k)R_r + S(k)R_s + 2S(k)\sqrt{R_r R_s}\cos(2k\Delta d + \theta) \quad (4\text{-}9)$$

where k is the wavenumber, $S(k)$ is the spectral density of the light source, R_r and R_s are the reflectivity from the reference surface and the sample surface, respectively, Δd is the OPD between the sample and the reference signals, and θ is a constant phase shift.

The first two expressions in the equations are constants for a given setup, so the intensity is modulated by the cosine expression at a frequency set by the OPD. The challenge is to determine the phase expression and extract the depth information:

$$\varphi(k) = 2k\Delta d + \theta \tag{4-10}$$

The system sensitivity in time depends on the stability of this phase expression. If the system has a phase stability or phase jitter of $\Delta\varphi$, the system SNR can be expressed as:

$$SNR = \frac{2}{\pi^2\langle\Delta\varphi^2\rangle} \tag{4-11}$$

To determine the OPD, the phase function needs to be unwrapped. The slope of the phase function is used and combined with the phase value to increase depth precision. To retrieve the phase information, several single-frame techniques have been proposed for the evaluation of the phase. These include Fourier transform, Hilbert transform, spatial phase shifting, windowed Fourier transform, and wavelet transform. The phase reconstructions are more or less identical except for spatial phase shifting, indicating that the reconstruction of the profiles does not suffer from large errors. Temporal phase shifting is a multi-frame method for reconstructing the phase information. This method can obtain accurate results. However, it typically requires five frames. As an example of the full steps required for retrieving the OPD, the use of the Fourier transform method is described next. First, a Fourier transform is performed on the spectral data giving the depth space. A Gaussian band pass filter is then applied on the positive term of the complex depth function to remove noise and unwanted reflections. Then, an inverse Fourier transform is applied to return to wave number space and to give the complex expression:

$$\tilde{I}(k) = 2S(k)\sqrt{R_r R_s}exp[j(2k\Delta d + \theta)] \tag{4-12}$$

The phase term can be retrieved as:

$$\varphi(k) = 2k\Delta d + \theta \tag{4-13}$$

where

$$\varphi(k) = \arctan(\frac{Im(\tilde{I})}{Re(\tilde{I})}) \tag{4-14}$$

To determine the OPD, the phase function needs to be unwrapped. First, a least-square algorithm is used to determine the slope of the phase as a function of the wavelength. Then, the slope of the phase function is used as the reference to remove 2π ambiguity, and one phase component is chosen to give the absolute OPD as:

$$\Delta d = \frac{\varphi(k_i)}{2k_i} + \frac{\pi}{k}\left[floor(\frac{\varphi'}{2\pi})\right] \quad (4\text{-}15)$$

where φ' is the phase that was retrieved from the slope of the phase function.

An example of how SAW can be obtained from 1% agar phantom by a PhS-OCT system is shown in Fig. 4.10. The M-mode image of phantom can be obtained with the OCT system in Fig. 2 (a), black arrow points the surface data selected to analyse the phase change. The surface of phantom have strongest signal due to the high surface reflectivity. Fig. 2 (b) shows the phase change observed at the surface. When shaker gives stimulation to phantom surface, a strong SAW signal can be detected with a very short time delay. To determine the system noise, data from the stage surface were collected when no sample was present (Fig. 4.10 (c)). The system noise detected from the sample stage was much lower than the detected SAW signal in amplitude; and its frequency contribution was negligible as observed in Fig. 4.10 (d). The measured SNR at a 0.5mm axial depth position was 100 dB.

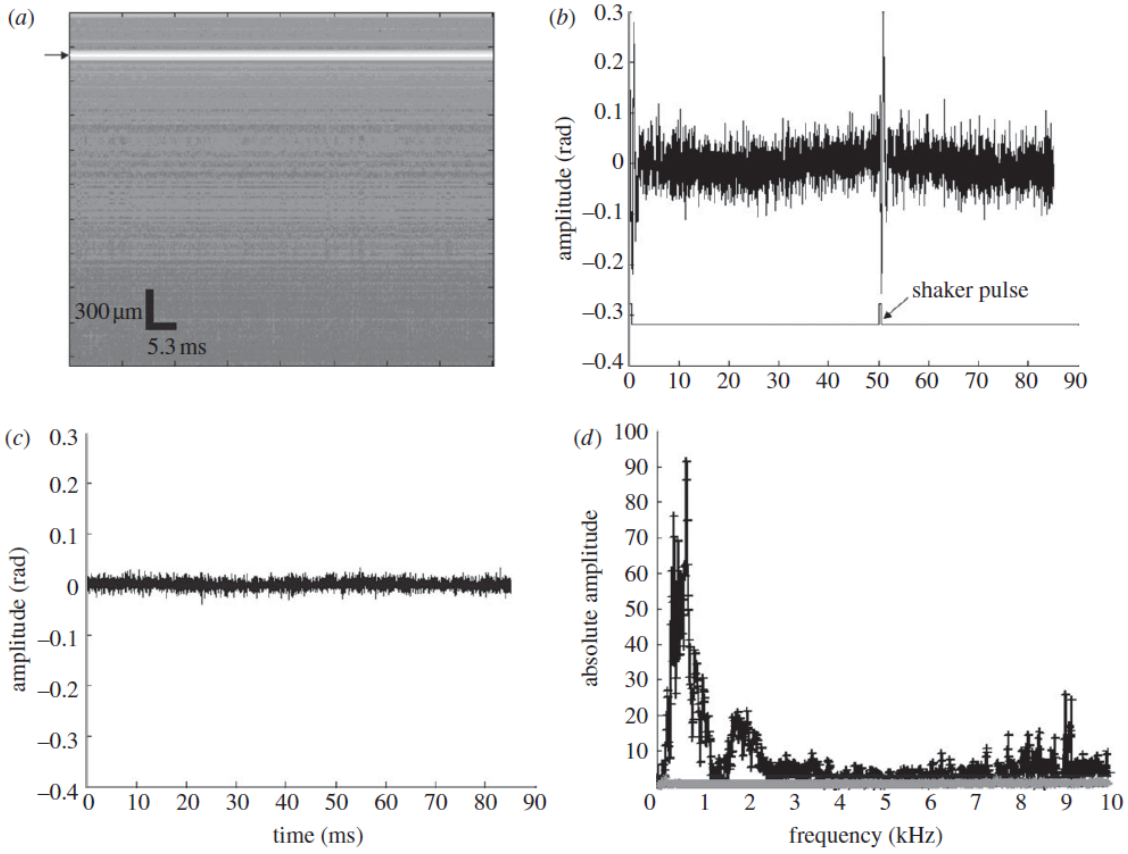

Fig. 4.10 (a) Amplitude data of M-mode PhS-OCT image at the detection point, (b) phase change of the SAW signal and waveform of the shaker pulses, (c) phase change of the detected system noise and (d) frequency contribution of the system noise and the detected surface wave signal.

To calculate the phase velocity dispersion curve of the shaker-induced SAW, several detecting locations with known separations are required. The shaker head needs to be in contact with the sample surface to generate the SAW. To maintain the stability of the generated SAW, the shaker and sample were mounted on a translation stage. During the experiment, the PhS-OCT sample beam was moved to different detecting locations while maintaining the shaker head at a fixed location. At each detecting location 4000-lines were acquired over time at a sampling frequency of 47 kHz, also known as an M-mode acquisition. Since the stimulation had a frequency of 20 Hz, the system was able to detect two phase changes (bottom line in Fig. 4.10 (b)) with a time gap of 50 ms. SAW displacements were calculated using:

$$\Delta z = \frac{\Delta\varphi\lambda}{4\pi n} \tag{4-16}$$

where $\Delta\varphi$ is the detected phase change, λ is the central wavelength of the PhS-OCT system (1310nm), and n is the index of refraction of the sample (1.35).

4.6 Preliminary experimental results

In the preliminary experiments, Q-switched laser pulse are used to stimulate the SAW and low coherence interferometry to detect the signals. It is because the Q-switched laser source can generate a signal with a bandwidth over 150 MHz which will not limit the frequency bandwidth of the generated SAW of the material, and broad band detection (up to 37.5 MHz) allow us to acquire the waves fully so that the characterisation of SAW in soft tissues can be well analysed. Fig. 4.11 shows the typical SAW recorded from steel plate. The excitation laser beam was first located at a position 1 mm away from the detecting point (red), and then moved with 1 mm/step to 6 mm away (magenta). Noise from excitation laser can be found in detected signals from each of the locations (as pointed by red arrow). Fig. 4.11 demonstrates that the SAW is moving away from the excitation position because the arrival time of the surface wave is longer as the detector is located farther away (black diagonal line in Fig. 4.11). In addition, attenuations between the waveforms were clearly observed. Longitudinal wave can also be observed (marked with blue dash line). Longitudinal wave cannot be distinguished well in near laser areas, for example the area is 1mm to laser pulse. Since it has much higher speed that SAW, longitudinal wave is separate from SAW with the increasing of detecting distance.

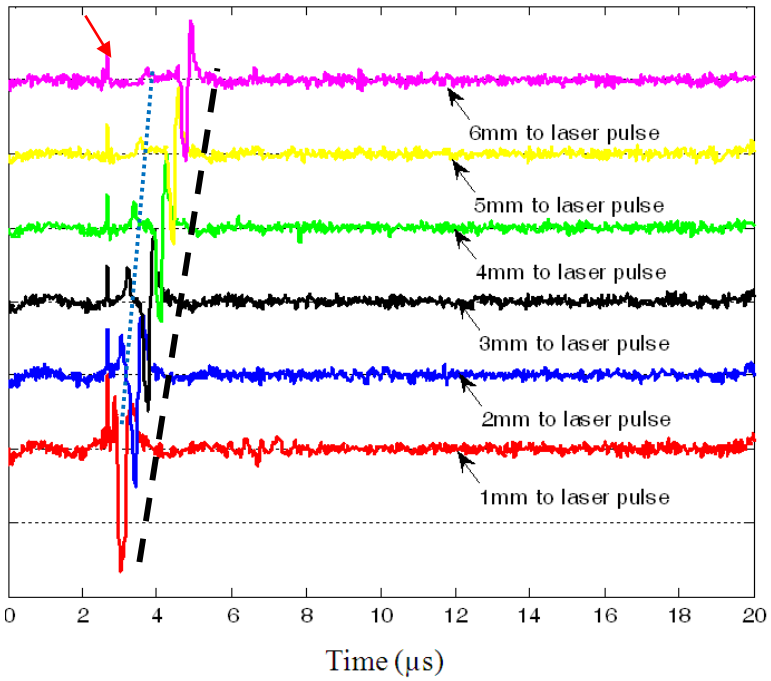

Fig. 4.11 SAW signal of steel plate with the distance of 1mm (top) to 6mm (bottom) to laser pulse, with 1mm/step.

Detailed comparison between experimental results and FEM results is summarised in Table 4.2. Briefly, the experimental results fit well with the FEM simulation results as well as literatures in steel study: 1) the propagating speed of SAW on steel surface is calculated approximately 3000 m/s both in FEM and experiment. This results obtained agrees well with the theoretical value expected for a homogeneous steel samples [176]; 2) the frequency content between experimental results and FEM are similar, the frequency drops to -20dB at about 6 MHz; 3) the SAW waveform is similar in FEM, experiment and published results. The detailed signal processing procedures will be introduced in next chapter. It offer a cross validation to show the experimental procedures and methods are correct. Thus, it can move to the soft tissue analysis.

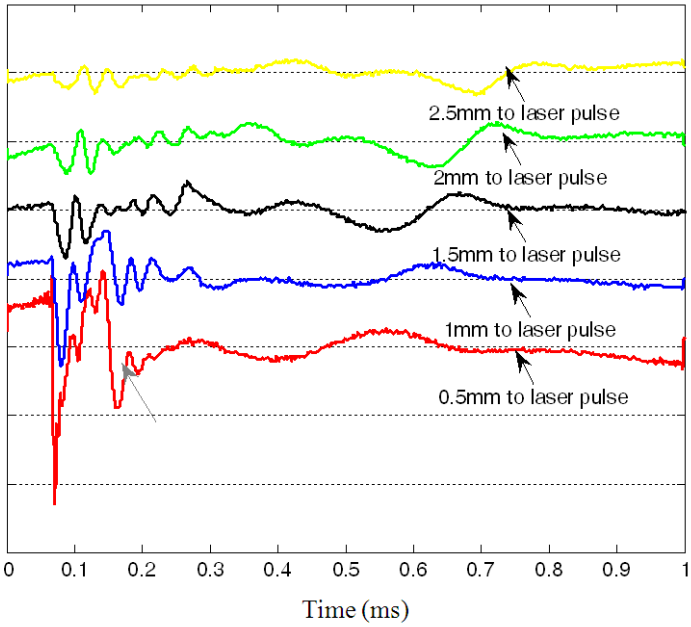

Fig. 4.12 SAW of one layer 2% agar phantom with the distance of 0.5mm to 3mm to laser pulse, with 0.5mm/step from experiment

Fig. 4.12 shows the typical SAW of one layer 2% agar phantom from experiment. Within the same detection protocol of FE simulation, the laser pulse was from 0.5 mm to detecting point, with 0.5 mm/step to 2.5 mm away. As expectation, no dispersion could be found in the SAW signals, as the waveform does not deformed during propagating. The SAW signals from FE simulation and experiment were in a similar shape. Differences were found between the simulation and the experimental results which could be attributed to effects of laser radiation pointed by grey arrow in Fig. 4.12, which led to the high frequency noise when laser pulse emitted on the sample.

Again, it shows that the experimental results are in good agreement (Table 4.2) with those of the FE simulation: 1) the wave velocity is 7.55 m/s in experiment and 7.93 m/s in FEM simulation and 2) the frequency drops to -20dB at approximately 10 kHz in experiment and 11 kHz in FEM. It can be concluded that the simulation procedure developed in this work is a good representation of the SAW method used in soft solids. Therefore, the simulation can act as a theoretical reference for experiments in SAW method for skin diseases diagnosis and treatment. From both of the FE simulation and experiments, it can be acknowledged that the frequency bandwidth of SAW in soft tissue

mimicking phantom is domain in kHz. Thus, the lower requirement of both stimulator and detector for this project is easily accomplished by a shaker stimulator and PhS-OCT which are with limitation of the frequency bandwidth.

Table 4.2 Comparison of experimental and FEM results

	Steel		**2% agar phantom**	
	Experiment	FEM	Experiment	FEM
Velocity	3005 m/s	2996 m/s	7.55 m/s	7.93 m/s
Frequency range	6.0 MHz	5.9 MHz	10 kHz	11 kHz

4.7 Conclusion

Presented in this Chapter was the development of a FEM technique to simulate the generation and propagation of SAW in one layer steel models and soft tissue mimicking phantom models. Since the behaviours of SAW in soft tissue remain unknown, FE simulation is important in this project, because the results from FE simulation offer as guidance for practical experimental procedures and cross-validate the results for the further development of the whole project. It can conclude that the simulation procedures developed in this work is a good representation of the SAW method procedures of one layer tissue models. Therefore, the simulation can act as a theoretical reference for experiments in SAW method.

Different stimulation methods (high energy laser pulse and mechanical shaker) and detection methods (low coherence interferometry) have been utilized for SAW generation and detection in metal and soft phantom. The results indicate that SAW can be generated and detected from soft materials, i.e. soft agar phantom. This study extends the application of SAW method which was only limited to the properties of hard solids, such as metals, to the soft biological tissues. It has shown that the experimental results are in good agreement with that of the FE simulation result and the theoretical expectations. SAW method may have the potential to apply to determine the elastic properties of skin.

The SAW frequency range of soft solid is much lower than hard solid, which is around 0-10 kHz. Thus, PhS-OCT can be applied to detect the SAW propagates on soft solid, which can take the advantages of PhS-OCT to provide real-time imaging of the samples.

Chapter 5: Signal processing and de-noising in SAW method

5.1 Introduction

This chapter introduces the principles and methods used in processing SAW signals, with the aim of estimating the phase velocity dispersive characteristics from the raw data. From the records of the SAW signals at different positions of receivers, impulsive transient data can be decomposed into their frequency components. Using specific processing algorithms the phase velocity can be calculated as a function of the frequency (Figure 5.1).

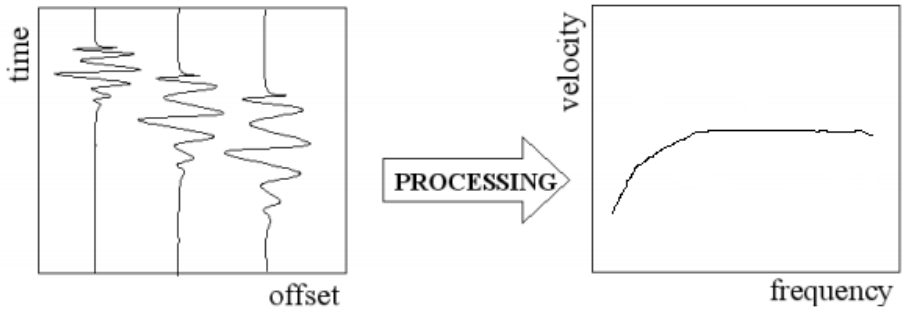

Fig. 5.1 the processing estimates the dispersion curve from raw data

To process the full waveform data recorded from the experimental systems in Chapter 4, two operations i.e., frequency bandwidth and phase velocity as a function of the frequency, are usually needed for the identification of mechanical properties. The phase velocity at each frequency can be obtained by measuring the distances and the travel times. The frequency bandwidth can be determined by spectral analysis.

This chapter introduces the signal processing procedure of the whole project. Firstly, spectral analysis of SAW (SASW) is introduced for SAW phase velocity calculation and frequency bandwidth definition. Due to different nature of SAW stimulation and detection systems, noise is always detected at different frequencies to a recorded signal. Different de-noising methods are discussed and compared in this chapter, including averaging, wavelet de-noising method and empirical mode decomposition (EMD) de-noising method. The phase velocity curve directly reflects the elasticity and geometry information of the sample, thus, inversion procedures which inverse the phase velocity curve to mechanical parameters of model, i.e., the elasticity properties and the thickness of each layer, are also introduced in this chapter.

5.2 Spectral Analysis of SAW (SASW)

In the SAW methods described in this thesis, the acquired SAW data are to be processed in order to estimate the dispersive characteristics. From the records of the impulsive transient SAW data at different positions, the processing algorithms infer the dispersion curve, i.e. the phase velocity as a function of the frequency in a wide frequency range.

Different processing techniques have been used to measure the phase and group velocity from SAW [177-186]. The use of the cross-power spectrum of two-station data has been adopted by many authors who have worked with the spectral analysis of SAW (SASW) approach [179-184]. SASW applies spectral analysis which decomposes a transient signal in its components to obtain a broad band dispersion curve. In SASW, the acquisitions are performed with a group of locations, with equal spacing. The phase difference between any two points is used to compute a phase velocity data of the material. By averaging, the final phase velocity curve can be obtained.

However, the signal frequency analysis has the priority in the whole signal processing procedures, because it shows the available frequency range of the signals. Previously *Wang et al.* [172, 173] indicated that when signals dropped 20 dB below the maximum of autocorrelation spectrum, uncertainty of dispersion curves increased. The frequency range of signals should be defined before analysing phase velocity dispersion curves using this rule.

For example, Fig. 5.2 shows the typical SAW of steel and 2% agar mimicking phantom, and their corresponding frequency range. The typical SAW waveform of single layer steel can be seen in Fig. 5.2 (a). By calculating its autocorrelation spectrum (Fig. 5.2(b)), optimal frequency range can be selected based on the frequency content in the power spectrum. The cut-off frequency of steel is determined at 6 MHz because at this frequency (Fig. 5.2(b)), the power spectrum drops 20 dB below the maximum. With the same rule, the cut-off frequency of 2% agar phantom SAW signal (Fig. 5.2(c)) is chosen at 10 kHz (Fig. 5.2(d)).

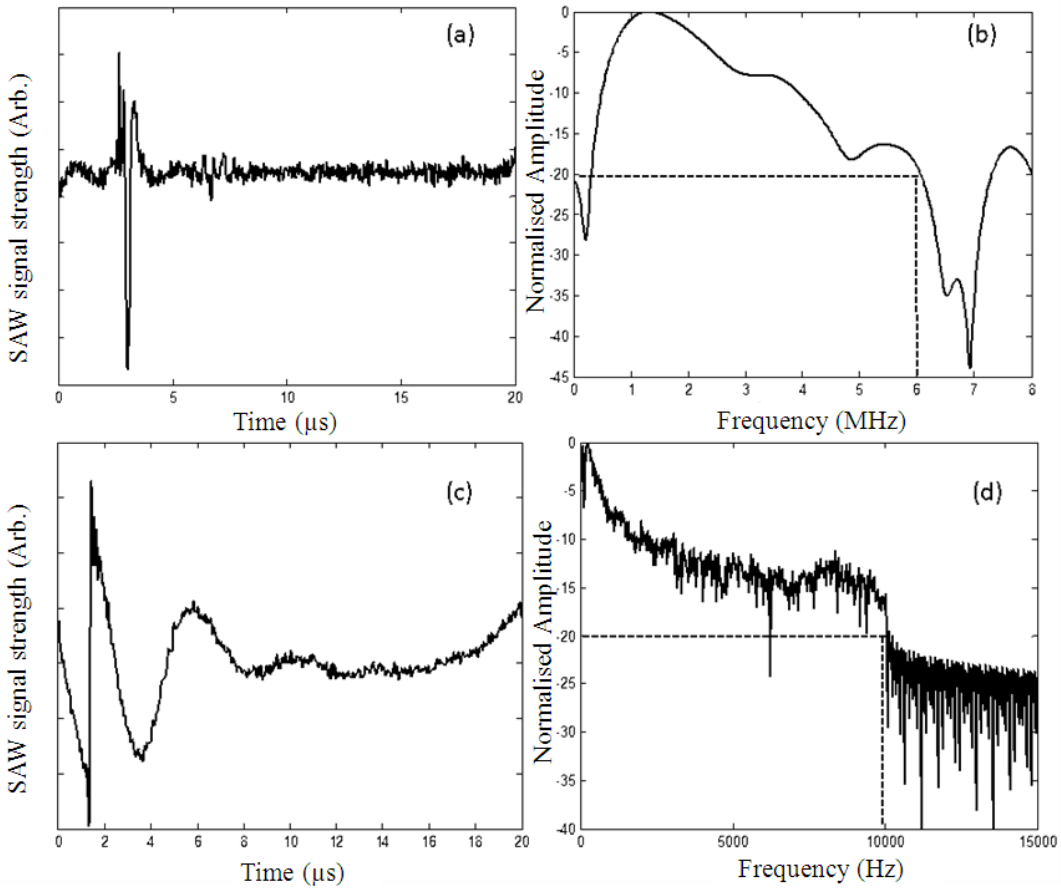

Figure 5.2 SAW waveforms of steel (a) and 2% agar phantom (c) with the corresponded power spectrum (b) and (d)

After the frequency bandwidth definition, the phase velocity calculation can be processed. The phase velocity analysis of any two signals is analysed in frequency domain. For a better understanding, monochromatic sources are used as demonstration first (Fig. 5.3). Two monochromatic signals are detected from location x_1 and x_2. Due to its greater distance from the source, signals are shifted in time. Time shift between two signals corresponds to a phase difference $\Delta\varphi$.

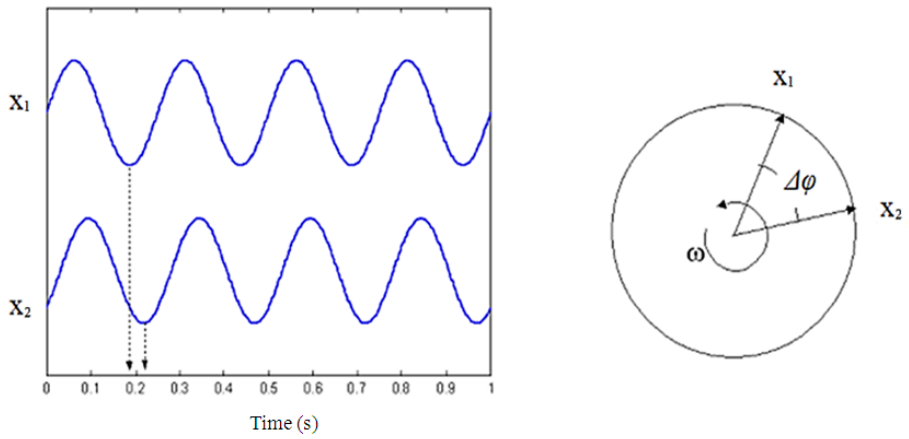

Fig 5.3 (left) Time shift between two monochromatic signals measured in different location: x_1 and x_2, black arrows point the time shift between the two signals (right) the time shift corresponds to a phase difference $\Delta\varphi$ between x_1 and x_2

The phase velocity dispersion curve between two measured signals, $y_1(t)$ and $y_2(t)$ corresponding to locations x_1 and x_2, respectively, were analysed. The phase difference $\Delta\varphi$ between the SAW signals $y_1(t)$ and $y_2(t)$ was calculated by determining the phase of the cross-power spectrum $Y_{12}(f)$. The phase difference can be computed directly from the two complex spectra:

$$y_1 \xrightarrow{F} Y_1(f) = A_1(f)e^{i\varphi_1(f)} \tag{5-1}$$

$$y_2 \xrightarrow{F} Y_2(f) = A_2(f)e^{i\varphi_2(f)} \tag{5-2}$$

and it gives the phase of the cross-power spectrum, $Y_{12}(f)$:

$$Y_{12}(f) = Y_1(f) \cdot \overline{Y_2(f)} = A_1 A_2 e^{i(\varphi_2 - \varphi_1)} \tag{5-3}$$

$$\Delta\varphi = \varphi_2 - \varphi_1 \tag{5-4}$$

where $Y_1(f)$ and $Y_2(f)$ are the Fourier transformations of $y_1(t)$ and $y_2(t)$, A_1 and A_2 are the amplitude of cross-power spectrum and $\Delta\varphi=\varphi_1-\varphi_2$ is the phase difference of the measured signals $y_1(t)$ and $y_2(t)$. Given two receivers at a known distance ΔX, the measured phase difference is 2π when the propagating wave has a wavelength that equals the distance ΔX. More in general, the ratio between the phase difference and 2π equals the ratio between the distance and the wavelength.

$$\Delta\varphi / 2\pi = \Delta X / \lambda \tag{5-5}$$

If the distance between the receivers and the phase difference between the two corresponding signals has been measured, the wavelength can be computed as:

$$\lambda = \Delta X \cdot 2\pi / \Delta\varphi \tag{5-6}$$

The velocity is then obtained, given the frequency f, as:

$$C_R = \lambda \cdot f \tag{5-7}$$

Thus, the velocity can be expressed as:

$$C_R = \Delta X \cdot 2\pi \cdot f / \Delta\varphi \tag{5-8}$$

The velocity is then computed from the phase difference between the signals at the two receivers.

If the wavelength is shorter than the receiver spacing, the phase difference is greater than 2π, and cannot be obtained directly from the analysis of data. All the points at a distance of $N\lambda+\Delta x$ have the same phase difference as shown in (Fig. 5.4). When analysing a certain frequency range, either one has to be sure that the wavelength is greater than the spacing, or the number of entire additional wavelength has to be known.

It can be solved by unwrapping the phase on a wide frequency range (Fig. 5.5). With a single geometrical configuration, if the signal quality is good and the phase difference has a continuous behaviour, the increase of the phase difference with the frequency can be followed up to values greater than 2π. The phase of the cross power spectrum, it can be unwrapped to a full phase representation. Each jump of the phase corresponds to a wavelength. In the unwrapped phase difference, the low frequencies, with greater wavelengths, have a small phase difference, while the high frequencies, with shorter wavelengths, have a great phase difference.

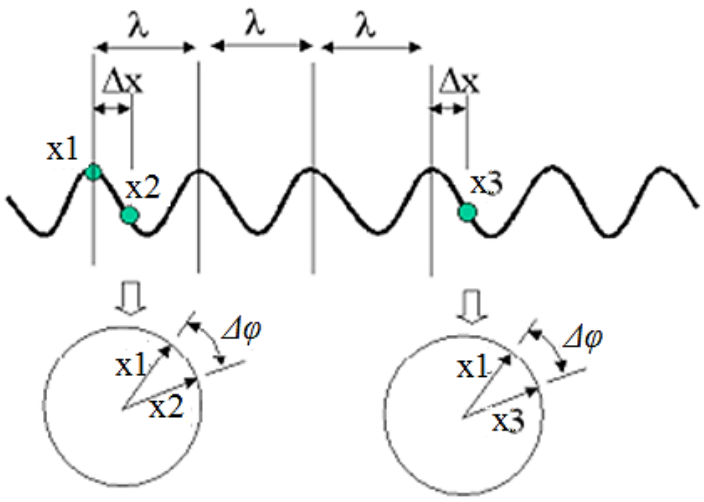

Fig. 5.4 To a single phase difference Δφ, all the points at a distance of Nλ + Δx have the same phase difference. λ is the wavelength of signal .

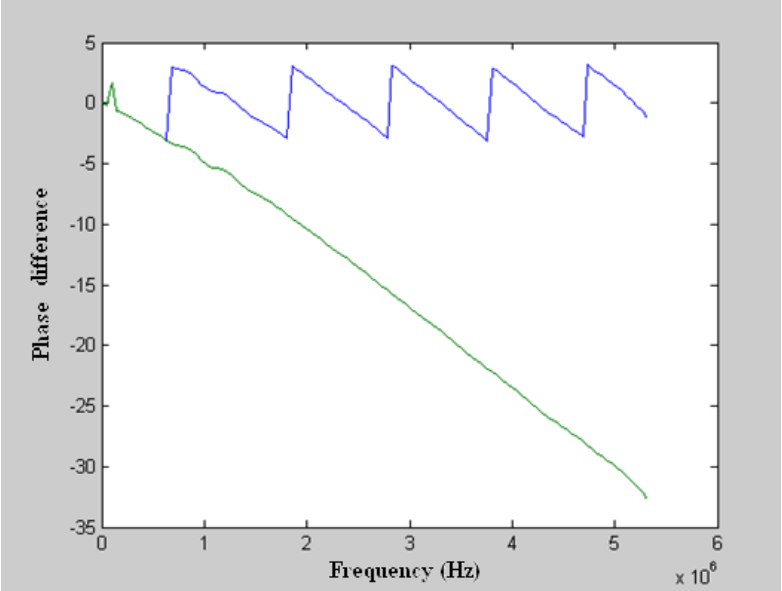

Fig. 5.5 By unwrapping the phase difference (phase of the cross power spectrum) also the wavelengths shorter than the receiver spacing can be identified. Blue: phase difference before unwrapping; Green: phase difference after unwrapping

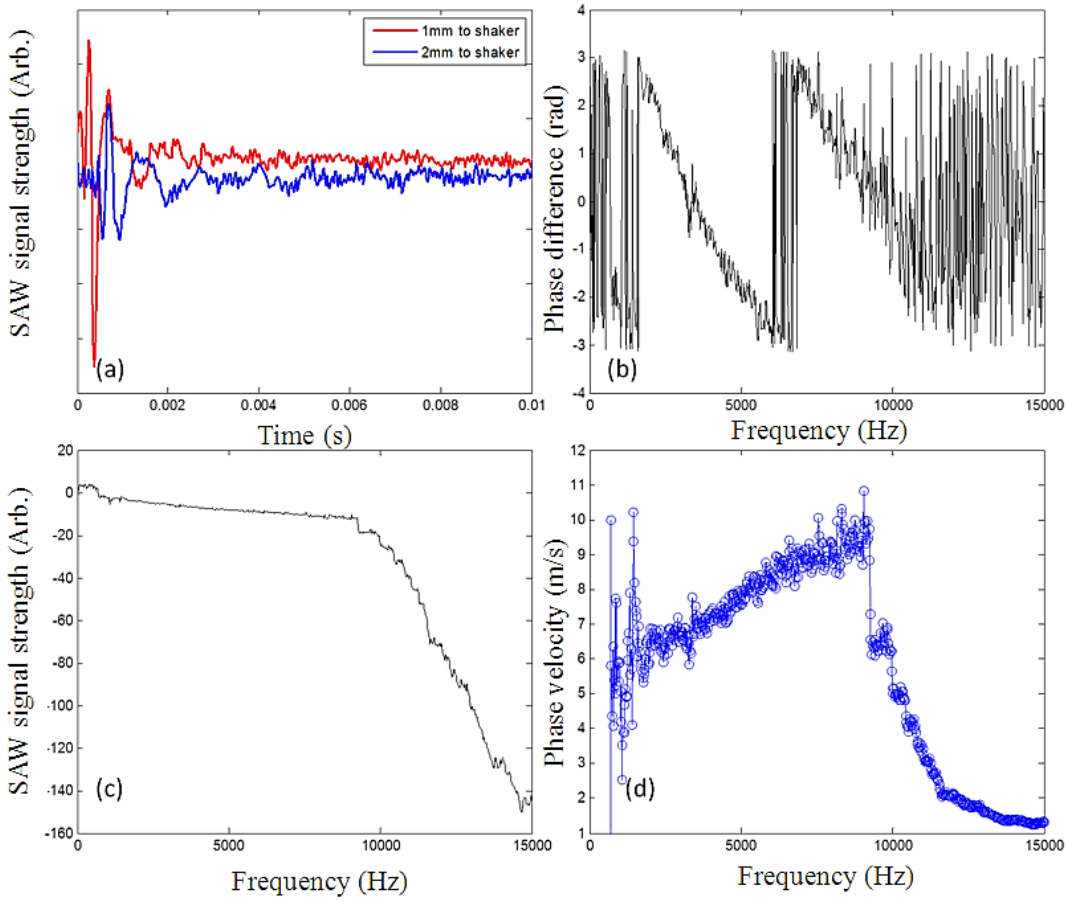

Fig. 5.6 SAW phase velocity calculation procedures from 2% agar mimicking phantom with 1mm and 2mm away to the mechanical shaker source (a); wrapped phase difference (b) is unwrapped to be (c), and the final phase velocity (d) can be calculated.

In the case of transient signals, e.g. SAW, which is generated by impulsive sources, it can be decomposed into their frequency components by means of the Fourier transform. The wave velocity at each frequency can be obtained by the time delay between the two measuring stations. The furthest signal is shifted in time, due to its greater distance from the source. Fig. 5.6 shows the signal processing procedures (Eq. 5-1 to 5-8) with the transient SAW signals from 2% agar phantom. When the frequency exceeds the cut-off frequency which has been set in Fig. 5.2 (d) (10 kHz), strong noise can be observed in wrapped phase difference (Fig. 5.6 (b)). By unwrapping the phase difference, the actual phase difference of each frequency content of the SAW can be obtained in Fig. 5.6 (c),

from which the phase velocity Fig. 5.6 (d) can be calculated. Note that the phase velocity curve is not flat here because of the absence of de-noising procedures.

5.3 De-noising technique of SAW method

Besides experimental errors, noises affect record, including high frequency optical and electric noises in the detecting system (such as the circulator, coupler, and optical balance detector) or due to the complexity of tested materials, coherent noise, random noise, and low frequency seismic noise (any type of vibrations, produced by traffic, human activities, vibrating machines), *etc.* A de-nosing technique is needed to be developed in order to get accurate experiment results.

One signal processing technique for a complex nonlinear and non-stationary signal is the wavelet transformation. Compared with STFT (short time discrete Fourier transform), it is a time-frequency localisation analysis with a changeable analysis window in both time domain and frequency domain, which means around low frequency it has a relative high frequency resolution but relative low time resolution, around high frequency it changes to a high time resolution but low frequency resolution. This character of wavelet analysis is very useful to detect the transient anomalism and display its components. Hence, wavelet analysis has got an incomparable advantage for the de-noising, especially for the non-stationary signals. However, there are also difficulties for wavelet decomposition, such as the choice of mother wave, frequency of overlap and the selection of threshold.

Recently, a new signal processing technique: empirical mode decomposition (EMD) has been developed. The advantage of the EMD is that the base function can be obtained from the signal itself to overcome the difficulty to choose a mother wave in wavelet de-noising method. Therefore, EMD method is used for this study in dealing with non-linear, non-stationary SAW signals.

5.3.1 De-noising by averaging

The majority of noises are random noises. Therefore, a simple but efficient way to reduce random noises is to conduct a large quantity of experiments and then average them. Fig. 5.7 shows the phase velocity dispersion after averaging (red curve) the original data, compared with the unprocessed result (blue curve). From the figure we can find that the

phase noise has been significantly reduced in all the frequency components, especially in low frequency part (1-2 MHz and 4-5.5 MHz). Thus, averaging algorithm has a desirable de-noising effect for some of the low frequency noise. However, it cannot de-noise the high frequency noise (normally noise from the system). Therefore, averaging method will be used and embedded into the other algorithms in the following work, which means before a trial of any algorithm, the signal will be pre-processed by averaging algorithm first to de-noise the low frequency noise.

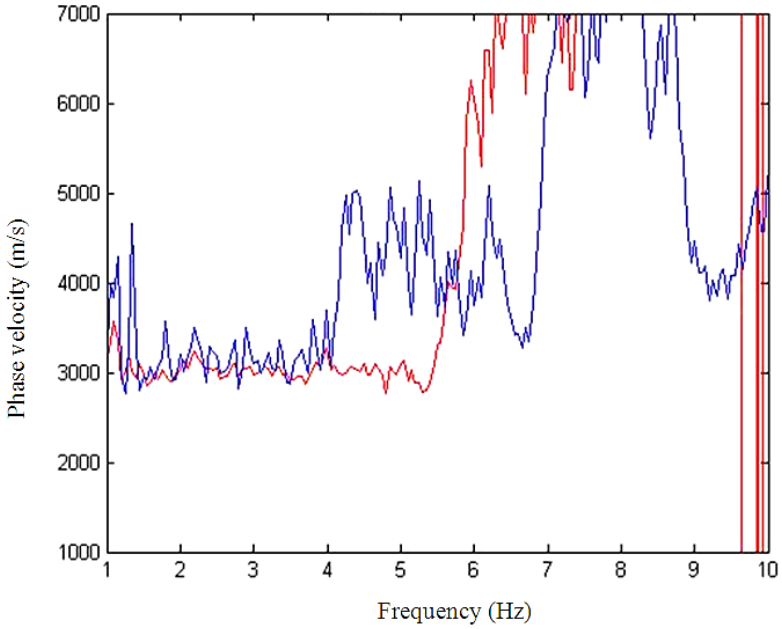

Fig. 5.7 Phase velocity calculated from the un-averaged (blue) and averaged steel data (red).

5.3.2 Wavelet de-noising

A wavelet is a wave-like oscillation with amplitude that starts out at zero, increases, and then decreases back to zero. Wavelet method usually provides an analysis of the signal which is localised in both time and frequency, whereas Fourier transform is localised only in frequency. Given a mother wavelet $\psi(t)$, the continuous wavelet transform (CWT) of a function $x(t)$ is defined as:

$$X(a,b) = \frac{1}{\sqrt{a}} \int_{-\infty}^{\infty} \psi \left(\frac{t-b}{a}\right) x(t) dt \tag{5-9}$$

The scale or dilation parameters correspond to frequency information (a - frequency^{-1}), and the translation parameter b relates to the location of the wavelet function as it is shifted through the signal. The integral in Eq. 5-9 can be seen as a convolution operation of the signal and a basis function $\psi(t)$. It should be emphasised that, unlike Fourier transform in which the basis function is $e^{i\omega t}$, there are many possible choices for the mother wavelet $\psi(t)$.

In practice, the transform used is the discrete wavelet transform (DWT) which transforms digital signals to discrete coefficients in the wavelet domain. This transform is essentially a sampled version of CWT. The values of $X(a, b)$ are calculated over a discrete grid:

$$a = 2^{-j}, b = k \cdot 2^{-j}, \qquad j, k \epsilon \mathbb{Z} \tag{5-10}$$

In the case of DWT, assuming that the length of the signal satisfies $N=2^J$ for some positive J, the transform can be computed efficiently. This results in a decomposition of the signal into different scales which can be considered as different frequency bands. At each decomposition level, the filters produce signals spanning only half the frequency band. This doubles the frequency resolution as the uncertainty in frequency is reduced by half. Thus, the output of each filter can be decimated by a factor of 2 in accordance with Nyquist's theorem. Using this approach, the time resolution becomes good at high frequencies, while the frequency resolution becomes good at low frequencies. The range of decomposition levels should be determined according to the features of the signal to be analysed. A typical number is 3-5. Each coefficient will be compared with a threshold in order to decide whether it constitutes a desirable part of the original signal or not. Thus, the chosen three factors need to be determined for a wavelet analysis: the mother wave, decomposition level and threshold. Different permutation and combination lead to different results. Fig. 5.8 show typical flow charts of wavelet de-noising method. Firstly a mother wavelet will be chosen from collections (Harr, dbN, *etc.*). Then decomposition level and threshold will be selected. Large quantities of trials have been conducted. Using db1 (Haar) mother wavelet with a decomposition level of 4 and 'heursure' soft threshold has the best phase de-noising results, for both hard and soft materials.

Mother wavelet	Haar	dbN	biorNr, Nd	coifN	symN	morl	mexh	meyr
Decomposition level	3	4	.....	N-1	N			
Threshold selection	Forcibly de-noising	Soft threshold 'rigrsure' 'sqtwolog' 'heursure' 'minimaxi'		Hard threshold				

Fig. 5.8 Typical flow chart of wavelet de-noise

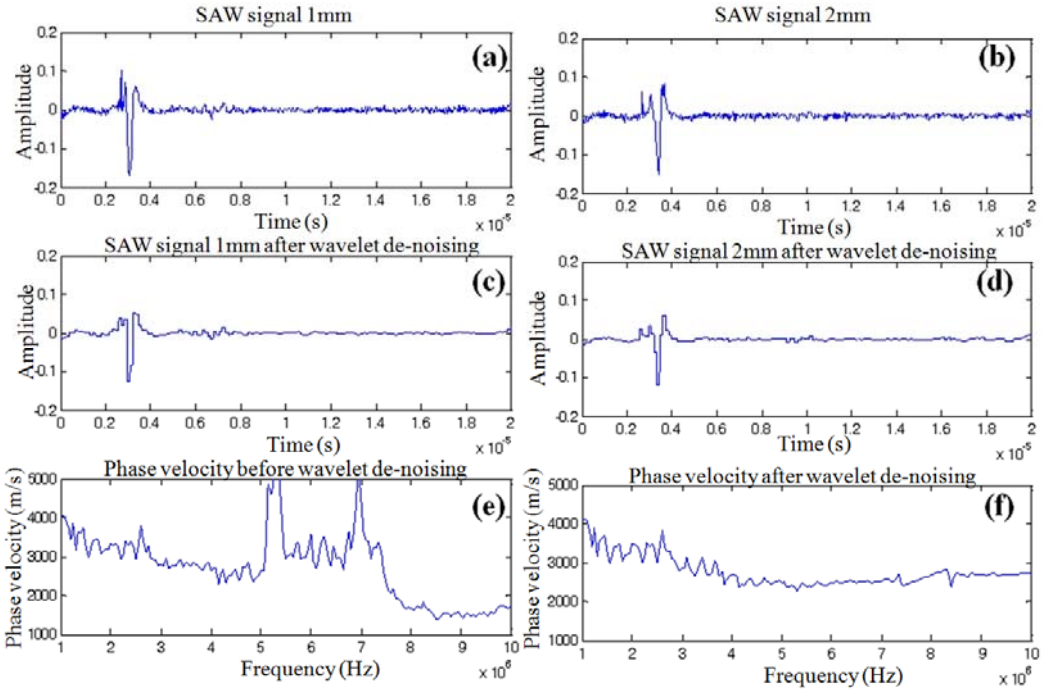

Fig. 5.9 Wavelet de-noising for steel, (a) and (b) Averaged SAW signal of steel from position in 1mm and 2mm; (c) and (d) Wavelet de-noised SAW in 1mm and 2mm; (e) and (f) Calculated phase velocity curve from average and wavelet de-noising method

Fig. 5.9 shows the comparison of both average (a and b) and wavelet (c and d) de-noising method for SAW signal of steel material. The calculated phase velocity curves from both of the de-noising methods are also compared in e and f. Noise in high frequency

content (5MHz-7MHz) is significantly reduced, which can be found from both waveform and phase velocity curve. Wavelet de-noise method is applicable for de-noising the SAW of hard solids (for the frequency range up to several megahertz). However, signal distortion can be observed, especially in peaks and turns of the signals, which will lead to the fault results in high frequency range.

Fig. 5.10 shows the comparison of both average (a and b) and wavelet (c and d) de-noising method for SAW signal of 3.5% agar phantom. Same with steel, high frequency component can be de-noised. But as the phantom is homogeneous material, the phase velocity curve should be a constant value but not gradually increasing. Because both of the average and wavelet de-noise cannot easily filter the low frequency noise (which comes from the detecting noise from the system), the accuracy of phase velocity calculation is greatly affected.

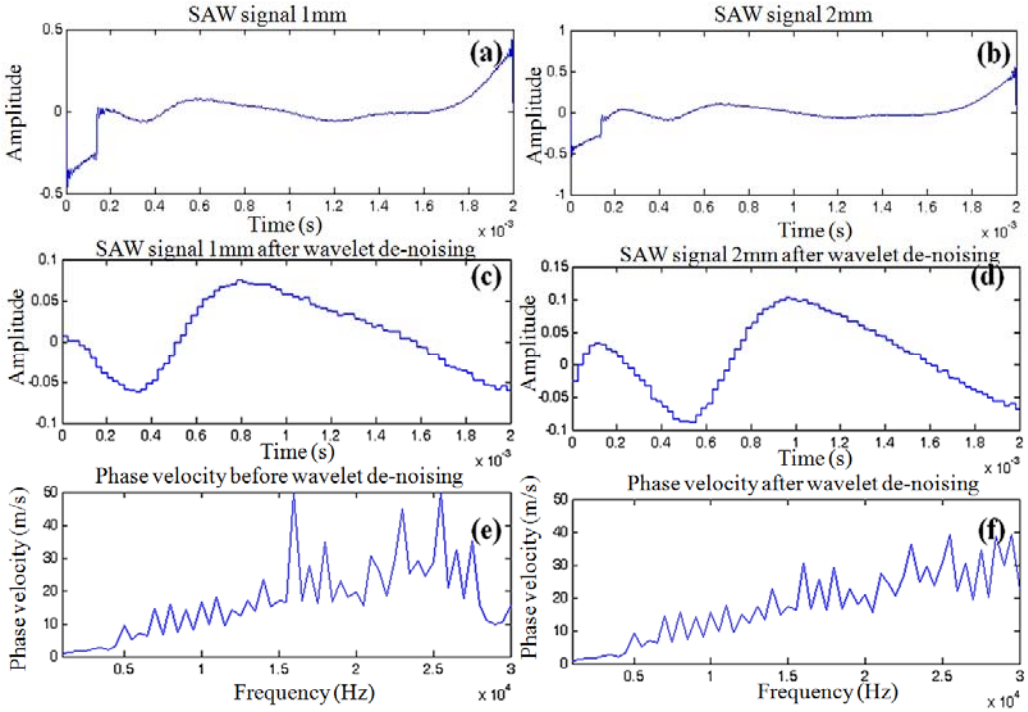

Fig. 5.10 Wavelet de-noising for 3.5% agar phantom, (a) and (b) Averaged SAW signal of 3.5% agar phantom from position in 1mm and 2mm; (c) and (d) Wavelet de-noised SAW in 1mm and 2mm; (e) and (f) Calculated phase velocity curve from average and wavelet de-noising method

In conclusion, although wavelet de-noising method is relatively developed, it has some limitations. Firstly, it is not self-adjustable. Different mother wavelet, decomposition level and threshold have to be defined before the de-noising procedure. Strong signal distortion may occur. In addition, instead of removing electrical noise, it only deals with an additive noise.

5.3.3 Empirical mode decomposition (EMD) de-noising

The Hilbert-Huang transform (HHT) uses the empirical mode decomposition (EMD) method to decompose a signal into so-called intrinsic mode function. The HHT provides a new method of analysing non-stationary and nonlinear time series data. Using the EMD method, any complicated data set can be decomposed into a finite and often small number of components, which is a collection of intrinsic mode functions (IMF). An IMF represents a generally simple oscillatory mode as a counterpart to the simple harmonic function. By definition, an IMF is any function with the same number of extreme and zero crossings, with its envelopes being symmetric with respect to zero. The definition of an IMF guarantees a well-behaved Hilbert transform of the IMF. This decomposition method operating in the time domain is adaptive and highly efficient. Since the decomposition is based on the local characteristic time scale of the data, it can be applied to nonlinear and non-stationary processes. In order to realise that, the first stage is to calculate and compute the IMF's of the signal. The EMD process itself can be done in several steps:

- Find the location of all maxima $x_{max}(t)$, and minima $x_{min}(t)$ of signal $x(t)$.
- Connect all $x_{max}(t)$ pointe with cubic spline (upper envelope) and do the same procedure to $x_{min}(t)$ to produce lower envelope.
- Compute the mean of spline curves at each point:

  $$m(t) = \frac{X_{\max}(t) + X_{\min}(t)}{2}$$

- Remove the trend, $m(t)$. Let $d(t) = x(t) - m(t)$.
- Now if $d(t)$ is an IMF according the definition of IMF, let $c_i(t) = d(t)$ and advance i by 1. Find the residual $r(t) = x(t) - d(t)$. If $d(t)$ is not an IMF (according to definition of IMF), further sifting is needed.

- Repeat steps 1 to 5 (x(t)←d(t)). The sifting process can be stopped when *r(t)* becomes a monotonic function and no more IMF can be extracted.

When all the steps have been processed, now it has several IMFs (represented by c_i):

$$r_1=x(t)-c_1$$

$$r_2=r_1-c_2$$

.

.

.

Then,

$$x(t)=\sum_{i=1}^{n} c_i + r_n$$

These IMFs have different scales, representing high frequency (small scales) and low frequency (large scales). Hence signal can be denoised via the reconstruction with several selected frequency IMFs as follows,

$$\tilde{y}(t)=\sum_{j=k}^{n} IMF_j\,(t)+r_n(t) \quad (k=2,\dots,n) \tag{5-13}$$

Then the problem is where is the threshold to choose the first IMF for the reconstruction. Some papers recommend using the continuous mean square error principle, which can be showed with the expression as:

$$CMSE(\tilde{y}_k,\tilde{y}_{k+1})=\frac{1}{N}\sum_{i=1}^{N}[\tilde{y}_k(t_i)-\tilde{y}_{k+1}(t_i)]^2 \tag{5-14}$$

$$=\frac{1}{N}\sum_{i=1}^{N}[IMF_k(t_i)]^2\,,(k=1,\dots,n-1)$$

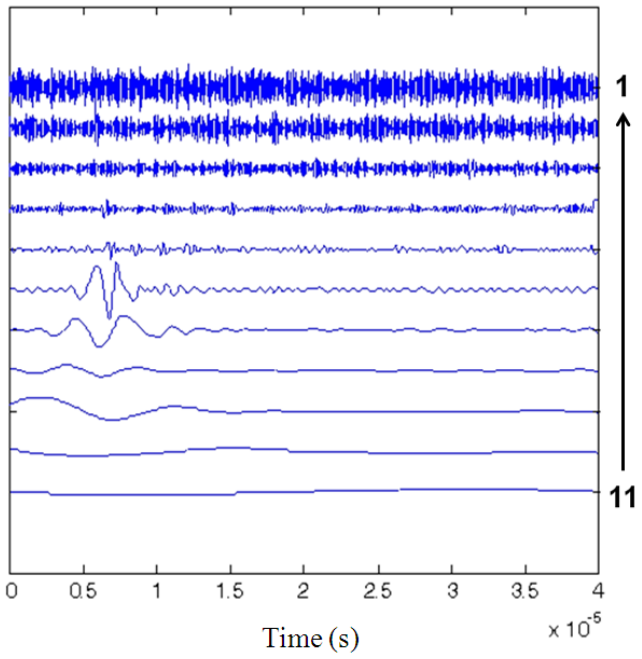

Fig. 5.11 IMFs from HHT transform of a steel SAW signal

Take a steel SAW signal for example. After the HHT transform the signal can be decomposed into 11 IMFs (Fig. 5.11), the first IMF domain the highest frequency component, and the 11th IMF domain the lowest frequency component. However, each IMF has a frequency overlap. For de-noising, it simply adds the frequency components that contain the information of SAW signal together and avoid the IMF which normally contains noise (in high and low frequency components which correspond to the first and last IMFs).

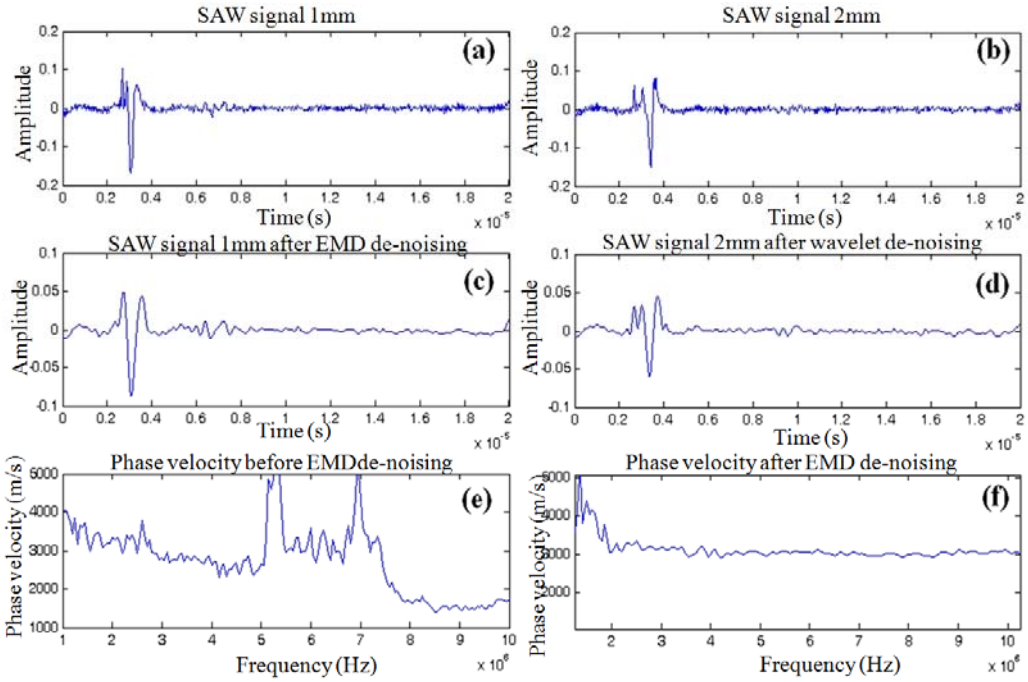

Fig. 5.12 EMD de-noising for steel, (a) and (b) Averaged SAW signal of steel from position in 1mm and 2mm; (c) and (d) EMD de-noised SAW signal of steel from position in 1mm and 2mm; (e) and (f) Calculated phase velocity curve of averaged SAW and EMD de-noised SAW

Fig. 5.12 shows the comparison of both average (a and b) and EMD (c and d) de-noising method for SAW signal of steel material. The calculated phase velocity curves from both of the de-noising method are compared in e and f. High frequency noise of the SAW signal is well removed, which can be observed from both of the SAW signal and phase velocity curve after the EMD filter being processed. No strong signal distortion happens. Fig. 5.13 shows the comparison of both average (a and b) and EMD (c and d) de-noising method for SAW signal of 3.5% agar phantom. Different from wavelet de-noising method, the low frequency noises can be easily removed (by deleting the low frequency IMF from the SAW signal). Thus, the phase velocity shows as a constant value which fit the material characterisation.

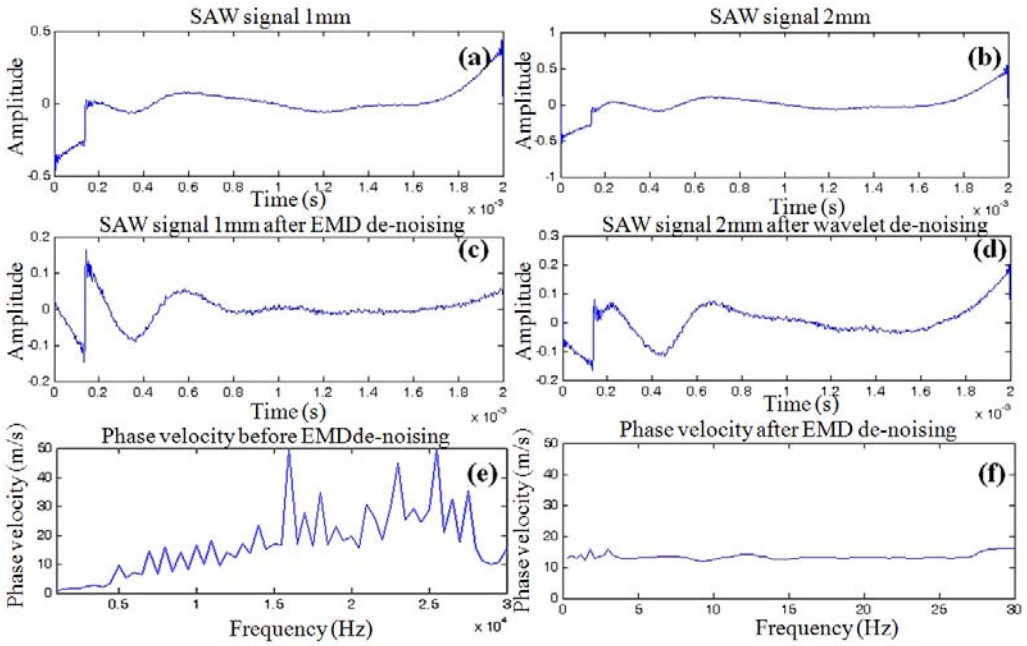

Fig. 5.13 EMD de-noising for 3.5% agar phantom, (a) and (b) Averaged SAW signal of 3.5% agar phantom from position in 1mm and 2mm; (c) and (d) EMD de-noised SAW signal of 3.5% agar phantom from position in 1mm and 2mm; (e) and (f) Calculated phase velocity curve of averaged SAW and EMD de-noised SAW

In conclusion, the EMD de-noising method is a very powerful tool to process signals and the HHT Algorithm can easily be implemented in any programming languages. It is self-adjustable to the signal. However the mathematical foundation of EMD de-noising method is not complete but it can still be used in many applications. In this study, EMD de-noising is utilised as the main de-noising method.

5.4 Inversion

The inversion is the final procedure in processing of the SAW method, and produces the final result of elasticity data. It consists of estimating the parameters of a layered model from the dispersion curve measured at a site. The inversion transforms the properties of the SAW propagation into the properties of a material layered model. The SAW method inverse problem is non-linear, and often mix-determined, which consists of estimating the model parameters when the SAW phase velocities have been measured.

As mentioned in the previous chapters, the propagation of SAW in layered materials shows a dispersive behaviour, where the different frequency components have different phase velocities. The phase velocity at each frequency is dependent on the elastic and geometric properties of the materials at different depths. In isotropic homogeneous materials, the SAW phase velocity can be approximated as [170, 171, 174]:

$$C_R = \frac{0.87+1.12\upsilon}{1+\upsilon}\left(\frac{E}{2\rho(1+\upsilon)}\right)^{\frac{1}{2}} \tag{5-15}$$

where E is the Young's Modulus, υ is the Poisson's Ratio, and ρ is the density of the material. Thus, once the phase velocity is known, the Young's modulus of the material can be estimated by:

$$E = \left(\frac{C_R(1+\upsilon)}{0.87+1.12\upsilon}\right)^2 2\rho(1+\upsilon) \tag{5-16}$$

For a multilayer medium, in which each layer has different elastic properties, the phase velocity of the SAW is influenced by the mechanical properties of all the layers it penetrates into. The elastic properties that affect the phase velocity dispersion curve include not only the Young's modulus, Poisson's ratio and density of each layer, but also the thickness of each layer. In this case, the SAW with shorter wavelengths (higher frequency) penetrates the shallow depth with the phase velocity depending on the superficial layers. On the other hand, the SAW with longer wavelengths (lower frequency) penetrates deeper in the material and the phase velocity tends to be mostly influenced by the elastic properties of the deeper layers. A property of SAW is that the depth of the wave motion is proportional to the wavelength. The probing depth (z) can be estimated by the following relation [155, 170, 171, 174]:

$$z \approx \lambda = \frac{C_R}{f} \tag{5-17}$$

where f is the corresponding frequency content. The relations between probing depth and frequency are not linear, the problem is hence a non-linear inversion. The set of model parameters described above completely represents the layered models. The velocities can be in general complex, thus allowing accounting for material attenuation and viscoelastic behaviour. All these parameters have to be specified to solve the forward problem, however, the solution is more sensitive to some of them, in particular the velocity and the

layer thickness. Therefore in the inversion, mass density (ρ) and Poisson ratio (υ) are often assumed a priori on the basis of other approaches.

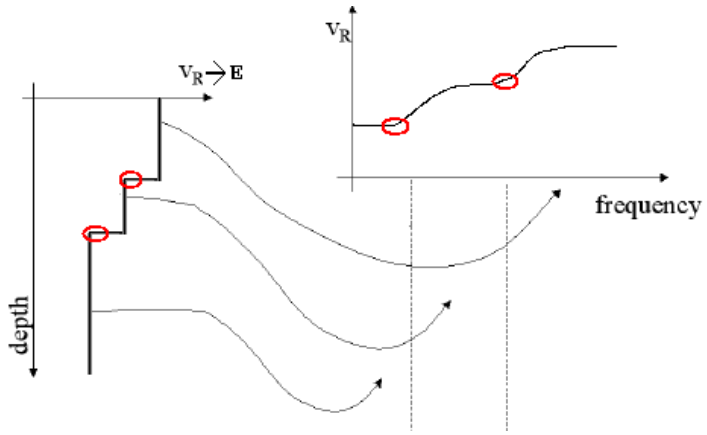

Fig. 5.14 Scheme of the relations between the model space (left) and the data space (right), red circles indicated the elasticity changes of the material, black arrows indicate the corresponding model space of data space.

The inversion procedure can be illustrated in Fig. 5.14. From the spectral analysis and the de-noising procedure mentioned above, the phase velocity of a group of SAW signals can be obtained. If the material is a homogeneous material, the phase velocity of all frequency components should be equal. On the contrary, if the material is layered, the phase velocity is no longer constant, but changing with the frequency (right, Fig. 5.14). High frequency part of phase velocity represents the information of shallow depth in material, with the frequency decreased, the phase velocity represents deeper of the material model. Each turning point (marked with red cycles in Fig. 5.14) indicates the elasticity change in axial direction, i.e. the appearance of a layer with higher or lower elasticity. By determining the frequency of the turning points, thickness of each layer of material model can be calculated by Eq. 5-17. The elasticity of that layer can be estimated by Eq. 5-16 by the phase velocity value and known density and Poisson's ratio. Thus, the material geometry can be recovered and built, as showed in left figure in Fig. 5.14.

5.5 Conclusion

Presented in this chapter is the signal processing procedures. SAW method converts the time domain SAW into the frequency domain phase velocity, different frequency

components of the waves can be analysed. Different kinds of signal de-noising methods for the transient SAW signal: averaging, wavelet de-noising method and EMD de-noising method have been introduced and compared. EMD method has clearer advantages than wavelet method. Thus, it will be utilised in the following chapters for signal de-noising.

The use of SAW method is an extremely sensitive technique for the characterisation of layered materials with the phase velocity dispersion curved dependent on the SAW velocities of each layer in the material. The shape of this curve in a homogenous isotropic material will remain of constant value as no dispersion will occur. In layered materials the curve will either increase or decrease depending on the properties of the materials. From the phase velocity curve, quantitative elasticity of different layers in a material model can be estimated in inversion procedure.

In the following chapters the mathematical procedures developed here will be used to analyse the SAW that are generated in the different models to study the sensitivity of the SAW method to changes in the mechanical and geometrical properties.

Chapter 6: The behaviour of SAW in homogeneous materials and heterogeneous soft solids

6.1 Introduction

This chapter discusses the behaviour of SAW in different homogeneous materials and heterogeneous soft solid samples, including hard solids (metal and plastic) and soft solid agar tissue mimicking phantoms with different layer thickness and different elasticity in both transverse and axial directions.

Homogeneous materials were tested including hard and soft solids. Q-switched high energy laser pulse source and low coherence interferometry system were utilised for SAW detection first. This combination provides broadband generation and detection which enables the full SAW determination in frequency, in order to reveal the relationship of SAW frequency range and material stiffness. After successfully study the SAW's behaviour in soft solids, PhS-OCT detection and mechanical shaker generation were proven to have enough frequency bandwidth for the application of SAW in soft solids, especially skin.

Then a group of layered agar mimicking phantom are made. Phantoms are designed to change the elasticity in both axial and transverse directions. Firstly, a two-layer phantom is made with a known surface layer thickness to investigate the ability of layered characterisation thickness and elasticity measurement using SAW phase velocity dispersion. Then, a two-block phantom with different elasticity from each side is fabricated to test if SAW method is sensitive to the transverse elasticity change. Finally, both of the axial and transverse elasticity changes are combined together, to mimick the skin diseases. The Young's modulus of each phantom and its geometry conditions are estimated from the SAW velocity measurement and then compared with those measured from the literature to calibrate and assess the accuracy of SAW mechanical characterisation.

6.2 Development of SAW method in homogeneous medium

In the study, homogeneous hard solids were tested first, in order to cross-validate the SAW method used in this project with literatures. As mentioned in chapter 4, high energy laser pulse source and low coherence interferometry system (Fig. 6.1) are used to generate and detect the SAW. The specimen of mild steel, cast iron and Perspex plastic plates are utilised in the experiment. The system stimulates and detects a full frequency range of

SAW in different materials so the system can detect a full spectrum of SAW behaviours. All the specimen plates have a thickness of 50mm-100mm.

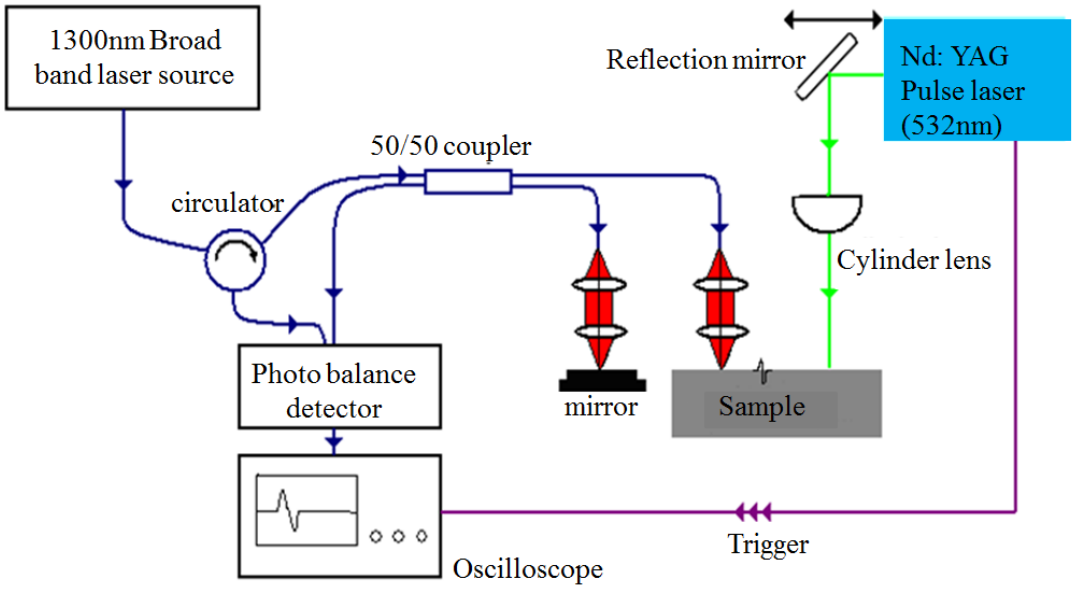

Figure 6.1 System set up of high energy laser pulse generation and low coherence interferometry detection of SAW

Fig. 6.2 (a, c and e) shows the typical SAW recorded from steel, iron and black Perspex, respectively. The excitation laser beam is first located at a position 1 mm away from the detecting point (bottom), and then moved at 1 mm/step to 6 mm away (top). As shown in the figure, it is clear that the SAW is propagating away from the laser-excitation position. In addition, attenuations between the waveforms are clearly observed.

Fig. 6.2 (b, d and f) shows the normalised power spectrum of all six SAW signals of steel, iron and Perspex corresponding to the left column. Optimal cut-off frequency is selected based on the frequency content in the power spectrum. In this case, the cut-off frequency is chosen at 5.5 MHz in the case of steel plate because at this frequency, the power spectrum drops 20 dB below the maximum. Base on the same rule that the maximum frequency content of a SAW signal in iron plate can be obtained, which is approximately 3.5 MHz and that in iron is approximately 2.0 MHz Perspex.

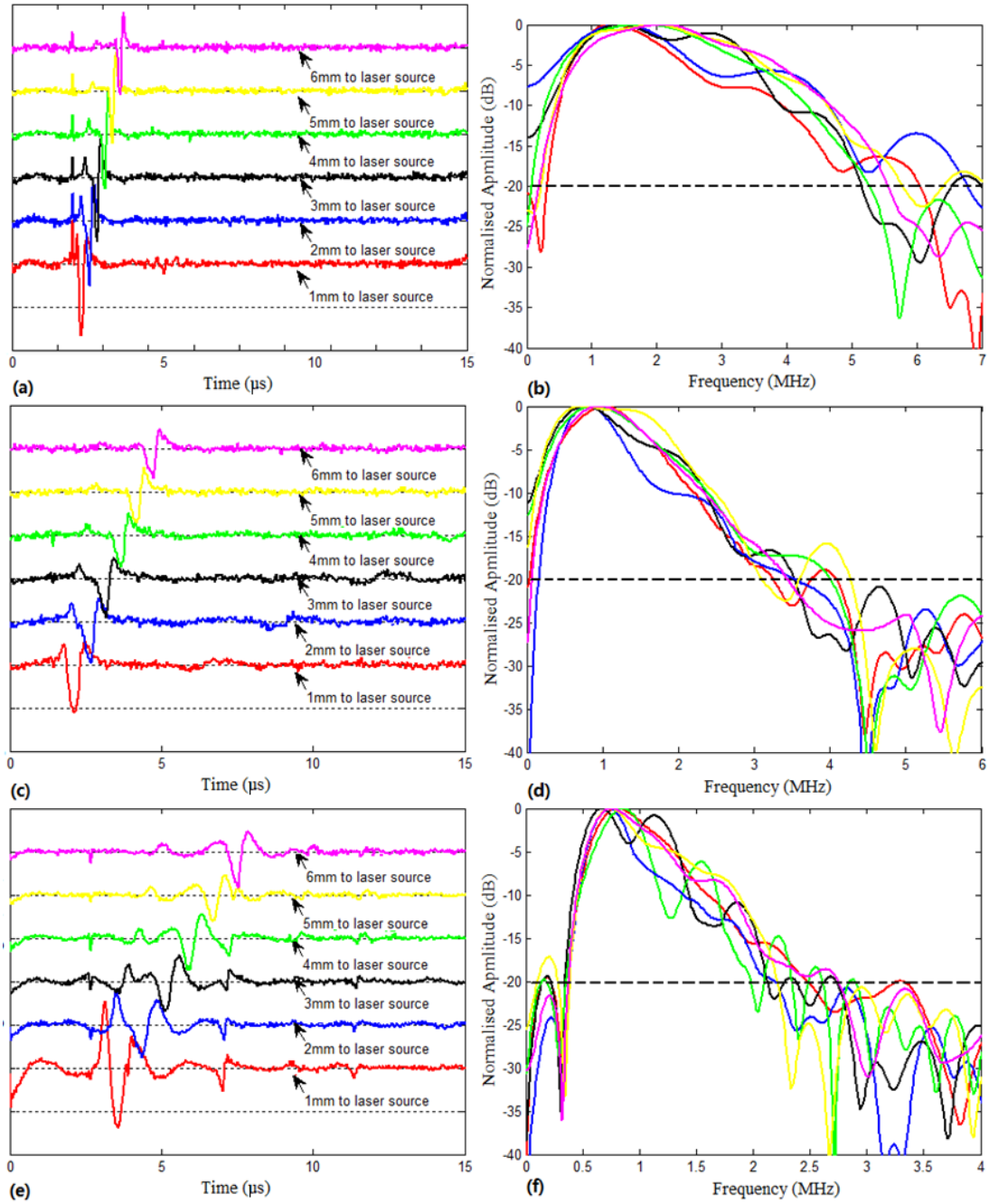

Fig. 6.2 Left column shows SAW signal of steel plate (a), iron (c) and Perspex (e) with the distance of 1 mm (bottom) to 6 mm (top) to laser pulse, with 1mm/step. Right column shows power spectrum in the detected SAW of steel plate (b), iron (d) and Perspex (f)

Experiments are also performed the tissue mimicking phantoms made of 3.5% solidified agar solution. All the phantoms are homogeneous, with a minimum thickness of 50mm to ensure the treatment of measurements under the semi-infinite conditions is valid, where a semi-infinite condition means SAW travels in unbounded

solid. Fig. 6.3 left shows the typical SAW recorded from one layer 3.5% agar phantom. The excitation laser beam is first located at a position of 0.5 mm away from the detecting point (bottom), and then moves in 0.5 mm/step to 3 mm away (top). Compared with the laser-induced SAW in the hard materials shown in Fig. 6.2 (a, c and e), the SAW in the soft materials have a longer wavelength and travel at a slower velocity. In addition, a clear attenuation between the waveforms can be observed. The spikes observed in every signal at the time 0.08 ms is a high frequency thermal expansion when laser pulse is given. Fig. 6.3 right shows the power spectrum of all six SAW signals. The cut-off frequency is at 20 kHz.

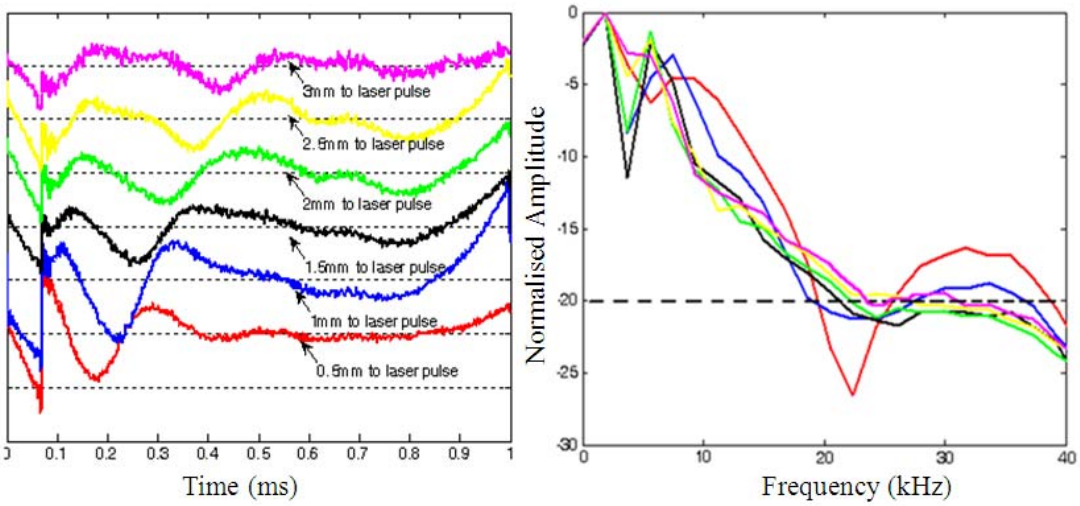

Fig. 6.3 (Left) SAW signal of one layer 3.5% agar phantom with the distance of 0.5 mm (top) to 3 mm (bottom) to laser pulse, with 0.5 mm/step. (Right) Power spectrum of the detected SAW of one layer 3.5% agar phantom

Fig. 6.4 and Fig. 6.5 indicate the phase velocity dispersion curves of the SAW in solid specimens and agar phantoms. The phase velocity remains at a steady level in homogeneous specimens as expected. Table 6.1 shows the relationship between Young's modulus and maximum SAW frequency of steel, iron, Perspex and 3.5% agar phantom from experiment respectively.

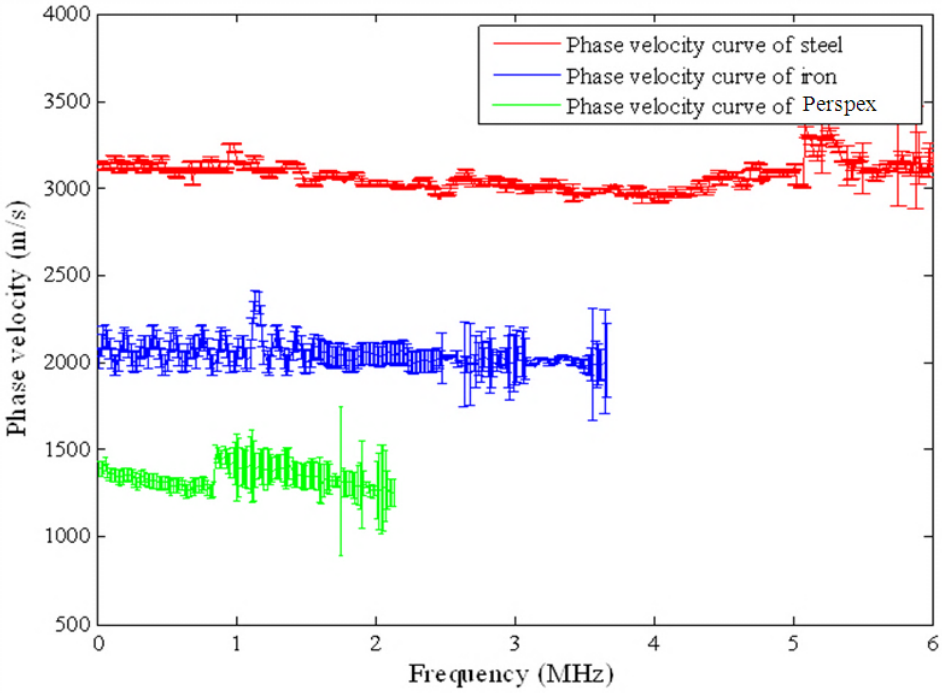

Fig. 6.4 Phase velocity dispersion curve of steel, iron and Perspex

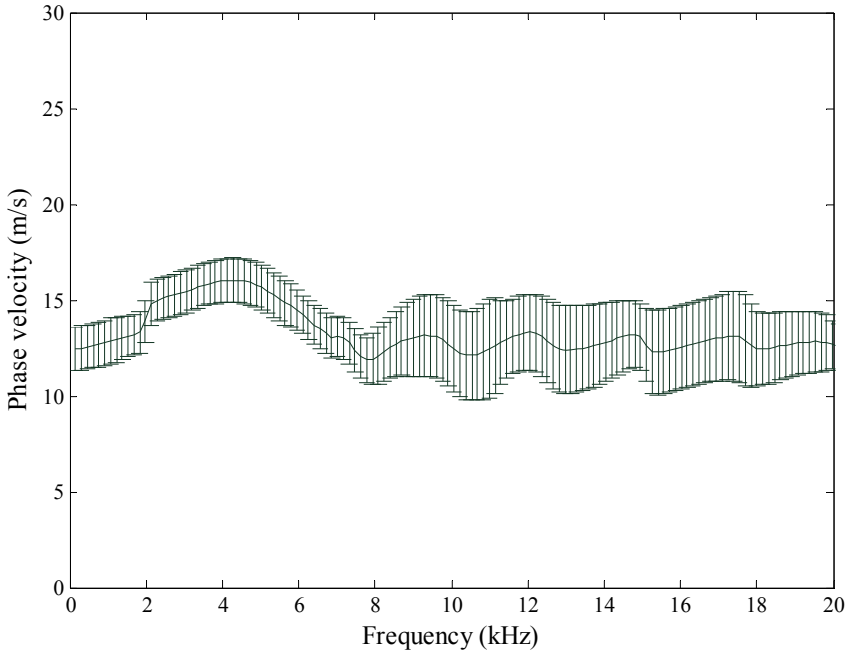

Fig. 6.5 Phase velocity dispersion curve of 3.5% agar phantom

Using Eq. 5-16, the Young's moduli are evaluated by the mean phase velocity in each material phase velocity dispersion curves measured from 6.2 (a, c and e) in Fig. 6.3, the results are matched with literature [16, 17, 187-189]. Note that the Poisson's ratio and density of different materials are assumed from literature. From the table, as

expected, with the decreasing of Young's modulus, the maximum SAW frequency reduces. In addition, the maximum of frequency content of SAW signal increases monotonically with the increase of the phase velocity of each sample, as expected. Thus, maximum of frequency content of SAW signal increases with the root of estimated Young's modulus. Combining Eq. 3-19 with Eq. 3-21, the maximum SAW frequency can be described by:

$$f_{max} = \frac{2.46+3.16\upsilon}{(1+\upsilon)\pi r_0}\left(\frac{E}{2\rho(1+\upsilon)}\right)^{\frac{1}{2}} \quad (6\text{-}1)$$

where r_0 as 0.5 mm is employed (equal to half of the line source width). The theoretical value can be calculated from Eq. 3-21 that the expected maximum frequency contents of steel, iron, Perspex and 3.5% agar phantom are 5.6 MHz, 3.6 MHz, 2.2 MHz and 23 kHz respectively. Our experimental results agreed with the expectations. Eq. 6-1 could be employed to evaluate the maximum SAW frequency content, given the sample properties and generation setup.

Table 6.1 Relationship between Young's modulus and Maximum SAW frequency

Material	**Material property**		**Experimental Data**		**Max. SAW frequency**	
	Poisson's ratio	Density (g/cm^3)	Phase velocity (m/s)	Young's modulus	Experiment	Theoretical
Steel	0.29	7.9	3005.54±137.95	217.45± 0.46GPa	5.5 MHz	5.6 MHz
Iron	0.27	7.2	2040.76±157.31	87.38± 0.53GPa	3.5 MHz	3.6 MHz
Perspex	0.39	1.18	1350±170.87	5.45±0.69GPa	2.0 MHz	2.2 MHz
3.5% agar phantom	0.495	1.05	13±1.25	592 ±5.39kPa	20 kHz	23 kHz

The above experiments show the relationship between material elasticity, the radius of stimulator and the maximum frequency range that are generated. The above experimental data show that the frequency range of soft material is in kHz range (0-30kHz), which is relatively low. It is able to transfer the detecting system to PhS-OCT imaging system (the sample frequency is 47 kHz) and the real time imaging of sample while detecting the SAW can be achieved. In addition, for further skin experiments,

the high energy Q-switched laser pulse source will be replaced by the mechanical shaker to avoid the laser safety problem.

Three single layer agar phantoms were prepared, to simulate soft tissues. A higher agar concentration produces stiffer gels with higher Young's modulus. Homogenous single layer phantoms were prepared with agar concentrations of 1%, 2% and 3% and their phase velocities were determined. The single layer phantom and the bottom layer of the double layer phantom had a thickness of 10 mm, which was considered semi-infinite for this application and should not affect the results. To improve the scattering coefficient of the tissue-mimicking phantoms, several drops of milk were mixed with the agar solution. It is because OCT mainly measures the scattering light from sample.

Fig. 6.6 shows the typical SAW recorded from a single layer 2% phantom. The PhS-OCT sample beam was located at 1, 2, 3, 4, 5 and 6mm away from the shaker head. Fig. 6.6 demonstrates that the SAW is moving away from the shaker-excitation position because the arrival time of the SAW is delayed as the detector is located farther away (diagonal line in Fig. 6.6). Since the sample was a single-layer homogeneous phantom, no velocity-dispersion was found in the detected waveforms. However, the waveform was attenuated with an increasing distance from the shaker. Although there were two SAW detected at each position in the experiment, since the shaker applies two pulses per experiment, the first SAW will be presented only. Similar results were obtained from the second SAW.

The average phase velocity dispersion curves of all single-layer phantoms are plotted in Fig. 6.7. All the curves exhibit a constant value for all frequencies, as expected from a single-layer homogeneous sample. The average phase velocities measured from the curves were 12.33±1.03 m/s, 7.55±1.09 m/s and 4.87±0.94 m/s which yielded a Young's modulus of 515±3.59 kPa, 193 kPa±4.01 and 0±2.99 kPa for the 3%, 2% and 1% phantoms, respectively. The Young's modulus was calculated with Eq. 5-15 by using a Poisson's ratio of 0.47 and a density of 1,040kgm^{-3} [170, 171]. As expected, the higher concentration of agar exhibits higher phase velocity due to its higher Young's modulus.

In addition, the maximum frequency content of the shaker-generated SAW was increased with the increase of agar concentration. The cut-off frequency was selected when the intensity of the power spectrum dropped 20 dB below its maximum. The maximum frequency content for the 1%, 2% and 3% phantoms was 4 kHz, 5.5 kHz and 8.3 kHz, respectively. These values were lower than the theoretical maximum

frequency content calculated from Eq. 6-1 (4.37 kHz, 6.5 kHz and 9.5 kHz for the 1%, 2% and 3%, respectively with the stimulator radius of 1 mm of the mechanical shaker head mentioned in Chapter 4), because the maximum frequency content might exceed the -20 dB cut-off of the power spectrum.

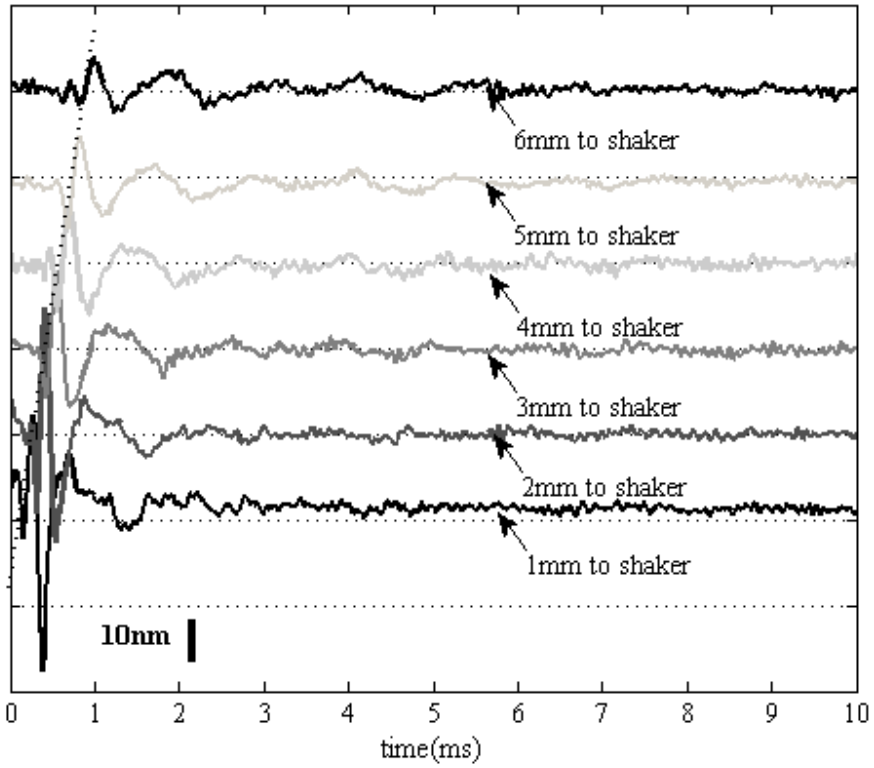

Fig. 6.6 SAW signals of a single layer 2% phantom at a distance of 1mm (bottom) to 6mm (top) from the shaker head, with 1mm/step. The bar indicates the estimated displacement of the SAW.

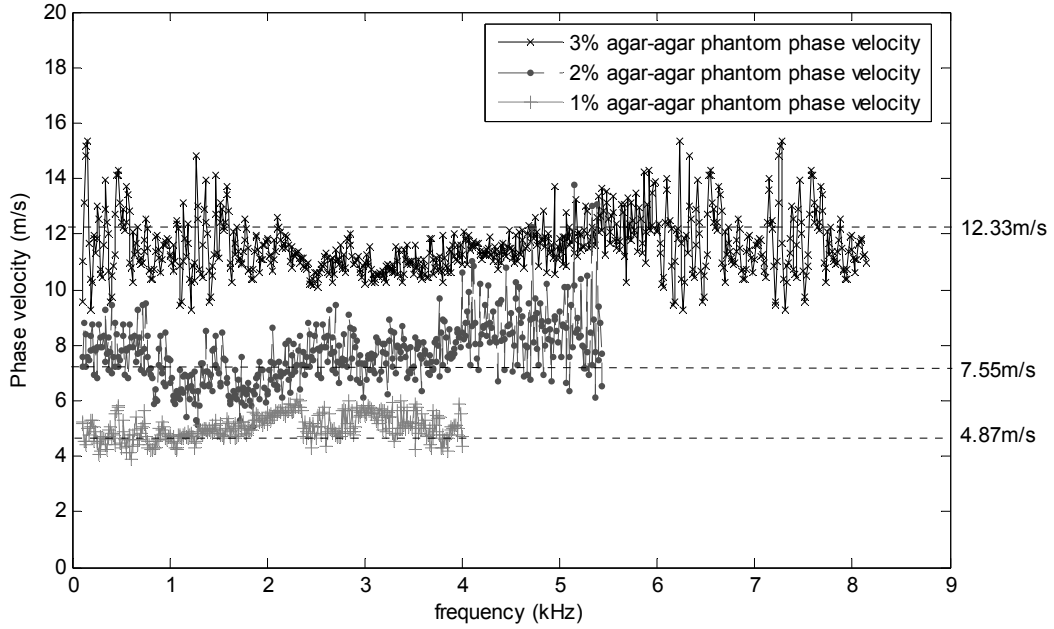

Fig. 6.7 Phase velocity dispersion curves of 1%, 2% and 3% phantoms

Fig. 6.8 shows different the phase velocities and Young's moduli with different agar concentrations. The phase velocity of each agar sample increased linearly with the increase of the agar concentration. The calculated Young's modulus (Fig. 6.8 (b)) increased quadratically with the increase of agar concentration. The experimental results agree with those from others the literature records [1, 3, 38, 190-192], indicating the validity of proposed approach using SAW method to evaluate the mechanical properties of the soft tissues.

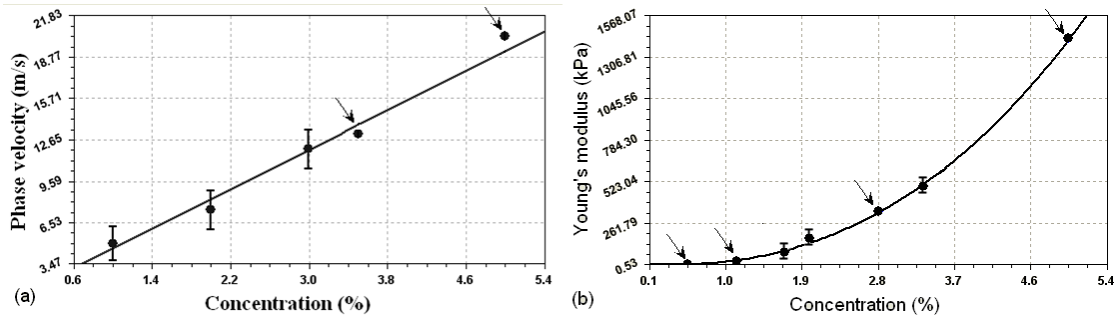

Fig. 6.8 Phase velocity (a) and Young's modulus (b) as a function of single layer homogeneous agar phantom concentration. The black arrows indicate the values extracted from a previous study [1, 3, 69, 195-197]

6.3 SAW method in soft solids with axial elasticity alteration

The advantage of SAW method is to quantitatively evaluate the mechanical properties of layered material, which is promising in skin applications, since skin is a

typical three layers material. The experiment continues to analyse the SAW's behaviour in layered soft phantoms.

Double layer phantoms were prepared with 1% over 2% agar and 3% over 2% agar, to validate our method of evaluating the elasticity of layered materials, such as skin. For both of these double-layer phantoms, a 1 mm and 2 mm upper layer thickness was produced to study the influence of the top layer thickness over the phase velocity curve.

Fig. 6.9 shows the typical SAW obtained from double layer agar phantom, with 2% agar as the substrate layer and 1% agar as the superficial layer with a thickness of 1 mm. The detecting points varied from 1mm to 6mm away from the shaker with 1mm increments. As the wave propagates along the surface of the phantom, the wave disperses due to the heterogeneous environments, which can be determined by a clear wave distortion when travelling away from source. It is because different wavelengths of SAW contents have different wave velocities, they will separate from each other when travel away from source.

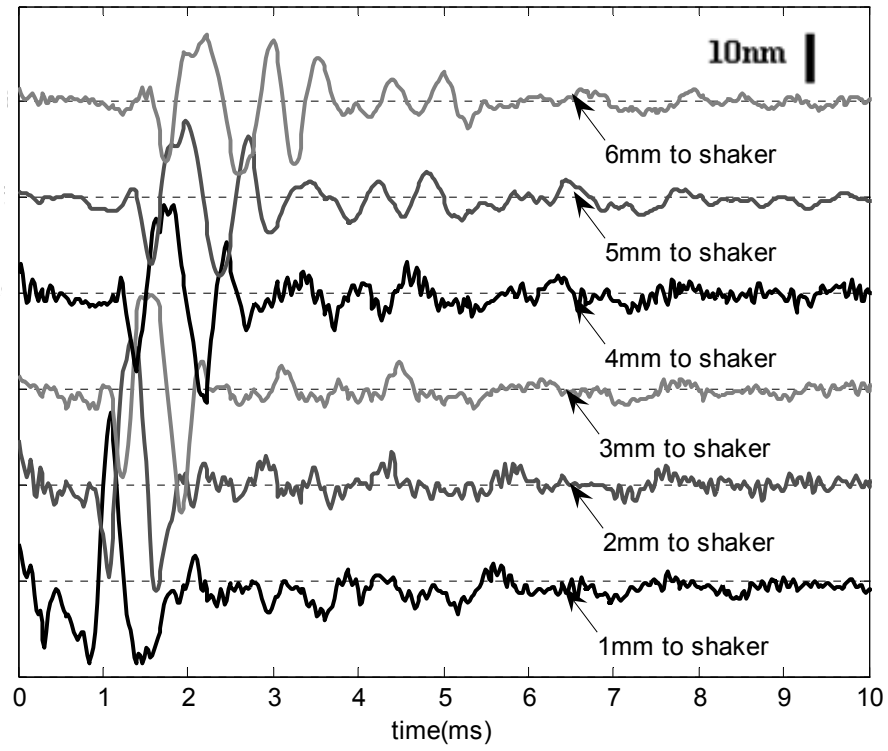

Fig.6.9 SAW signal from a 1mm 1% layer over a 2% substrate at a distance of 1mm (bottom) to 6mm (top) from the shaker head, with 1mm/step.

The phase velocity dispersion curves of the four double layer phantoms are presented in Fig. 6.10. The phase velocity dispersion curves are not constant for all frequencies. The initial phase velocity of these double layer phantoms has a value of

7.5 m/s, which matches the value from the single layer 2% phantom. This is expected since each of the double layer phantoms has a 2% agar phantom as the substrate. However, as the frequency increases, the phase velocity changes due to the influence of the upper layer. The phase velocity increases to 12.5 m/s when the top layer had a 3% agar concentration, and was reduced to 4.80 m/s when the top layer had a 1% concentration. These results agree with the theoretical expectations, where the phase velocity at lower frequencies indicates the mechanical properties of deeper tissue layers, while the phase velocity at higher frequencies indicates the mechanical properties of the superficial layers.

The frequency is dependent on the thickness of the superficial layer. Thicker layers change the phase velocity at lower frequencies. The 2mm top layer phantom saturates at frequencies greater than 1.5 kHz while the 1mm top layer phantoms saturates at 2.2-2.8 kHz. Notice that the 2mm 3% agar layer on 2% agar phantom was noisier than the other three curves. This was because the scattering coefficient in that phantom was lower than the other phantoms (fewer drops of milk were added into the agar solution), which would lead to weaker OCT signal values, and thus higher inaccuracy in the phase estimation.

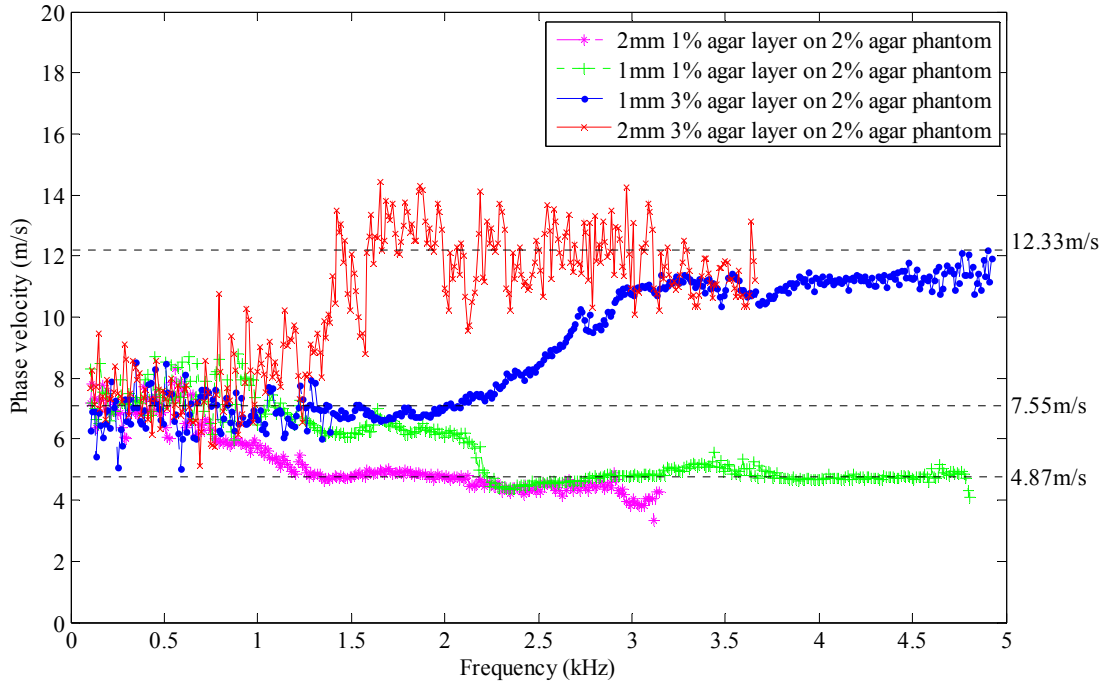

Fig. 6.10 Comparison of phase velocity dispersion curves between double layer phantoms with different upper layer thickness and agar concentration

6.4 SAW method in soft solid with transverse elasticity alteration

In skin pathologies, the lateral change of biomechanical properties has to be considered because the early stage disease is often localised, meaning the elasticity alters at the boundary between the normal and the diseased skin. In the realistic in vivo situation, the tissue would often exhibit the lateral heterogeneity. In this case, when the acoustic waves travel to the boundary between two materials the acoustic energy is either reflected or transmitted depending on the material acoustic impedances. The acoustic impedance is the product of material density and acoustic wave velocity. The bigger difference in acoustic impedance results in a bigger percentage of energy that is changed at the interface or boundary between one medium and another. When a wave travels from *material 1* to *material 2*, it is required that:

$$\frac{A_t}{A_i} = \frac{2z_1}{z_1 + z_2} = \frac{2\rho_1 c_1}{\rho_1 c_1 + \rho_2 c_2} \tag{6-2}$$

where A_t (A_i) is the transmitted (incident) wave amplitude, z, ρ, and c are the acoustics impedance, density and the acoustic wave velocity of the medium, with the subscript 1 and 2 representing *material 1* and *material 2,* respectively. When the acoustic impedance of the *material 1* is higher than that of the *material 2*, the transmitted wave amplitude would be amplified. Otherwise, it would be considerably decreased. Here, either P-wave velocity and S-wave velocity has been extensively studied previously, no record of SAW is found in literatures.

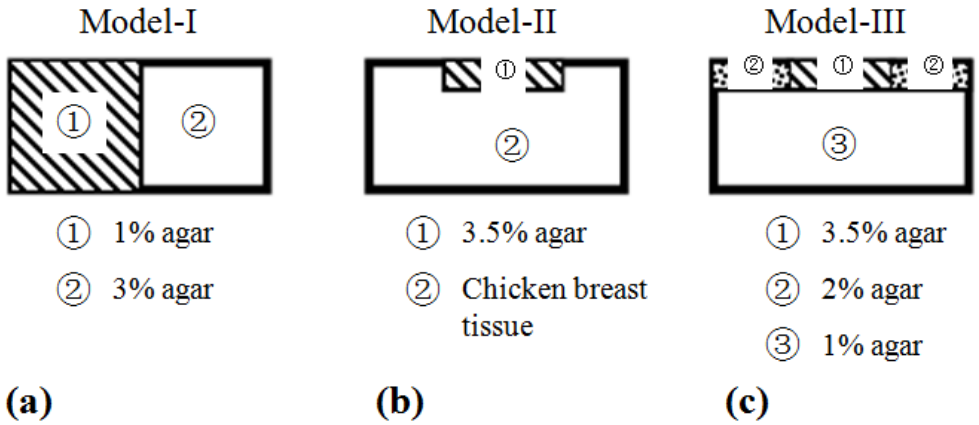

Fig. 6.11. Schematic diagrams of three phantom models, showing the arrangement of the mechanical heterogeneity in phantoms (a) model-I, (b) model-II and (c) model-III

It is important to study the behaviour of SAW travelling through the interface (boundary) at which the alteration of elastic property occurs, so that the feasibility of

SAW method to detect the localized change of elasticity within a mechanically heterogeneous tissue could be assessed. Working towards this objective, three kinds of tissue phantoms (shown in Fig. 6.11) are prepared to simulate the localised change of elasticity, i.e. the alteration of mechanical property in both lateral and axial directions.

For phantom model-I (Fig. 6.11a), it intended to study the behaviour of SAW when passing an interface between two materials with different elasticity to each other. It is known that the higher the agar concentration, the higher the Young's modulus of the gel becomes. Two homogenous agar-gel blocks were made, one with a concentration of 1% and the other of 3%. They then were put firmly together side by side to make the final phantom (Fig. 6.11a, model-I) used in this study.

The skin lesion is often a localized inclusion with differing stiffness, which invades the normal epidermis and dermis. In model-II (Fig. 6.11b), the phantoms were made to test the sensitivity of SAW method to the lateral changes in elasticity. The skin tissue was simplified with homogenous and soft chicken breast tissue onto which a small, thin layer of stiffer mimicking-lesion near the surface was included. To accomplish this, a tissue with a size of approximately 10x10x2 (length, width and height) mm^3 was removed away from the bulk tissue into which 3.5% agar-gel was implanted. In another phantom, instead of using the stiffer agar-gel, a piece of the same breast tissue was simply used to fill the tissue volume that had been removed. This was because the procedures of making phantoms in the chicken breast tissue would inevitably leave a boundary between the bulk tissue and the lesion-mimicking tissue. Thus, this second phantom in this model will enable us to test whether the results obtained are influenced by the existing boundary in the phantom due to the phantom-making.

Skin is a layered biological tissue, implying that the elasticity is altered along the depth, i.e. axially. In model-III (Fig. 6.11c) the layered structures (two layers) were incorporated into the model-II phantom in order to simulate the skin that has a localised lesion, i.e., the elasticity is altered both axially and laterally. Because it was relatively challenging to make such a phantom using chicken tissue, the agar gel was chosen in this case. The bulk phantom was made with 1% agar as the base to mimic the subcutaneous fat tissue layer, on the top of which a 1.5mm thick 2% agar-gel was laid to simulate the dermis layer. A 3.5% agar-gel with a size of approximately 8x8x1.5

mm^3 was implanted in the middle region to make the final phantom (see Fig. 6.11c, model-III).

All the phantoms had a minimum thickness of 10 mm, making the treatment of measurements under the semi-infinite conditions valid. To improve the quality of OCT images to assist the assessment of elasticity, several drops of milk were mixed with the agar solution to increase scattering coefficient.

6.4.1 SAW method in soft solid with only transverse elasticity alteration

Fig. 6.12a and 6.12b show the typical SAW recorded from the model-I phantom (Fig. 11a). Fig. 12a plotted the SAW travelling across the interface (boundary) from stiff to soft tissues while the stimulation was located at the 3% agar-gel site, whereas Fig. 6.12b plotted the results while the stimulation was located at the 1% agar-gel site. The PhS-OCT sampled the SAW first at the position about 2mm away from the shaker head, and then sequentially stepped to the required positions, with a step size of 1 mm, to 13 mm away from the shaker head. It is clear that the SAW was moving away from the excitation position because the arrival time of the SAW was increasingly longer when the detector was located farther away. The diamond sign marked the SAW signal when it was passing through the interface between the two materials with different stiffness. Since it was a single-layer and homogeneous phantom at both the sides of the sample, no velocity-dispersion was found in the waveforms.

When the SAW travels across the interface from stiff to soft tissue s(Fig. 6.12a), the wave speed in the 3% agar phantom (11.58 m/s, evaluated from the diagonal line shown in Fig. 6.12) immediately dropped (4.75 m/s) as if the SAW was travelling in the 1% agar-gel. In addition, the SAW amplitude was amplified at the interface (marked by diamond). On the contrary in Fig. 12b, the wave velocity increased (from 4.66 m/s in 1% agar to 12.06 m/s in 3% agar) but the SAW amplitude greatly attenuated at the interface. The measured SAW phase velocities in the 1% agar and 3% agar-gel sides in the model-I phantoms match well with those measured from the mechanically homogeneous single-layer phantoms reported previously.

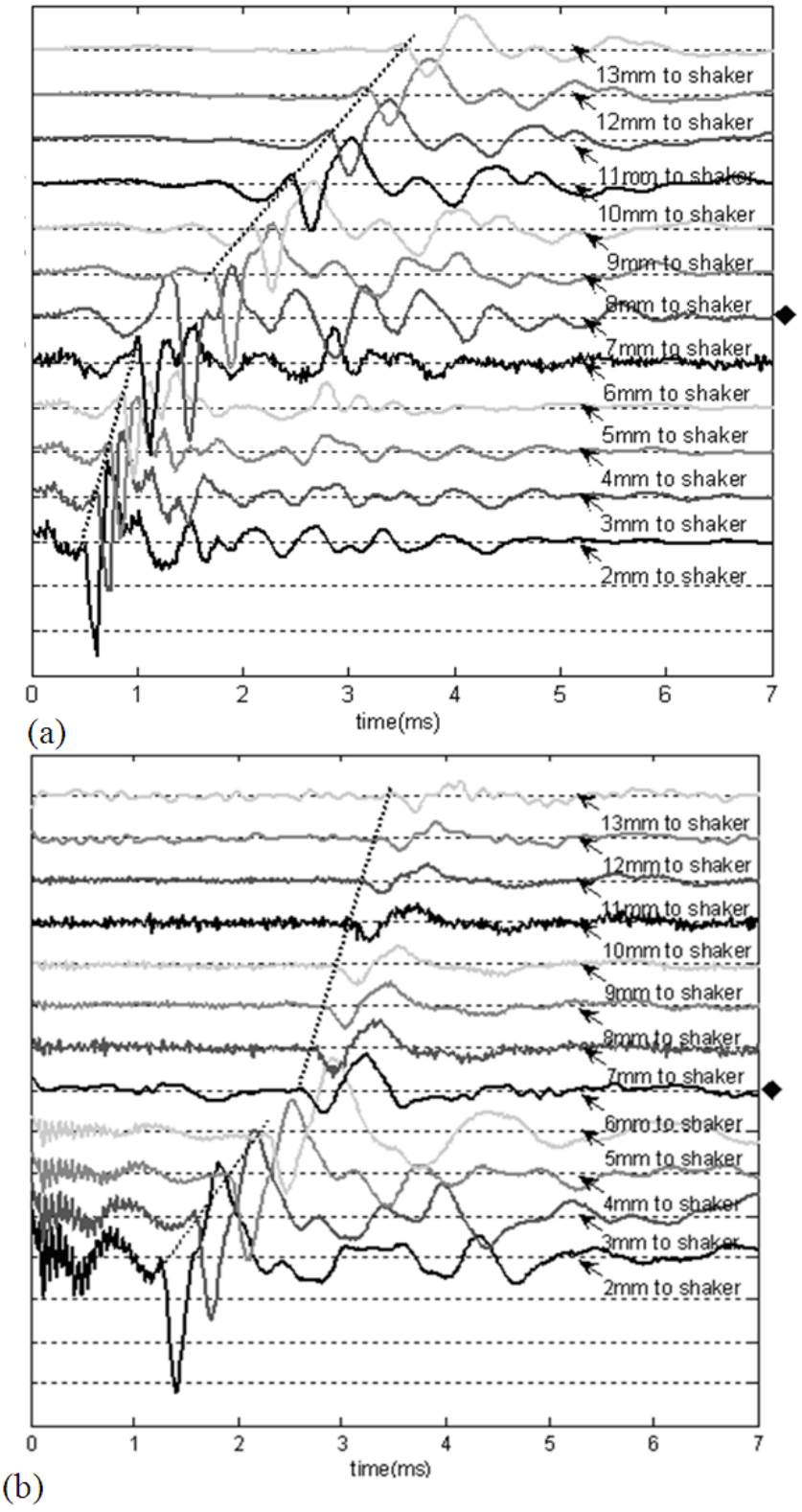

Fig. 6.12. SAW signal measured when it travels across an interface between two materials for the model-I phantoms: (a) from 3% to 1% agar side, while the excitation is located at the 3% site; and (b) from 1% to 3% agar side, while the excitation is located at the 1% site. The diamond marks the interface position.

Table 6.2 Thermal and mechanical properties of Model [171, 175]

Parameters	1% agar	3% agar
Density (kg/m^3)	1060	1080
Specific heat (J/kg·K)	3300	3300
Thermal expansion coefficient (K^{-1})	3×10^{-4}	3×10^{-4}
Thermal conductivity (W/m·K)	0.45	0.45
Young's Modulus (Pa)	87097	511147
Poisson's Ratio	0.49	0.49

To confirm the experimental results, a separate simulation by the use of FEM was conducted in which all the geometrical and physical parameters used in the experiments were used the FEM to obtain the numerical results. SAW were detected at various points on the model surface in sequence, starting from point A (2 mm away laser source) in Fig. 6.13 and ending up at point D (16 mm away laser source) with a uniform distance distribution of 1 mm. A series of detection points were scanned from 1% agar to 3% agar and to 1% agar again. The thermal properties of agar in FE simulation are collected from literature [171, 175] while the mechanical properties are obtained from experiment data present previously (shown in Table 6.2). SAW waveforms represented by the out of plane displacement were shown in the Fig. 6.14 and the wave troughs were traced.

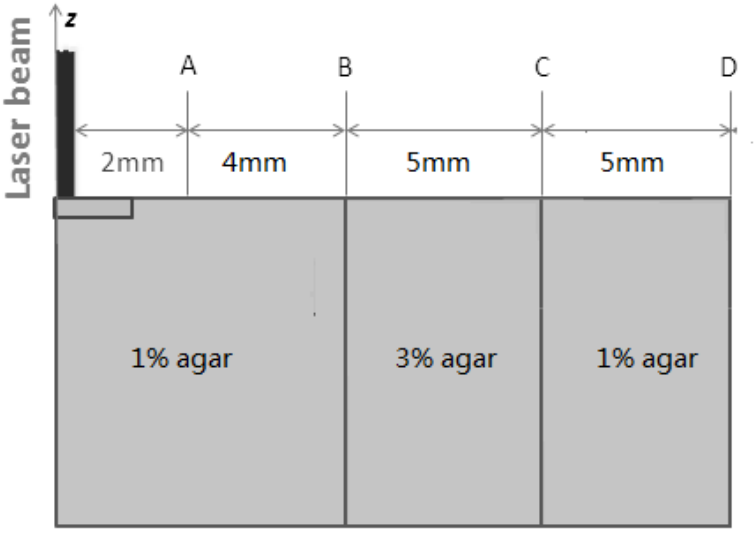

Figure 6.13 Schematic of the geometry of FEM surface and the dimension of interest

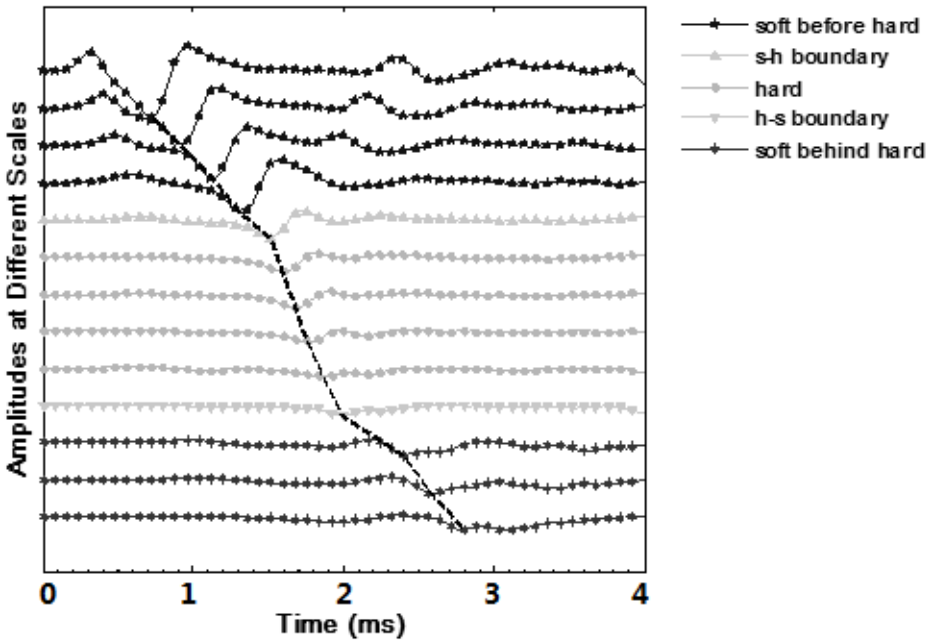

Figure 6.14 SAW (out of plane displacement) detected on the surface of FEM

The simulated results of the SAW amplitudes are given in Fig. 6.15 along with those from the experiments for comparison. In addition, the experimental results obtained from the single-layer and mechanically homogeneous agar-gels (for 3% and 1% agar, respectively) are also shown in Fig. 6.15 to facilitate the comparison. From Fig. 6.15, it can be observed that for the mechanically homogeneous phantom of either 3% or 1% agar-gel, the SAW amplitude follows approximately an exponential attenuation when it travels away from the origin. For the model-I phantom, the SAW amplitude initially follows that from the homogeneous phantom until the SAW arrives at the interface. After the SAW crosses the interface, its amplitude is increased by 150% when travelling from 1% agar side to 3% agar side (Fig. 6.15a). In contrast, the SAW amplitude is decreased by 50% when travelling in the opposite direction (Fig. 6.15b). Both of the experimental and FEM simulation results matches well with the theoretical expectations by Eq. 6-2, which indicates that the wave amplitude would increase by 150% when passing through the interface from 3% agar to 1% agar, and drop by 50% when crossing the interface from 1% agar to 3% agar. Note here that in the theoretical estimation using Eq. 6-2, the necessary parameters were estimated based on the prior study. The SAW velocity of 1% agar was 5 m/s and that of 3% agar was 12 m/s; and the density of 1% and 3% agar-gel were 1020 $kg \cdot m^{-3}$ and 1060 $kg \cdot m^{-3}$, respectively. Note also that when travelling from the stiff side to the soft side, the SAW amplitude

did not increase to its maximum immediately (see Fig. 6.15a). This was most likely due to the localisation error in which the interface was judged visually.

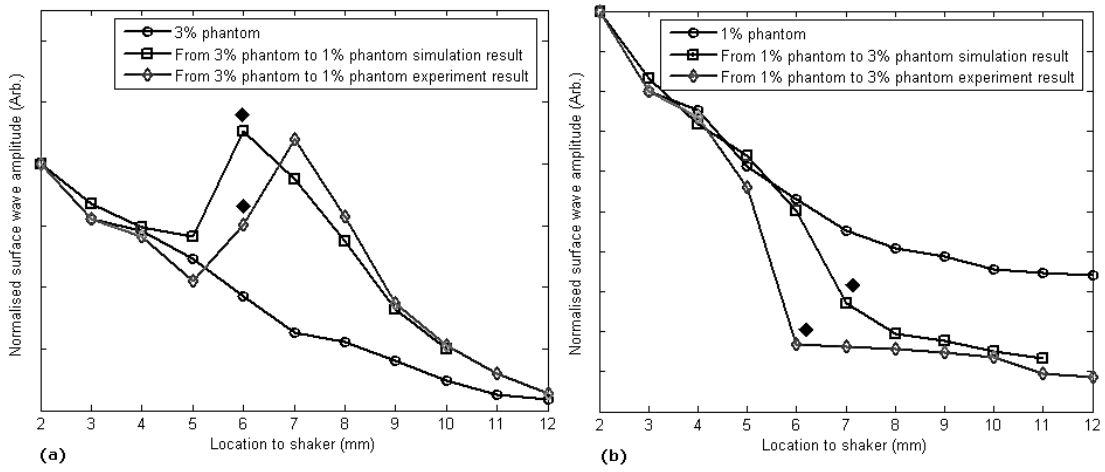

Fig. 6.15. The SAW amplitude evaluated from the experiments and FEM simulations. (a) SAW travels from 3% agar to 1% agar and (b) SAW travel from 1% agar to 3% agar, the diamond mark indicate the interface position.

These results demonstrate that the SAW method is sensitive to the lateral change of elasticity in tissues, as measured by either the SAW velocity or the SAW amplitude. When crossing the boundary between two materials with differing elasticities to each other, the SAW travelling speed would immediately adapt to that of the material. And more importantly, the observed abrupt change of the SAW amplitude can be taken as a marker to indicate that the SAW has travelled from one material to another and tell the relative location of material interface to the shaker, serving a potentially useful purpose in biomedical diagnosis.

6.4.2 SAW method in soft solid with thin layer of transverse elasticity alteration

Next, the model-II phantoms were used to analyse the sensitivity of SAW method to a localised lateral alteration of elasticity. In order to make sure the enclosure of the localised stiffer material near the surface of the bulk chicken tissue, firstly the imaging mode of the PhS-OCT system was used to acquire cross-sectional microstructures images (B-scan) of the phantoms, immediately before the SAW experiments.

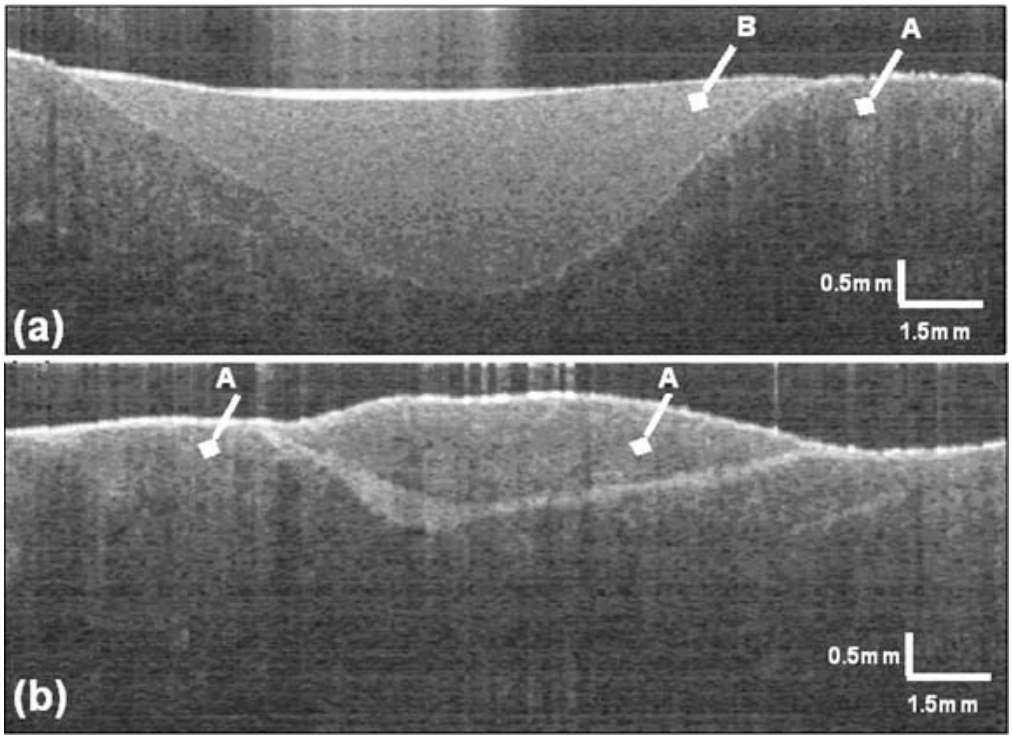

Fig. 6.16. Typical OCT image of the model-II phantom made from the chicken breast tissue. (a) chicken breast tissue as the base and a 3% agar-gel as the inclusion with a differing elasticity; and (b) chicken breast tissue as the base and another small but the same tissue as the inclusion near the surface. "A" shows the chicken breast tissue and "B" indicates the agar inclusion.

Fig. 6.16a shows the typical OCT image scanned from the phantom with the chicken breast tissue as the base and with 3.5% agar-gel as the localised stiffer inclusion to simulate a skin lesion, where the area "A" indicates the chicken breast tissue and the area "B" indicates the 3.5% agar-gel inclusion. The OCT image clearly demarcates the mimicked skin lesion that measured 10x1.8 mm^2 in size (width x depth). Fig. 6.16b shows the typical OCT image obtained from another phantom made from the chicken breast tissue as the base with a small inclusion of the same tissue near the surface. As mentioned before, the second sample was made to check whether the existing boundary had an impact on the measured SAW results. In order to facilitate the discussion, the phantoms shown in Fig. 6.16a and Fig. 6.16b are named Model-IIa and Model-IIb phantoms, respectively.

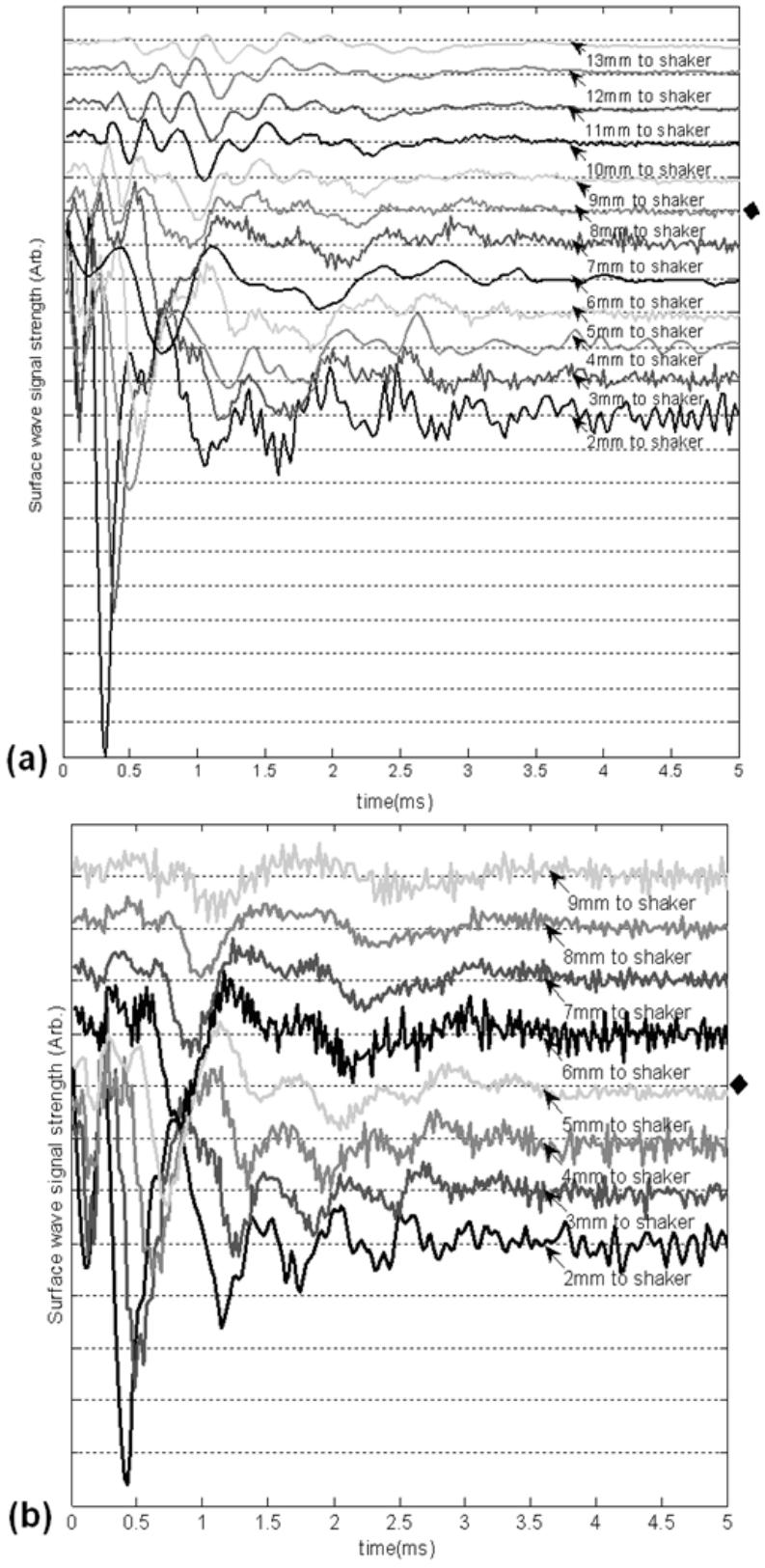

Fig. 6.17. SAW signal measured when it travels along: (a) the model-II phantom and (b) the model-IIb phantom, respectively. The signal was measured initially at 2 mm position away from the excitation (bottom curve), and then sequentially stepped with 1 mm step size until 13 mm away from the excitation (top curve).

Figures 6.17 shows the typical SAW data measured from the Model-IIa and Model-IIb phantoms. The detection step was set to 1 mm, started from the location at 2mm away from the excitation and finished at the location 13 mm away from the excitation, which distance span covered the interface between *ex vivo* chicken breast and mimicking lesion. From Fig. 6.17a it can be seen that the SAW began to disperse after it crossed the interface between chicken and agar, indicating that the SAW was travelling in a heterogeneous medium. On the other hand, there was no dispersion observed for the chicken-chicken sample (Fig. 6.17b, Model-IIb), indicating the sample was a homogeneous material.

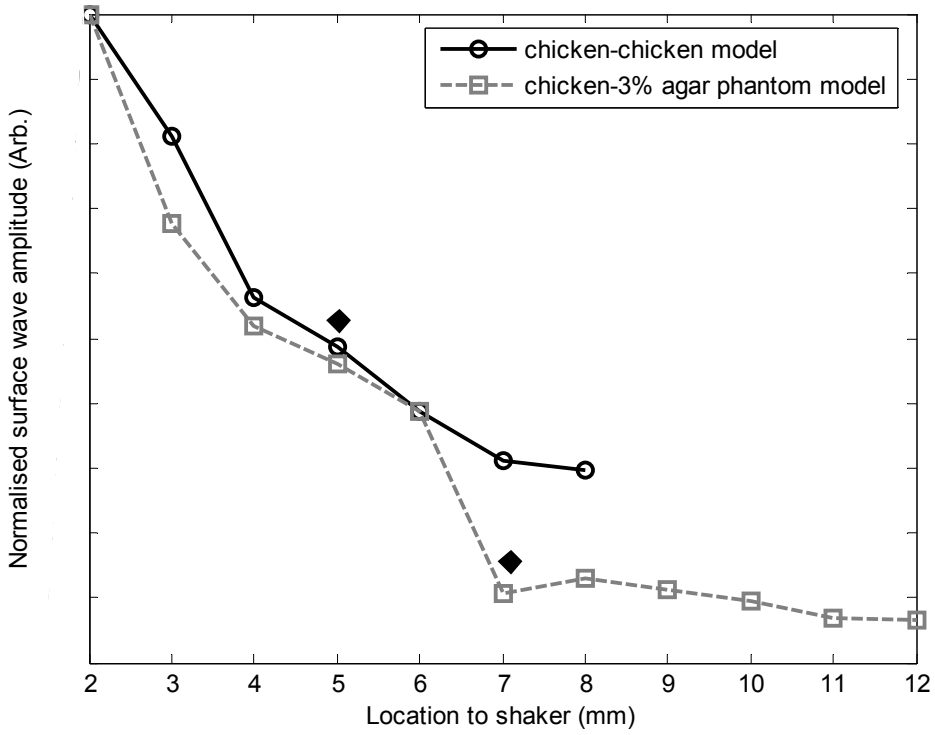

Fig. 6.18. SAW amplitudes measured when the SAW travels in the model-two phantoms. The dark diamond mark indicates the position of the interface.

The changes of SAW amplitude when travelling at the surface of the phantom were plotted in Fig. 6.18, from which a significant attenuation was observed when the SAW travelled cross the boundary between chicken-3% agar in Model-IIa phantom. Assuming the chicken tissue and agar gel used in this study have the similar mass density (which is valid in our current study), the above result implies that the SAW velocity of 3.5% agar is higher than that of chicken breast, indicating that 3.5% agar has higher Young's modulus. On the contrary, when SAW passed through the interface

of chicken-chicken phantom (Model-IIb), no abnormal attenuation in SAW amplitude was observed, indicating that the phantom was almost mechanical homogeneous, in other words, the boundary in the Model-IIb phantom did not have an effect on the proposed system sensitivity to measure the SAW.

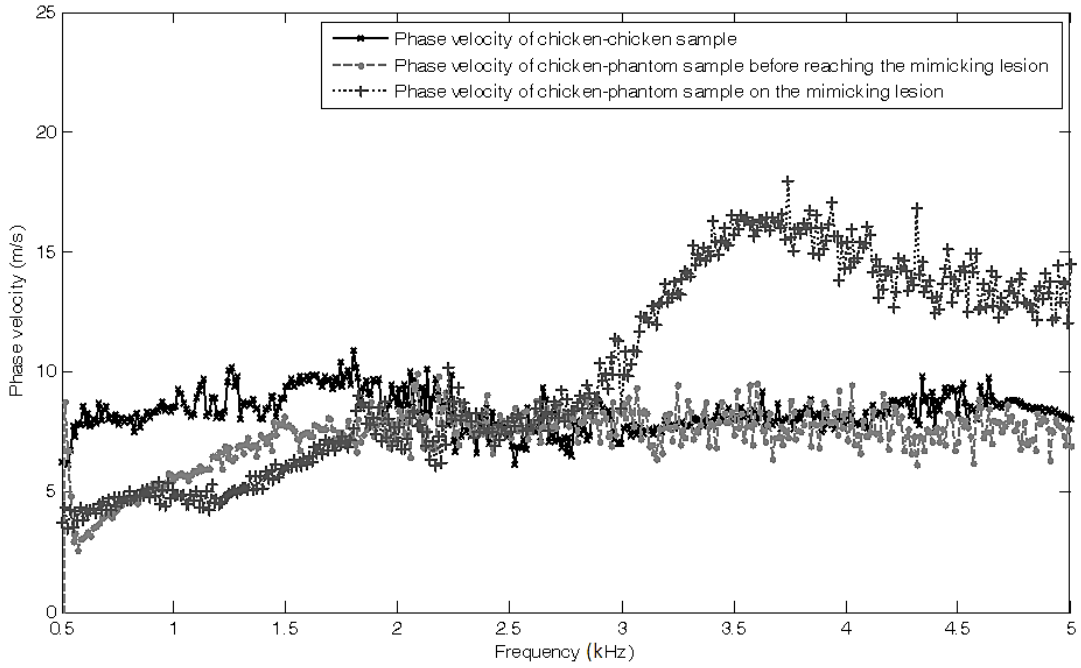

Fig. 6.19. Comparison of phase velocity dispersion curves between SAW before and within the mimicking lesion for the model-two phantoms.

The results illustrated in Fig. 6.19 phase velocity curve of the SAW in the Model-IIb phantom (i.e., chicken-chicken sample) was almost a straight line (7.19 m/s), asserting that the Model-IIb phantom was mechanically homogenous. The similar phase velocity curve (6.89 m/s) was also observed for the Model-IIa phantom (i.e., chicken-3.5% agar sample), only before the SAW travelled into the mimicking lesion area. Note that a small difference in the low frequency contents of these two curves might be caused by dehydration of the chicken sample, as the same piece of chicken was used in both experiments. It is observed that the calculated phase velocity increased after the SAW crossed the interface of chicken and 3.5% agar, showing the material was no longer mechanically homogenous. The phase velocity (7.08 m/s) in the low frequency content (below 3 kHz) represents the substrate chicken tissue, whereas the phase velocity (13.13 m/s) in the high frequency content represents the 3.5% agar mimicking lesion, giving the Young's modulus of 96 kPa and 595 kPa, respectively. The Young's modulus was calculated by assuming the Passion's ratio of

0.47 and the density of 1060kg·m^{-3} for the 3% agar, and 0.49 and 1060kg·m^{-3} for the chicken breast tissue, respectively. The evaluated elasticity values agreed well with the expectations drawn from the SAW amplitude measurements shown in Fig. 6.18. In addition, the thickness of the lesion can be estimated from the phase velocity curve. In this case the calculated depth of lesion was 1.96 mm, agreed well with that measured from OCT images (1.8mm). Notice that the final phase velocity dispersion curve was determined by averaging all the phase velocities between any two available detection points. As a thicker layers change the phase velocity at lower frequencies and a thinner layer change the phase velocity at higher frequencies, the calculated depth (1.96mm) from phase velocity of SAW propagate into the mimicking lesion area will be greatly influenced by the maximum depth. However, if adjacent phase velocity curves are calculated, it is possible to observe the depth change which corresponds to the curve shape of lesion.

6.4.3 SAW method in soft solid with transverse combining with axial elasticity alteration

The experiments with the model-II phantoms demonstrate that the SAW method is sensitive to the thin layer of lateral alterations in elasticity. It is possible that the SAW amplitude diagram can be used to locate the material interface, while the SAW phase velocity curve can be used to provide the elasticity information of different layers, as well as the thickness information about the inclusion with differing elasticity. In addition, we showed that the existing boundary between two materials but with the same elasticity would not have an impact on the estimations of both the SAW amplitude and phase velocity. However, because the skin is a layered structure, it is necessary to incorporate the layered features into the model-II phantom so that the sensitivity of SAW method to both the lateral and vertical elasticity changes can be assessed. The following study with the model-III phantom was designed to achieve this goal.

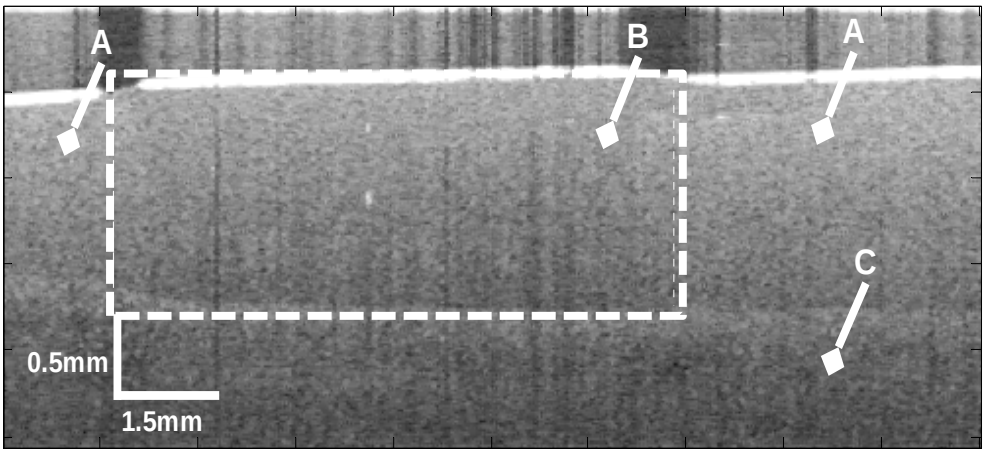

Fig. 6.20. Typical OCT B-scan image acquired from the model-III phantom, where "C" indicates the substrate layer (1% agar), "A" the upper layer (2% agar), and "B" the inclusion (3% agar), respectively

Fig. 6.20 demonstrates the typical OCT images acquired from the model-III phantom, which was made with 1% agar as the substrate layer (area "C", mimicking the subcutaneous fat), 2% as the upper layer (area "A", mimicking dermis) and an 3% agar inclusion (8x1.3 mm^2; width x thickness) (area B, mimicking skin lesion). Fig. 6.21 shows the typical SAW curves measured from this sample. The detection points started at the location 2 mm away from the excitation, stepped across the sample with 1mm increments and finished at the position 19 mm away from the excitation, within which the whole inclusion was covered in the measurements. In this case, the system experienced two interfaces, one when stepping into and another out of the inclusion. Because this phantom had layered structures, the SAW dispersion was observed at all the measured locations as expected.

Fig. 6.22 gives the extracted SAW amplitudes at all the measured positions, which suggests that the SAW was greatly attenuated when it crossed the interface between 1% agar and 3% agar, and then increased when it travelled back into the 1% agar. Both of the SAW waveforms and amplitude changes matched with the width of the mimicking abnormal inclusion, as visualised and measured by the OCT B-frame images, demonstrating the feasibility of using the SAW method to localise the inclusion with different elasticity from the substrate, important for developing this method into a diagnosing tool to differentiate the diseased lesions from the peripheral normal tissues.

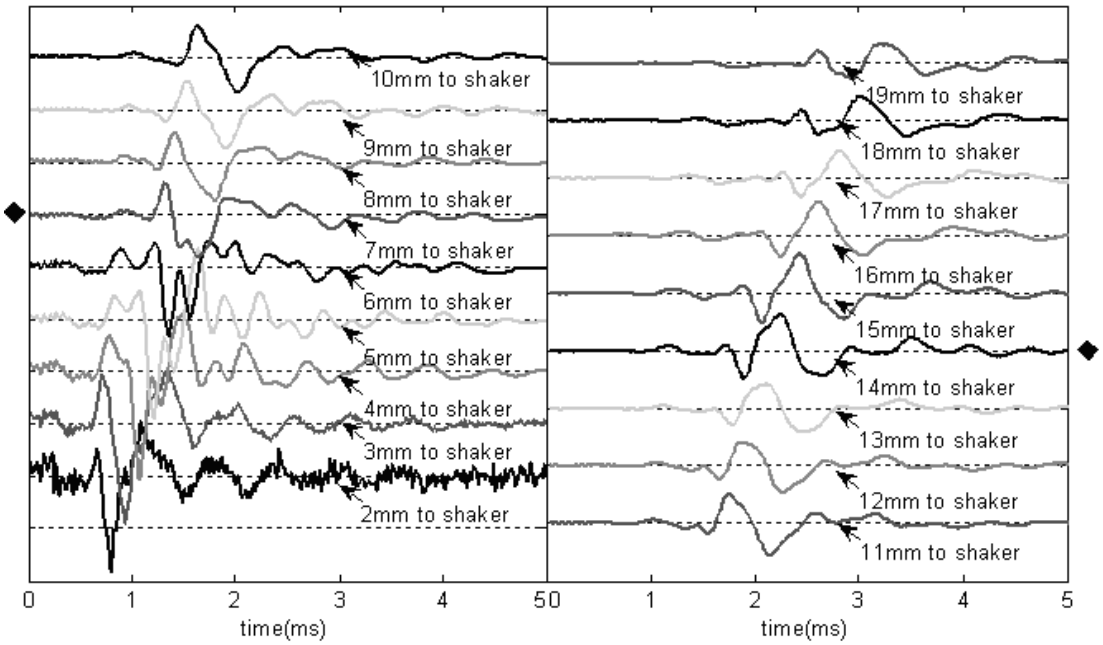

Fig. 6.21. SAW signals measured from the model-III skin phantom starting at 2 mm (bottom in the left) and ending at 19 mm (top in the right) locations away from the excitation, with a 1 mm per step in between. Black diamond's marked the locations of the interfaces of the inclusion.

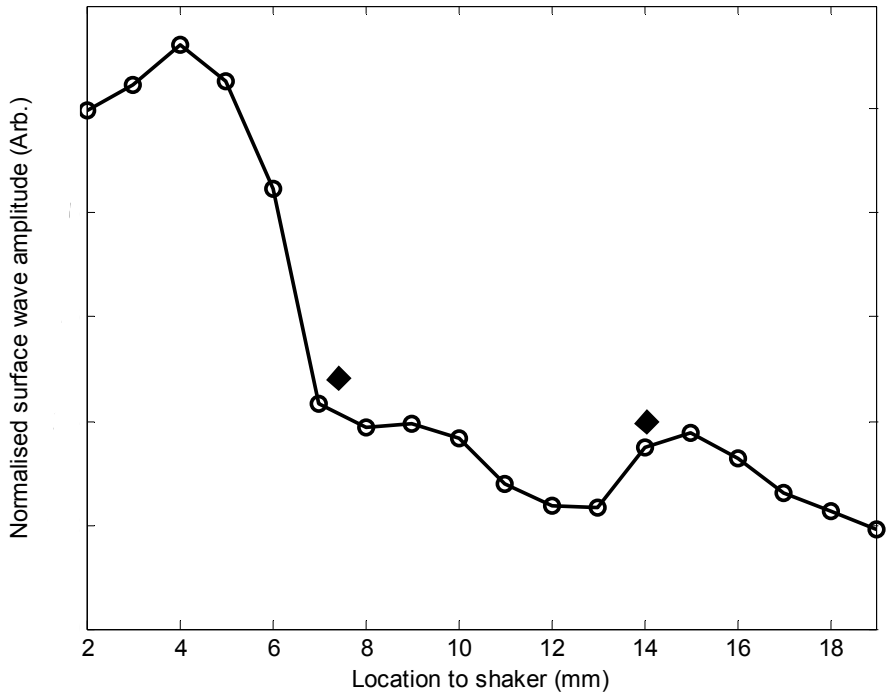

Fig. 6.22. SAW amplitudes measured from the model-III phantom, the diamonds indicate the locations of the interfaces.

The evaluated SAW phase velocity curves before, within and after the SAW passed the mimicking lesion are provided in Fig. 6.23 for comparison, where we can clearly observe that the phase velocity curves before and after the SAW passed through the inclusion were similar to each other. The phase velocity values were evaluated to provide 4.79m/s in the low frequency contents, which increased to 7.5 m/s at 3.2 kHz, representing the mechanical properties of the substrate layer and upper layer, respectively. The phase velocity curve for the SAW measured within the mimicking inclusion shared the similar results in the low frequency contents to the other measured locations as expected because they all shared the same substrate layer. However, with the increase of frequency, the phase velocity began to represent the property of 3% agar which was used to mimic lesion layer, for which the phase velocity was evaluated at 12.08 m/s. The calculated thickness of the inclusion from the phase velocity curves was 1.4mm, agreeing with that measured from the OCT B-scan images. Once again, the phase velocity curve demonstrates the capability of the SAW method to provide quantitative mechanical properties of a localised abnormal tissue, as well as the geometrical thickness information.

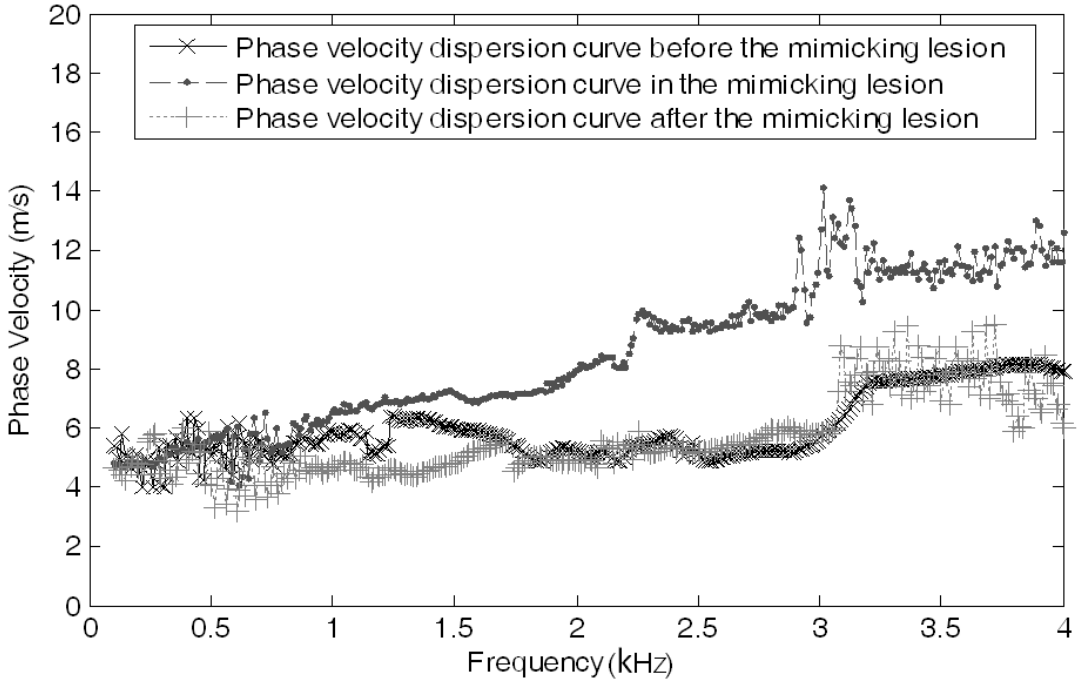

Fig. 6.23. Comparison of phase velocity dispersion curves between SAW when traveling in tissues before, within and after passing the inclusion that mimics an abnormal lesion

6.5 Conclusion

This chapter has presented SAW behaviour in different materials, i.e. hard solid, homogeneous and layered soft mimicking phantoms. From the experiment result we can find that the advantage of SAW method in soft solid: to quantitatively provide the elasticity information of different layers of a material by phase velocity calculation and analysis. Samples with transverse alteration of elasticity were also tested. It is a very important issue as most skin diseases are localised. Through the analysis of the SAW amplitude attenuations, it clearly shows that the SAW method can be used to localise the interface between two materials with different elasticity properties. By analysing the phase velocity curves evaluated from the detected SAW signals, it has shown that the SAW is capable of providing and differentiating the elastic properties of mimicking lesion from the peripheral normal tissues. As a result, the SAW behaviours in axial and transverse alterations of mechanical properties are fully revealed.

In addition, the SAW method can also provide important geometric information of the inclusions, via the thickness and the width, which agreed well with those determined by the use of OCT imaging method. This study represents an important step towards the potential of SAW method as a clinical diagnosis tool to localise the skin lesions, quantify and differentiate the elastic properties of skin diseases from the normal surrounding tissues.

Chapter 7: The development of SAW method in dermatological application

7.1 Introduction

As described in previous chapters, this study has successfully combined phase sensitive OCT (PhS-OCT) with the SAW in evaluating the Young's modulus of thick layered biological phantoms with different models. Using the SAW method, measurements at two locations with known separation distance are required to determine the SAW phase velocity curves, from which the elasticity of the sample is calculated using an inverse method.

This chapter explores the potential of SAW method in dermatology. We firstly apply the SAW method to five Thiel cadavers with different skin sites. *In vivo* human skin (palm and forearm) is then tested. By the signal processing it is able to obtain the phase velocity curves of human skin. However, it is desirable that the elastography as a biomedical property of the tissue to be mapped, to provided direct visualisation of the tissue stiffness for ease of biomedical diagnosis. To fulfil this requirement, this chapter also reports on the use of SAW method, coupled with PhS-OCT, to enable the SAW elastography.

7.2 Human skin elasticity mechanical properties measurement

7.2.1 Thiel cadaver skin mechanical properties measurement

Before *in vivo* human skin mechanical properties measurements, thiel cadavers are utilised to prove the method and the systems are highly sensitive to the elasticity differences of different skin sites. The mechanical shaker was used to stimulate the SAW. Due to the difficulty to install the PhS-OCT system in the cadaver room, the detection of the mechanical impulse induced SAW was accomplished by a Laser-Doppler Vibrometer (LDV) (OVF-534, Polytec, UK) with the maximum sample rate as 20 MHz. The vibrometer decodes the vibration displacement to analogue output, and is digitised using a data acquisition card on NI-PXI system (National Instruments Corp., USA).

Human cadavers embalmed by Thiel's method were processed in the Centre for Anatomy and Human Identification at the University of Dundee, United Kingdom. Thiel cadavers are embalmed in a water-based solution of salts for fixation, boric acid for disinfection, glycol, chlorocresol and ethanol, and a very small amount of formaldehyde. The skin has life-like flexibility, joints are fully flexible, and ultrasound imaging of nerves and needle guidance is realistic. Five human cadavers embalmed by Thiel's method were used; two females (age 58 and 83, embalmed 8 months previously)

and three females (age 36, 83 and 72, embalmed 8-11 months previously). The experiment carried on palm, mid medial backs, forearms, upper arms, mid medial calves and chests of the cadavers, on each anatomy site, the measurement repeated for 6 times in different adjacent regions.

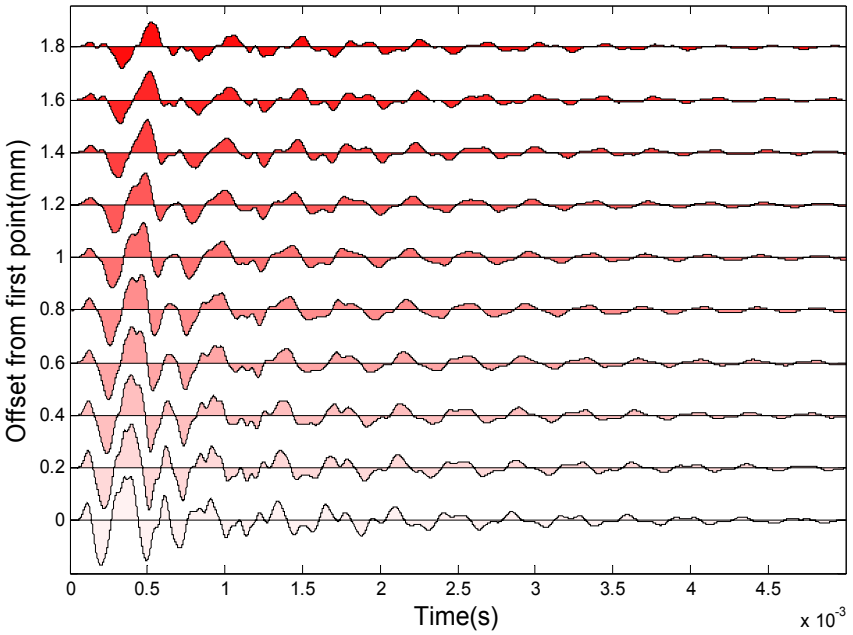

Fig. 7.1 Typical SAW signals (cadaver back skin). First detect point is approximately 4mm from the stimulation centre. Each wave signal is purposely shifted upwards by equal distance for illustrating the waveforms of each detection point with equal spacial interval

Fig. 7.1 shows the typical SAW recorded from Thiel cadavers' back skin. The detecting point begins from 4mm to 6mm to the stimulation center. The SAW is moving away from the shaker-excitation position because the arrival time of the surface wave is longer as the detector is located farther away. The waveform is attenuated clearly with increasing distance from the shaker. However, the dispersion of phase velocity cannot be judged intuitively in the SAWs group.

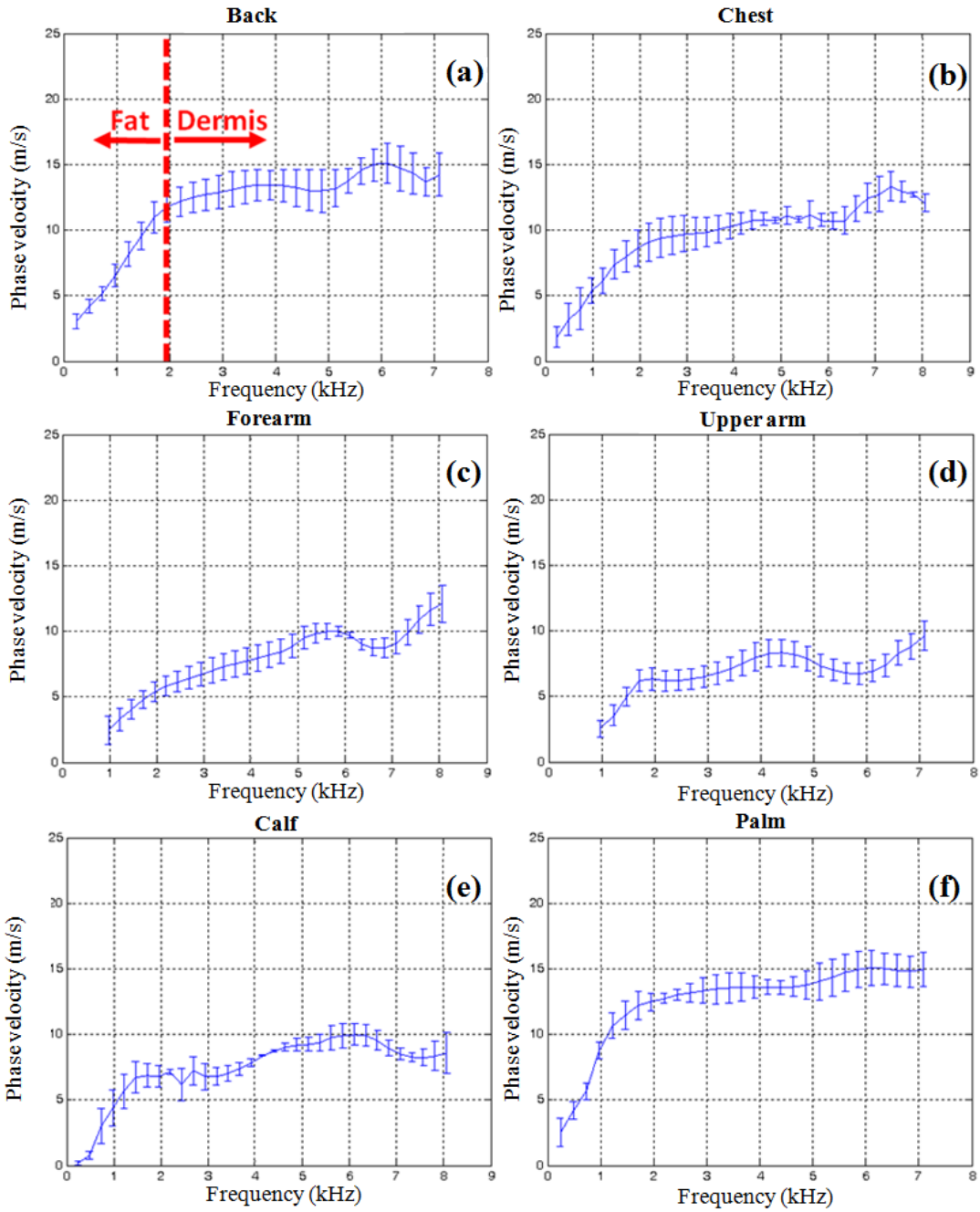

Fig. 7.2 Phase velocity dispersion curves on each anatomy site (a) back, (b) chest, (c) forearm, (d) upper arm, (e) calf, and (f) palm. Error bar indicates the standard deviation between all the phase velocity results on this anatomy site.

The typical phase-velocity dispersion curves of cadaver different skin sites (from the cadaver female, age 58) are determined by averaging all the phase velocities in this waveform group, shown in Figure 7.2. The phase velocity dispersion curves are not constant for all frequencies, which indicate that cadaver skin is not a homogenous but a layered material. Different skin layers have different elasticity. Subcutaneous fat

layer located deep in the skin layers, so the low frequency region in phase velocity curve represent its elasticity information. The high frequency region in the phase velocity curve represents the dermis layer. Take Figure 7.2 (a) as an example, from 0.5-2 kHz, the phase velocity represents the subcutaneous fat layer, with an average value of 5.5 m/s. The phase velocity reaches a plateau of 12.5 m/s at 2 kHz. The plateau value was selected when the value of the phase velocity curve reached 90% of the maximum value after smoothing the curve (the region is separated and marked with vertical dotted lines in Figure 5(a)). These values indicate that the dermis Young's modulus of the dermis is higher than that of the subcutaneous fat. From the phase velocity curves of different skin sites of the Thiel cadavers, it is can be found there are significant differences between the elasticity of skin layers. The back and palm skin are much stiffer than those of other sites.

Table 7.1 Phase velocity and estimated Young's modulus of different anatomy sites in each layer

	Dermis		**Subcutaneous fat**	
	Phase velocity(m/s)	Young's modulus (kPa)	Phase velocity(m/s)	Young's modulus (kPa)
Back	13.45±1.57	662.15±9.02	5.13±0.65	83.81±1.35
Chest	11.12±1.32	452.60±6.38	4.69±0.82	70.05±2.14
Forearm	9.98±1.24	364.56±5.62	4.13±0.53	54.32±0.89
Upper arm	8.56±1.67	268.20±10.20	4.02±0.96	51.47±2.94
Calf	9.73±1.84	346.52±12.39	4.42±1.46	62.22±6.78
Palm	14.03±1.05	720.48±4.04	5.65±0.43	101.66±0.59

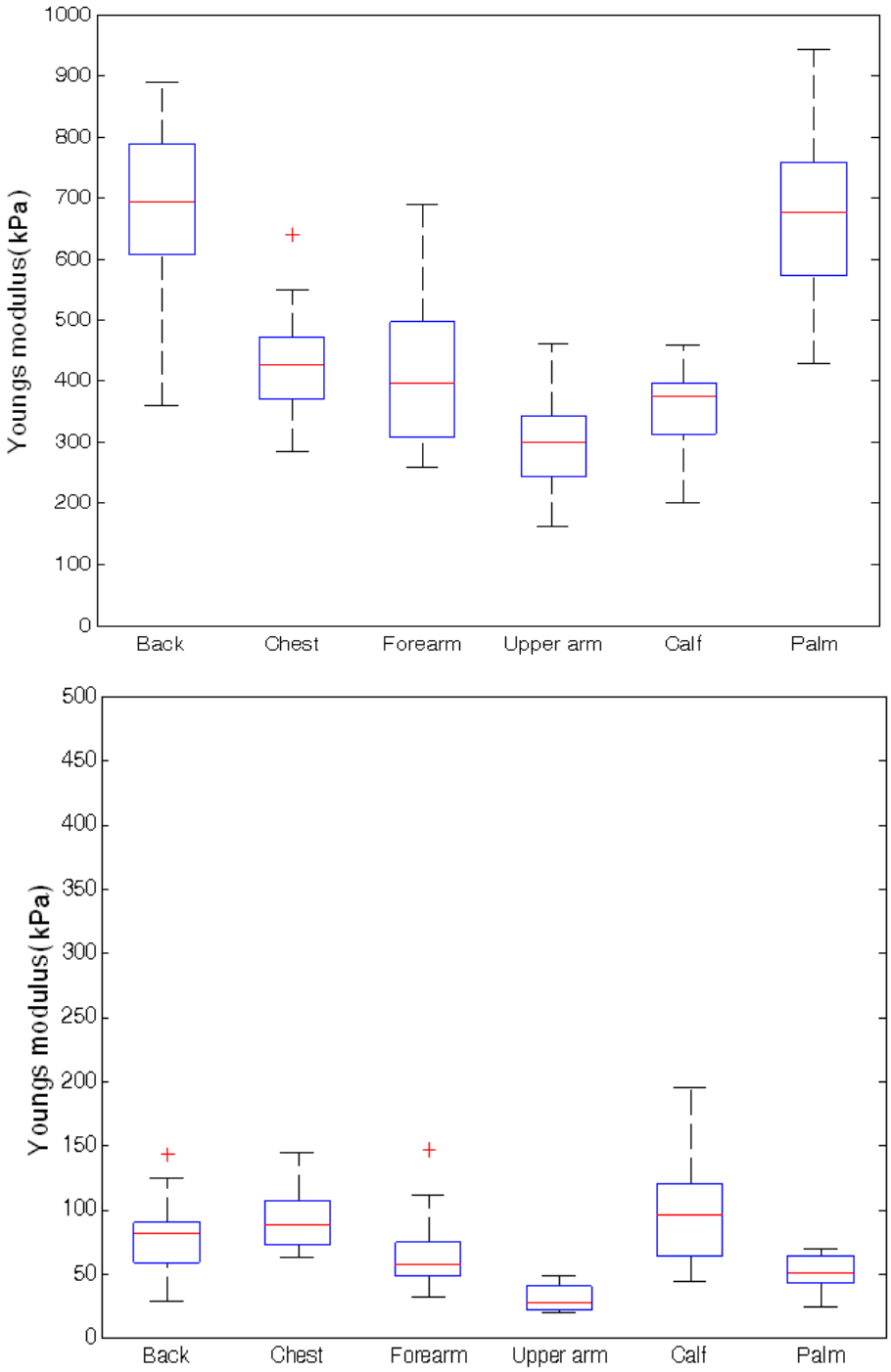

Fig. 7.3 Statistics results of Young's Modulus on different anatomy sites Young's modulus on dermis layer (up) Young's modulus on subcutaneous fat layer (down)

The measured phase velocities for the palm and forearm skins of all the five subjects are summarised in Table 7.1. The results of all phase velocities on different sites in dermis and subcutaneous fat are used to calculate the Young's modulus. The statistics results of calculated Young's modulus are shown as box plots in Fig. 7.3. The box plot is a standardized way of displaying the distribution of data based on the five number

summaries: minimum, first quartile, median, third quartile, and maximum, plus the outside values. In the box plot shown in Fig. 7.3 the central blue rectangle spans the first quartile to the third quartile (the interquartile range). A red segment inside the rectangle shows the median and black lines above and below the box show the locations of the minimum and maximum. The red cross shows the outside values. The data suggest that the elasticity differs significantly between anatomic sites.

7.2.2 In vivo human skin mechanical property measurement

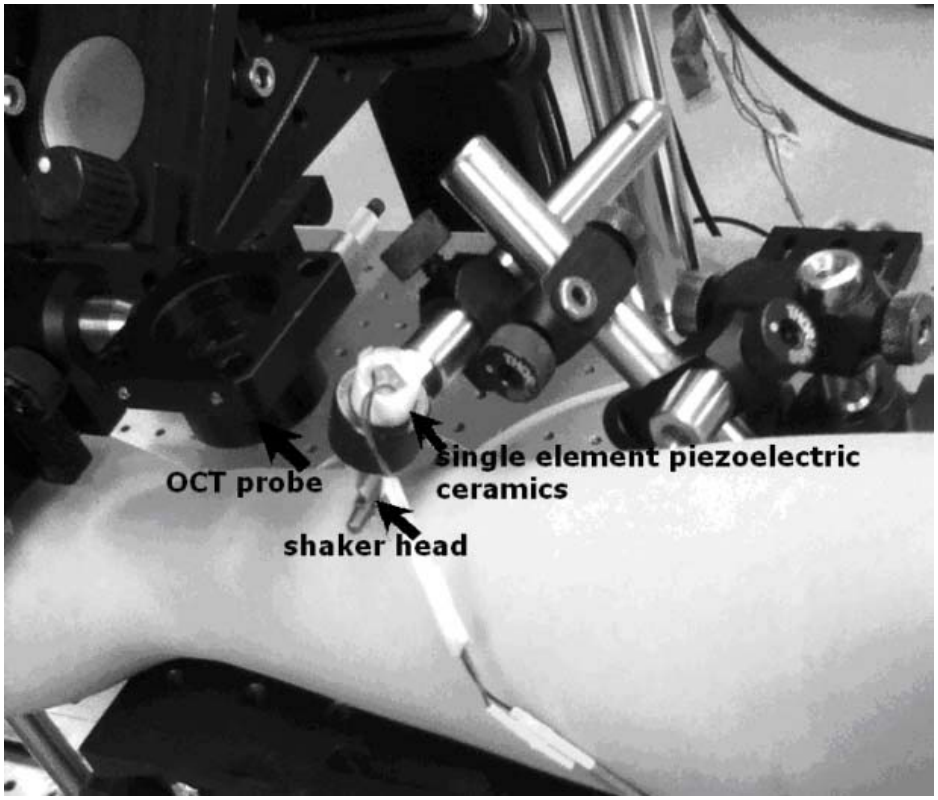

Fig. 7.4 Experimental setup for measuring a human forearm

In vivo experiments were carried on eleven healthy human volunteers with an age span between 25 to 45-years old (4 females and 7 males). These experiments were undertaken under room temperature and humidity. Measurements were obtained from two skin sites, the forearm and the palm. Here, the measurement setup and the analysis procedures were the same as described for the phantom experiments (the combination of mechanical shaker and PhS-OCT is utilized). Fig. 7.4 shows a photograph taken when the measurement was carried out on a human forearm skin. The subjects were asked to keep the arm (palm) stable during the six measurements (6×85 ms). A full

experiment lasted less than five minutes. The shaker head was gently pressed over the skin, and no discomfort was felt by the subjects.

Fig. 7.5 and Fig. 7.6 show the typical SAW from *in vivo* human skin for the forearm and palm, respectively. The detection points varied from 2 to 12mm away from the shaker head in 2mm increments. The SAW signal on the human skin attenuated faster than in the phantoms, which may be due to the high viscosity and influence of the micro-vasculature under the skin.

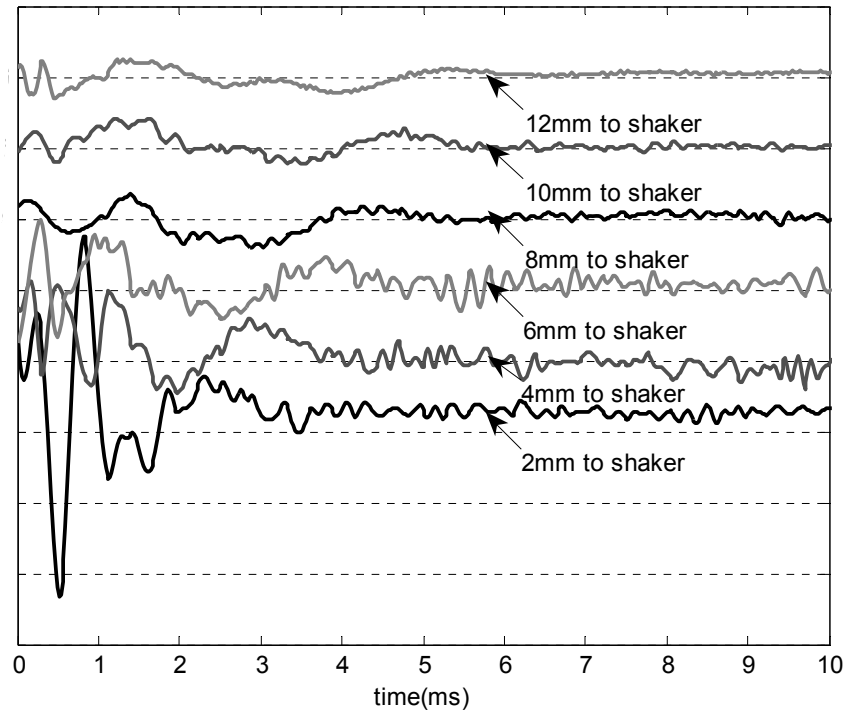

Fig. 7.5 Typical SAW signals from *in vivo* human forearm skin between 2mm and 12mm away from to the shaker head, in 2mm steps

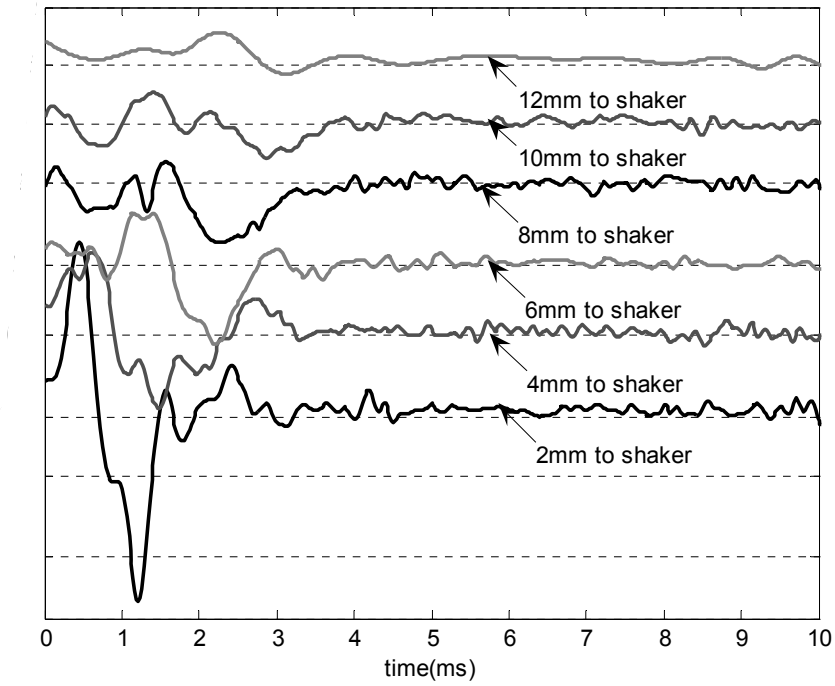

Fig. 7.6 Typical SAW signals from *in vivo* human palm skin between 2mm and 12mm away from to the shaker head, in 2mm steps

The phase velocity dispersion curves of the palm and forearm from one female subject are plotted in Fig. 7.7. The value of the phase velocity in the low frequency for the palm and forearm is similar. At 1 kHz, the phase velocity represents the subcutaneous fat layer, with a value of 4 m/s. The phase velocity increases at higher frequencies which represents the dermis layer of the skin. The phase velocity reaches a plateau of 7 m/s at 4.1 kHz in the forearm and 7.5 m/s at 3.3 kHz in the palm (the plateau is marked with vertical dotted lines in Fig. 7.7). These values indicate that the dermis's Young's modulus of the palm is higher than that of the forearm, and the thickness of the palm dermis layer is thicker than that in the forearm, which is indicated from the phase velocity curve reaching saturation at a lower frequency.

The phase velocity curve shows that the skin model is similar to the double layer phantom with 1 mm 3% agar layer on top of the 2% agar phantom. The Young's modulus of the epidermis cannot be detected by the current system due to the layer being thin and superficial, which requires collecting data at higher frequency range. It is estimated that the shaker pulse will require a pulse of 20 kHz, and the PhS-OCT system will require a sampling rate of 100 kHz, which is higher than the current system range (47 kHz). This study has value since most skin diseases are related to the mechanical properties of the dermis layer.

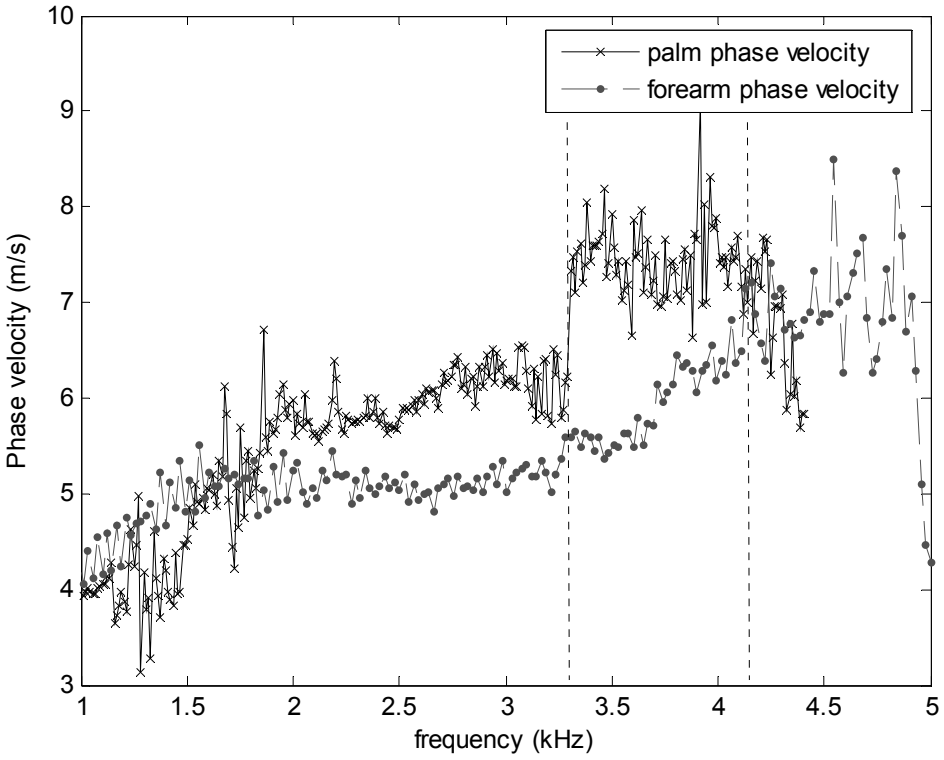

Fig. 7.7 Comparison of phase velocity dispersion curves between palm and forearm (dot line shows the beginning frequency content of dermis layer)

Table 7.2 the phase velocity (averaged) and estimated Young's modulus of eleven subjects in palm and forearm

Subject (F-female M-male)	**age**	**Dermis phase velocity (m/s)**		**Dermis Young's modulus (kPa)**		**Subcutaneous fat phase velocity (m/s)**		**Subcutaneous fat Young's modulus (kPa)**	
		forearm	palm	forearm	palm	forearm	palm	forearm	palm
1F	27	7.02±1.14	7.50±0.55	180.38±4.76	205.89±1.11	4.00±0.38	4.25±0.69	50.95±0.46	57.52±1.51
2F	26	6.45±0.87	7.94±0.52	152.27±2.77	230.75±0.99	3.92±0.27	4.05±0.81	48.93±0.23	52.23±2.09
3F	25	7.17±1.25	7.58±1.15	176.54±5.37	280.96±8.73	3.64±0.95	3.71±0.51	45.50±3.09	49.93±0.94
4F	26	7.94±0.61	7.64±0.96	216.49±1.28	212.01±3.16	4.26±0.54	4.39±0.69	62.32±1.00	69.99±1.51
5M	45	7.37±0.93	8.29±0.61	198.81±3.17	251.55±1.36	4.18±0.41	4.38±0.78	55.64±0.54	61.09±1.94
6M	36	7.24±0.61	7.69±0.48	191.86±1.36	216.45±0.84	4.25±0.35	4.56±0.64	57.52±0.39	66.22±1.30
7M	26	8.85±0.79	10.02±0.51	286.68±2.28	368.22±0.98	4.17±0.55	4.03±0.73	55.37±0.96	51.72±1.69
8M	29	7.47±0.58	8.06±0.39	191.62±1.15	235.96±0.55	3.27±0.85	4.15±0.39	36.72±2.48	62.55±0.55
9M	27	8.52±0.96	8.79±0.62	249.28±3.16	280.63±1.39	4.37±1.63	4.79±0.41	65.58±9.12	83.33±0.61
10M	28	8.76±1.12	8.85±0.85	263.51±4.31	284.48±2.62	4.27±0.56	4.63±0.78	62.61±1.08	77.86±1.94
11M	28	8.61±0.95	9.23±0.78	254.57±3.09	315.50±2.21	4.22±0.84	4.52±1.54	61.15±2.42	74.21±8.61

From the experiments above, the measured phase velocities for the palm and forearm skin of all the 11 subjects are summarised in Table 7.2. To calculate the Young's modulus, the phase velocity value at 1 kHz is chosen for the fat layer, and the phase velocity of the plateau for the dermis layer. Based on previous studies, we can assume that the Poisson's ratio of human skin tissue is 0.48. We used 1,116 $kg \cdot m^{-3}$ as the dermis density and 971 $kg \cdot m^{-3}$ as the subcutaneous fat density. Therefore, with these measured phase-velocity values, we can calculate the Young's modulus.

Fig. 7.8 presents the statistics of calculated Young's modulus of dermis and subcutaneous fat layers from eleven female and male subjects' forearms and palms. As can be found in the figure, the Young's modulus of dermis layer (200kPa) is much higher than that of subcutaneous fat layer (50kPa). The Young's modulus of dermis is higher than forearm. In addition, the females have softer dermis and subcutaneous fat than males.

The results show SAW method combine PhS-OCT is sensitive enough to differentiate Young's modulus between different genders at different skin sites. However, the analysis is not integrated. Factors like age, body mass index, race and the degree of hydration will influence the skin elasticity. Due to the limited number of subjects and incomplete detailed information of subjects, only the differences between female and male palm and forearm have been analysed.

Although the current system is capable of evaluating the Young's modulus from different layers, there are some limitations. The skin layer boundaries are not flat surfaces and the tissue microstructures (such as blood vessels) are ignored. Therefore, there is a higher uncertainty in distinguishing the frequency contents at each layer in the phase velocity curve. The Young's moduli presented in Table 7.2 are estimates obtained from averaged phase velocity values, using values for the Poisson's ratio and density that were found in literature. However, the standard deviations of the phase velocities were small compared to the expected stiffness changes that were found in skin diseases, e.g. basal cell carcinoma tumours being 3 to 50% stiffer compared to healthy skin.

The minimum SAW velocity that the current system can measure is 0.011m/s, determined by the time of SAW travelling between adjacent sampling locations (0.5 mm), corresponding to a Young's modulus 0.45 Pa, which represents the system sensitivity. Thus, the system is sensitive enough to detect very low elasticity (3% stiffer to healthy skin in basal cell carcinoma tumours).

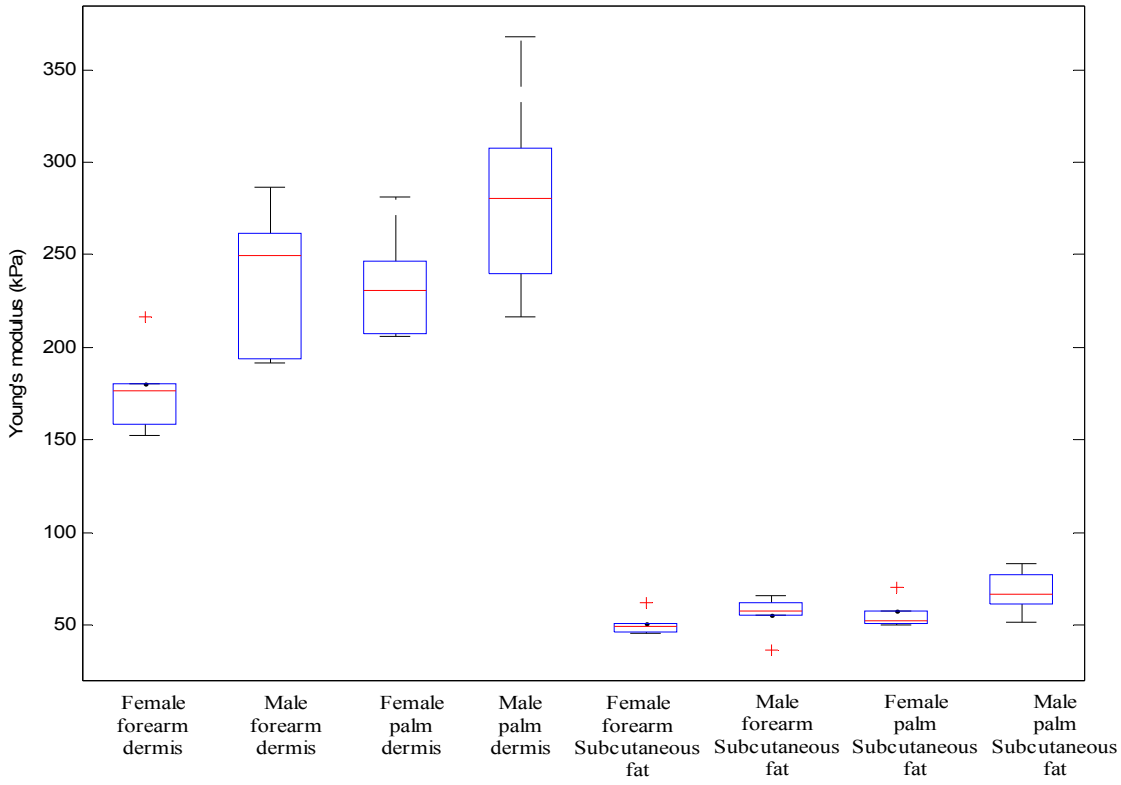

Fig. 7.8 Statistics results of Young's Modulus on forearm and palm dermis and subcutaneous fat in female and male groups

7.3 *In vivo* human skin elastography achieved by SAW method and PhS-OCT

Whilst SAW method is applicable to detect the skin elasticity change, the elastography of tissue can provide direct visualisation of the tissue stiffness in aid of clinical diagnosis. The main concept is to estimate the Young's modulus curve as a function of frequency based on the phase velocity data calculated from two adjacent locations, resulting in an A-line of SAW elastography. After all the adjacent locations are evaluated, a B-scan elastographic image can be built, with its horizontal axis representing the spatial extent (i.e., distance, mm) over the sample and the vertical axis representing the SAW frequency (Hz) that is related to the depth.

The minimum depth that the SAW method can detect is related to the stimulator radius. As the shaker had 2mm radius, the minimum depth of elastography by system was thus 1mm. On the other hand, the maximum depth of SAW elastography can be calculated from Eq. (6-1) by the lowest frequency content and its corresponding SAW velocity. Here, the lowest frequency (typically 1 kHz) was defined by -10 dB from the maximum of the autocorrelation spectrum. The maximum depth that the current

system can sense is 5mm because the SAW velocity was typically 5m/s at 1 kHz in this study.

7.3.1 Agar phantom test

To verify the proposed elastography approach, it firstly used agar phantoms largely because the agar can be easily used to make mechanically heterogeneous samples. We first made a double-layered phantom with 1% agar as the base, and 1.3 mm thick 2% agar as the top layer into which a 3% agar was included in its middle region. The gel was mixed with 5% milk, giving a scattering background to provide a contrast for OCT imaging. This phantom possessed a mechanical heterogeneity that is sufficient to test the sensitivity of the proposed method to differentiate the localised inclusion of the 3% from the 1% and 2% agar-gel background.

The results are shown in Fig. 7.9, where (a) is the structure image of the phantom that provides important geometrical information; and (b) is the resulted SAW elastogram with quantitative Young's modulus given. OCT image showed the boundaries [marked in Fig. 7.6(a)] between areas of different agar concentrations, demonstrating the possible mechanical inhomogeneity of the sample, but is unable to give the elasticity of sample. The mapped elastography by the proposed approach (Fig. 7.9(b)) distinguished the elasticity of regions with different agar concentrations, with its geometry corresponded well with that observed in Fig. 7.9(a). The averaged values of Young's modulus at 3%, 2% and 1% agar concentration regions were 500kPa, 200kPa and 100kPa, agreed well with the values obtained by previous studies where the elasticity of homogeneous phantoms made by different agar concentrations was measured. From Fig. 7.9(b), we can also observe that the interface between 3% and 1% concentration agar appears at 4 kHz because there is an apparent transition of the Young's modulus in the elastography. Thus, this value of 4 kHz and its associated phase velocity (5m/s) can be used to estimate the thickness of the top 3% agar layer, which gives 1.2mm, which matched very well with that measured from OCT image (1.25 mm).

In order to test if the proposed method is able to detect the elascity change within sample, another phantom was made with a 2% agar block embedded inside 1% agar gel. The results presented in Fig. 7.9. The OCT image (Fig. 7.9(c)) confirmed the 2% agar inclusion with a thickness of 1 mm, located at 1.1 mm beneath the phantom surface. Again the SAW elastography resulted from the proposed approach (Fig. 7.9(d))

demonstrated the ability to differentiate the localised mechanical inclusion from the background, with the geometrical appearance of the mechanical heterogeneity matching well with the OCT structure image. From Fig. 7.9(d), we obtained an averaged Young's modulus for 2% agar inclusion of 200 kPa, while that in the background of 100 kPa showed the Young's modulus of 1% agar. The upper and lower boundaries of the 2% agar inclusion can be estimated by the frequencies of 4.5 kHz and 2.5 kHz, corresponding to 1.05 mm and 2.03 mm from the surface of the phantom, agreed well with the OCT measurement (Fig. 7.9(c)). These results demonstrate the feasibility of the proposed method to provide elastrography of the mechanically heterogeneous samples.

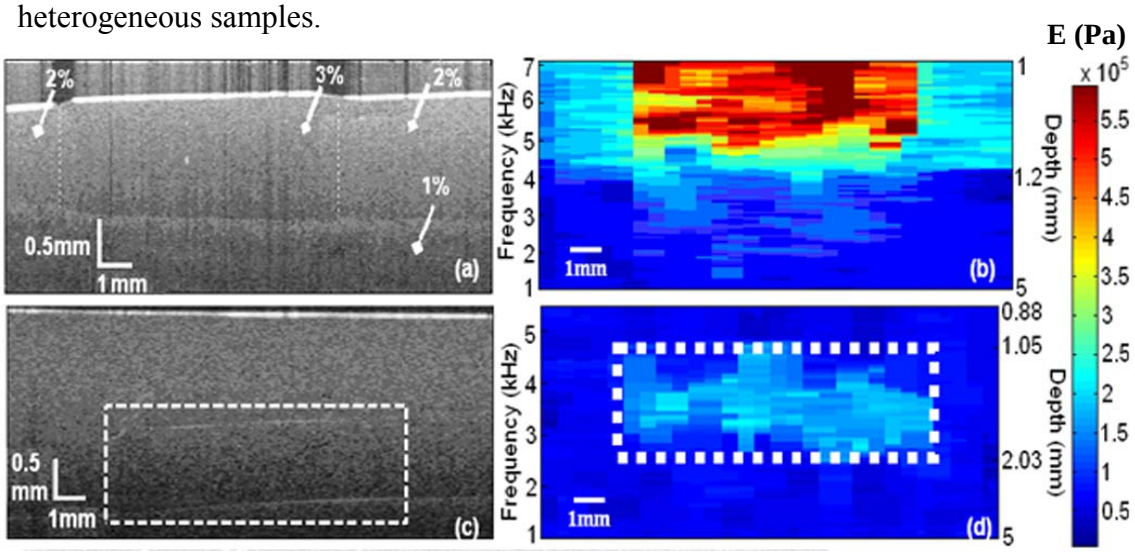

Fig. 7.9 (a) OCT image of the phantom with 1% agar as substrate layer, 2% agar and 3% agar as upper layer; (b) the elastogram of the phantom evaluated from the phase velocity curves. (c) OCT image of the phantom with 2% agar (outlined by the dashed box) embedded within 1% agar background; (d) the resulted elastogram.

7.3.2 In vivo human skin elastography

Finally, we used the proposed SAW elastography method to test on a human forearm skin in vivo with a hard nodule in the dermis layer, which can be observed by OCT image [Fig. 7.10(a)]. From the OCT image, it can be seen that the hard nodule is 0.5mm beneath the surface, but to provide its size was difficult because of the limited imaging depth which was less than 1 mm. The elastographic image (Fig. 7.10(b)) distinguished the stiffness between the nodule and background tissue. At the normal human skin, the Young's moduli gradually decrease from the surface (200 kPa from 5 to 3 kHz, corresponding to the depths from 1.5 to 2.2 mm, i.e. dermis layer) into the depth (100 kPa from 3 to 1 kHz, corresponding to the depths

from 2.2 mm to 4 mm, i.e. subcutaneous fat layer). The Young's moduli measured for dermis and subcutaneous fat layers were consistent with those reported in the prior study. The hard nodule (shown in red color) can be easily distinguished in the elastogram as it has much higher Young's modulus than surrounding tissues, and reaches to 1.85mm deep inside of skin. However, the current system had difficulty to provide mechanical property of the epidermis layer because the minimum depth that the system can measure was 1mm.

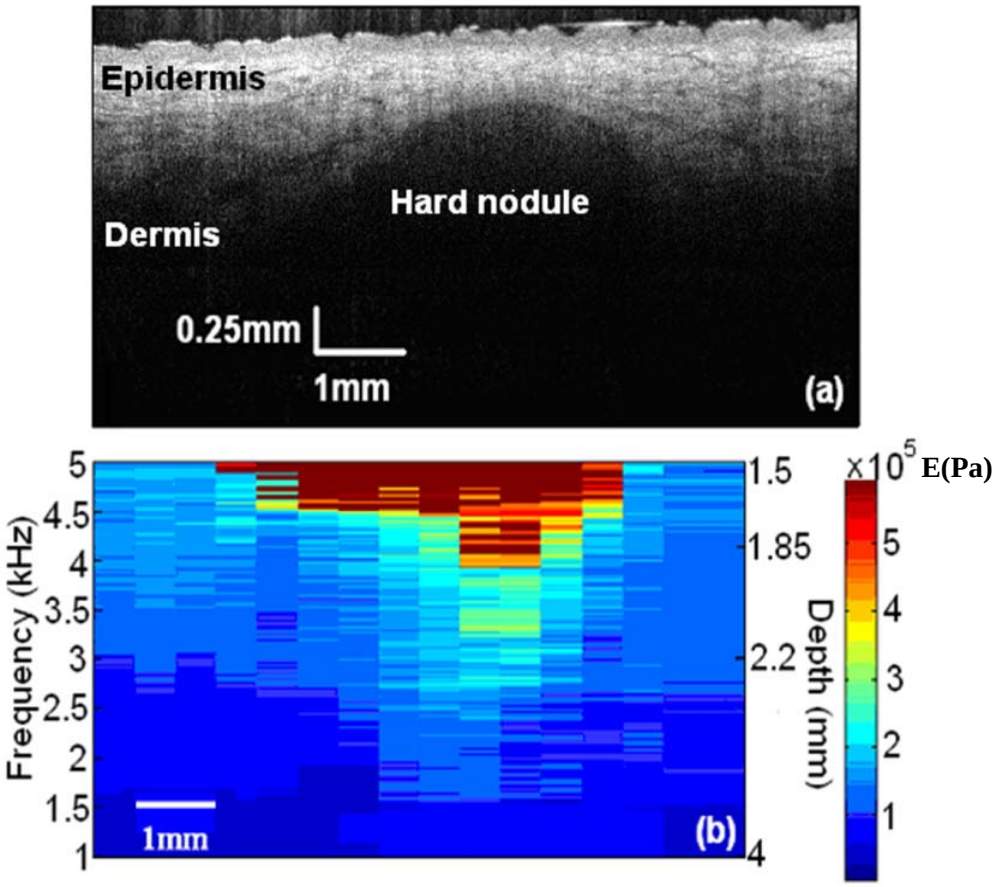

Fig. 7.10 (a) OCT image of human forearm skin in vivo with a hard nodule in the middle; and (b) the resulted elastogram.

PhS-OCT combine SAW method for skin elasticity measurement and elastography has some advantages as well as some limitations. For the advantages: 1) The elastography depth is much higher than traditional OCE, the system can image the tissue with 5mm's depth; 2) the system provide quantitative elastography; 3) due to the dispersion of SAW, this system can provide full information of different layers of skin with one data set. The limitations of the system including: 1) the spatial resolution of the SAW elastography is much lower than that of the prior OCE. This is because the latter relies on OCT to perform the strain-rate imaging, while the former requires

a certain distance for the SAWF to sufficiently disperse so that the phase velocity can be evaluated; 2) Mapping from the phase velocity to the depth information in the SAW elastography is unfortunately a non-linear process, which needs to be further studied in order to provide the elastography in a linear geometrical scale so that it can be directly presented alongside with the OCT imaging for ease of use in biomedical applications; 3) the minimum sensing depth of the current system is limited by the size of the stimulator. This problem is perhaps amendable if a laser source is used to stimulate the SAW because the laser beam can be easily focused, leading to dramatically increased high frequency contents within the generated SAW signals.

7.4 Conclusion

This chapter has presented a technique that combines an inexpensive mechanical impulse response with a PhS-OCT detector to characterise the mechanical properties in vivo human skin. It has shown that the experimental results are in good agreement with the literature. This study proves the feasibility of using SAW method for evaluating elastic properties of soft biological tissues.

The *in vivo* human skin experiments demonstrate that the SAW method could be applicable in clinical settings, because the system is sensitive to the elastic and geometry changes of a sample in the axial direction. Since most skin diseases result in changes of the elastic properties and/or thickness of the affected skin layer, this will cause changes to the phase velocity curve which can be detected by our system. The current system may have potentials in diagnosing diseases of the dermis layer, such as Level II skin cancer (including malignant melanoma, squamous cell carcinoma and basal cell carcinoma) and scleroderma.

In addition, it have demonstrated that the SAW method can be successfully utilised to quantitatively image and map the elasticity of soft and layered heterogeneous tissues. The proposed SAW elastography is independent of the OCT imaging, but utilizes OCT to provide complementary morphological information of the tissue that can be particularly useful for diagnostic purposes.

Chapter 8: Conclusions and Further Work

8.1 Summary

This project aims to develop a new elastography method for fast quantitative elasticity measurement of different skin layers, which can aid medical diagnosis and treatment of skin cancers and scleroderma. Presented here is the first study that reveals the SAW's behaviour in soft material, i.e. soft tissue, and we use impulse stimulated SAW for the rapid functional characterisation of skin, i.e. skin mechanical properties measurement and elastography. By combining it with the PhS-OCT imaging system, the ultra-high resolution of skin structure image can also be obtained.

In chapter 4, the single layer steel and 3.5% agar phantom FE model are created and developed, in order to provide reference to cross validate the experimental data. For the experiment, SAW stimulation and detection systems, i.e. Q-switched high energy pulse and mechanical shaker stimulators, as well as the low coherence interferometry and PhS-OCT detecting system are introduced. The singles layer aluminium and 3.5% agar phantom SAW signals that generated and detected by the systems are then compared with the Finite element modelling.

Chapter 5 introduces the signal processing procedures. Frequency range definition and phase velocity calculation are presented in SASW method. Different de-noising methods are compared, including averaging, wavelet de-nosing and EMD de-noising. The inversion procedure is also introduced to inverse the phase velocity into mechanical properties of the tested samples.

In chapter 6, the behaviours of SAW in homogenous and heterogeneous materials are fully studied. Firstly, SAW frequency range is studied in single layer hard and soft materials. With the decreases of material stiffness, the frequency range of SAW decreases. It has proven that the PhS-OCT has enough bandwidth to detect SAW in soft tissues. Then, behaviours of SAW are analysed in different tissue mimicking phantoms with axial and transverse alteration of mechanical properties. It is proved that the SAW is sensitive to the elasticity change in both directions, and has the possibility to offer the quantitative elasticity properties of localised skin lesions.

The SAW method is carried out on human skins in Chapter 7. We successfully apply the SAW method to detect the Young's modulus of different skin sites of Thiel cadavers. Significant differences between different skin sites can be observed. *In vivo* human dermis and subcutaneous fat layers with eleven volunteers are tested. The results fit well with literature, and a clear difference between the elasticity in dermis, subcutaneous fat in female and male subjects can be observed. SAW can also be

utilized for elastography mapping the skin elastography quantitatively. The combination of SAW elastography and OCT structural images can be a very useful tool in skin diseases detection and treatment evaluation.

8.2 Conclusions

This study demonstrates the first study to prove the feasibility of using SAWs to quantify and sense the elasticity change in skin was studied. The following conclusions can be summarised:

- Among different imaging and elastography methods, optical imaging combine transient elastography method has great potential in dermatological applications. Optical coherence tomography has ultra-high resolution which can differentiate different skin layers clearly. SAW method, as one transient elastography method, has the potential to quantitatively measure the elasticity of different skin layers, which has advantages than other kinds of elastography method;
- FE simulation serves as a very useful tool to guide feasibility experiment and to cross-validate practical experimental data in this study, since no relevant research in SAW in soft tissue has been done before,;
- SAW can be successfully generated on soft solid material by different approaches, including high energy laser pulse and mechanical shaker. Compared with a high energy laser pulse, mechanical shaker is more suitable to use to generate SAW propagating on *in vivo* human skin with the consideration of safety;
- The SAW velocity and frequency range in soft solid is much lower than that in hard solid (about 8 m/s in dermis and 4 m/s in fat tissue, the frequency range of SAW in skin is from 1 Hz to 20 kHz). These features make the SAW detection by PhS-OCT possible;
- Stimulation method of SAW as well as the elasticity of sample will influence the frequency contents of a SAW, the balance between the elasticity of testing material, stimulation method and detection method should be balanced before any SAW research taken place;
- SAW phase velocities, as well as SAW amplitude are sensitive to elasticity change in both axial and transverse directions;
- The SAW phase velocity have relationship with material elasticity, higher SAW phase velocity indicates stiffer material. By signal processing method proposed in this study, SAW phase velocity curve can be calculated and inversed to reveal the

mechanical properties of different models of phantoms (homogeneous, layered and with elasticity change in both axial and transverse directions).

- SAW method combining PhS-OCT system can provide both structure images and elastography of *in vivo* human skin. It can differentiate skin elasticity and thickness of different subjects. Due to high sensitivity, SAW method combining PhS-OCT is feasible in dermatological applications, e.g. skin cancer diagnosis and monitor.

8.3 Future work

The work presented here shows the potentials of the SAW method for the *in vivo* characterisation of human skin elasticity measurement and elastography. There are several straightforward studies and developments which would be logical next steps.

Signal Processing and Algorithm Development

The work carried out in this research involves the development of SAW phase velocity dispersion curves from the generated SAW which gives quantitative information on changes in the geometrical and mechanical properties of the layers. However, the signal processing is not real time. Higher data processing speed is also required to provide results in a real-time quantitative elastography of detecting site of skin tissue, which will be beneficial in clinical applications.

The study aims to make simultaneous quantification of the elastic modulus and geometrical parameters, the elastography will merge with the real-time high resolution OCT imaging of the tested samples. The inversed elasticity information should be simultaneously processed and sent to the real-time OCT imaging software. With the depth-frequency relationship of the SAW method, the elasticity information of a specific depth can be defined in the OCT imaging, with the color map of the elasticity. This will be a challenging stage of the project.

In addition, since 2D SAW elastography is presented in this study, it is interesting to show the 3D elastography of a volume for better localisation of the skin lesions.

Laser safety issues

The initial idea of this project is to use laser to induce SAW on soft tissues, as it can offer a very broad band SAW signal which covers all the skin layers. The laser safety is of great importance and needs to be studied. We will conclude the most suitable

laser pulse optics to induce SAW on human tissues from FE simulation. The pulse laser should not cause burn or thermal-chemical reactions. The laser must be safe to irradiate soft tissue sample and able to induce SAW with detectable amplitude. The laser energy level will restrain in class 3, which will not cause burn to skin tissue. Beside the FE simulation, experiments are also required to observe the tissue thermal reaction to laser pulse. This can be achieve by applying different kinds of laser pulse to different samples of tissue mimicking phantoms and Thiel cadaver, and record the temperature increasing distribution by using a thermal camera. The increased temperature will be strictly monitored and controlled into 2 K. For the *in vivo* human skin tissue, it considers to apply a thin film to shield the thermal affect to skin.

Clinical studies

The ultimate aim of this work is the development of a system which can be used in the clinical diagnosis of scleroderma and to monitor changes in the various stages of skin cancers or scleroderma treatment and therefore clinic trials are crucial. The trial would consist of patients recruited from the dermatology unit and skin involvement monitored for skin disease progression using the current systems and comparing the results with established methods of skin measurement including biopsy and clinical skin scoring methods.

References

1. Gennisson J., Baldeweck T. T., Catheline M. S., Fink M., Sandrin L., Cornillon C. and Querleux B. (2004) “Assessment of Elastic Parameters of Human Skin Using Dynamic Elastography” IEEE transactions on ultrasonics, ferroelectrics, and frequency control, Vol. 51, issue. 8, pp. 908-989.
2. Agache P. G., Monneur C., Leveque J. L. and De Regal J., “Mechanical Properties and Young’s Modulus of Human Skin in vivo” Arch. Dermatol. Res., Vol. 269, pp. 221-232.
3. Zhang X., Kinnick R. R., Pittelkow M. R. and Greenleaf J. F. (2008) “Skin viscoelasticity with surface wave method” 2008 IEEE International Ultrasonics Symposium Proceedings, paper. 0156.
4. "Melanoma skin cancer," American Cancer Society, (2011) http://www.cancer.org/acs/groups/cid/documents/webcontent/003120-pdf.
5. "Skin cancer," American Cancer Society, (2007) http://www.cancer.org/acs/groups/content/@nho/documents/document/skincancerpdf.pdf.
6. Ciarletta P., Foret L. and Ben Amar M. (2010) "The radial growth phase of malignant melanoma: multi-phase modelling, numerical simulations and linear stability analysis," Journal of The Royal Society Interface, Vol. 8, issue. 56, pp. 345-368.
7. Tilleman T. R., Tilleman M. M. and Neumann M. H. (2004) "The elastic properties of cancerous skin: Poisson's ratio and Young's modulus," Isr Med Assoc J., Vol. 6, issue. 12, pp. 753-755.
8. Williams M. and Ouhtit A. (2005) "Towards a Better Understanding of the Molecular Mechanisms Involved in Sunlight-Induced Melanoma," J Biomed Biotechnol., Vol. 2005, issue. 1, pp. 57-61.
9. Allen A. C. and Spitz S. (1953) "Malignant melanoma; a clinicopathological analysis of the criteria for diagnosis and prognosis," Cancer 6(1), 1-45 (1953).
10. Sun C., Standish B. and Yang V. X. (2011) "Optical coherence elastography: current status and future applications," J Biomed. Opt., Vol. 16, issue. 4, pp. 043001.
11. Evans A., Whelehan P., Thomson K., McLean D., Brauer K., Purdie C., Jordan L., Baker L. and Thompson A. (2010) "Quantitative shear wave ultrasound elastography: initial experience in solid breast masses," Breast Cancer Res., Vol. 12, issue. 6, pp. R104.
12. Rago T., Santini F., Scutari M., Pinchera A. and Vitti P. (2007) "Elastography: new developments in ultrasound for predicting malignancy in thyroid nodules," J Clin Endocrinol Metab, Vol. 92, issue. 8, pp. 2917-2922.
13. Rivaz H., Boctor E. M., Choti M. A. and Hager G. D. (2011) "Real-time regularized ultrasound elastography," IEEE Trans Med Imaging, Vol. 30, issue. 4, pp. 928-945.
14. Venkatesh S. K., Yin M., Glockner J. F., Takahashi N., Araoz P. A., Talwalkar J. A. and Ehman R. L. (2008) "MR elastography of liver tumors: preliminary results," AJR Am J Roentgenol, Vol. 190, issue. 6, pp. 1534-1540.
15. McKnight A. L., Kugel J. L., Rossman P. J., Manduca A., Hartmann L. C. and Ehman R. L. (2002) "MR elastography of breast cancer: preliminary results," AJR Am J Roentgenol, Vol. 178, issue. 6, pp. 1411-1417.

16. Schneider D. and Schwarz T. A. (1997) “Photoacoustic method for characterising thin films,” Surface and Coatings Tech., Vol. l91, pp. 136-146.
17. Wang H. S., Fleming S., Law S., Huang T. (2006) “Selection of Appropriate Laser Parameters for Launching Surface Acoustic waves on Tooth Enamel for Non-Destructive hardness Measurement,” in Proceedings of IEEE Australian Conference of Optical Fibre Technology/Australian Optical Society (ACOFT/AOS).
18. Huang Q. J., Cheng Y., Liu X. J., Xu X. D. and Zhang S. Y. (2006) “Study of the elastic constants in a La0.6Sr0.4MnO3 film by means of laser-generated ultrasonic wave method” Ultrasonics, Vol. 44, Supp. 1, pp. e1223-e1227.
19. Reverdy F. and Audoin B. (2001) “Ultrasonic measurement of elastic constant of anisotropic materials with laser source and laser receiver focused on the same interface” J. Appl. Phys., Vol. 90, no. 9, pp. 4829-4835.
20. Ridgway P., Russo R., Lafond E., Jackson T. and Zhang X. (2004) “A Sensor for Laser Ultrasonic Measurement of Elastic Properties during Manufacture”, in Proceedings of 16th WCNDT 2004 - World Conference on NDT, paper 466.
21. Scruby C. S. and Drain L. E. (1990) Laser Ultrasonics: Techniques and Applications, ISBN-10: 0750300507, Taylor & Francis, London, pp. 325-335
22. Tilleman T. R., Tilleman M. M. and Neumann M. (2004) "The elastic properties of cancerous skin: Poisson's ratio and Young's modulus”, IMAJ, Vol. 6, pp. 753-755.
23. Nakajima M., Kiyohara Y., Shimizu M. and Kobayashi M. (2007) "Clinical application of real-time tissue elastography on skin lesions", MEDIX Suppl., pp. 36-39.
24. Gawkrodger D. J. (2002) Dermatology, An Illustrated Colour Text. 3rd Ed., ISBN-10: 0443104212, Edinburgh: Churchill Livingstone, pp. 15-9.
25. Burns D. A., Breathnach S. M., Cox N. and Griffiths C. E. (2004) Rook's testbook of Dermatology 7th Ed., ISBN: 9780632064298, Oxford UK. Blackwell Publishing, pp. 120-123.
26. Machie R. M. (2004) Clinical dermatology 4th Ed., ISBN: 978-1-118-69350-6, New York, New York. Oxford Press, pp. 134-146.
27. Standring S. (2006) Gray's Anatomy, ISBN-10: 0914294083, Elsevier Mosby, pp. 365-374.
28. Richard W., Hunter J., Savin J. and Dahl M (2008) Clinical Dermatology, 4th Ed. ISBN: 978-1-118-69350-6, Sussex UK. Blackwell Publishers, pp. 345-8.
29. Agner, T. (1995) “Ultrasound A-mode measurement of skin-thickness” In: Serup, J. and Jemec, G.B.E. (eds.) Handbook of Non-Invasive Methods and the skin, ISBN: 9780849314377, Boca Raton, CRC Press, pp. 567-9.
30. Alberts B., Bray D., Johnson A., Lewis J., Raff M., Roberts K., and Walter P. (1998) “Essential Cell Biology” pp. 601. Garland.
31. Anonymous (2003) “What are skin diseases [online]”. Available from: http://www.wisegeek.com/what-is-skin-disease.htm.
32. Clements P. L., Lachenbruch P. A., Seibold J. R., Zee B., Steen V. D., Brennan P., Silman A. J., Allegar N., Varga J. and Massa M. (1993) “Skin thickness score in systemic sclerosis: an assessment of interobserver variability in 3 independent studies-Calculation of the modified Rodnan Score”, J Rheumatol, Vol. 20, issue. 11, pp. 1892-6.
33. Boring C. C., Squires T. S. and Tong T. (1991) "Cancer statistics, 1991". SA Cancer Journal for Clinician, Vol. 41, issue. 1, pp. 19–36.

34. Jerant A. F., Johnson J. T., Sheridan C. D., Caffrey T. J. (2000) "Early Detection and Treatment of Skin Cancer". American Family Physician, Vol. 62, issue. 2, pp. 357–68, 375–6, 381–2.
35. Balch C., Buzaid A., Soong S., Atkins M., Cascinelli N., Coit D., Fleming I., Gershenwald J., Houghton A., Kirkwood J., McMasters K., Mihm M., Morton D., Reintgen D., Ross M., Sober A. and Thompson J. (2001) "Final version of the American Joint Committee on Cancer staging system for cutaneous melanoma". J Clin Oncol, Vol. 19, issue. 16, pp. 3635–48.
36. Halachmi S., Gilchrest B. A. (2001) "Update on genetic events in the pathogenesis of melanoma". Curr. Opin. Oncol., Vol. 13, issue. 2, pp. 129–136.
37. Tilleman T. R., Tilleman M. M. and Neumann M. (2004) "The elastic properties of cancerous skin: Poisson's ratio and Young's modulus" IMAJ, Vol. 6, pp. 753-755.
38. Kennedy B. F., Hillman T. R., McLaughlin R. A., Quirk B. C. and Sampson D. D. (2009) "In vivo dynamic optical coherence elastography using a ring actuator" OPTICS EXPRESS, Vol. 17, no. 24, pp. 21762-21772.
39. Chan R. C., Chau A. H., Karl W. C., Nadkarni S., Khalil A. S., Iftimia N., Shishkov M., Tearney G. J., Kaazempur-Mofrad M. R. and Bouma B. E. (2004) "OCT-based arterial elastography: robust estimation exploiting tissue biomechanics" Opt. Express, Vol. 12, issue. 19, pp. 4558–4572.
40. Balbir-Gurman A., Denton C. P., Nichols B., Knight C. J., Nahir A. M., Martin G. and Black C. M. (2002) "Non-invasive measurement of biochemical skin properties in Systemic Sclerosis" Ann Rheum Dis., Vol. 61, pp. 237-241.
41. Vlachoyiannopoulos P. G. (2011) "System sclerosis",Orphanet encyclopaedia, https://www.orpha.net/data/patho/GB/uk-SSc.pdf.
42. Le Roy E. C. "Systemic sclerosis (scleroderma)", Cecil's Testbook of Medicine, Bennet, J. C., Plum F. (eds), 20th Edition, Philadelphia.
43. Gilliland B. C. (1998) "Systemic sclerosis (scleroderma)", Harrisson's Princples of internal Medicine, Fauci AS et al (eds), 14th Edition, New Youk, McGraw-Hill.
44. Anonymous (2004) Microbial Diseases of the Skin and Eyes [online]. Available from: http://classes.midlandstech.edu/carterp/courses/bio225/chap21/ss1.htm.
45. Beuthan J., Minet O., Helfmann J., Herring M., and Muller G. (1996) "The spatial variation of the refractive index in biological cells" Physics in Medicine and Biology, Vol. 41, pp. 369–382.
46. Bevilacqua F. and Depeursinge C. (1999) "Monte carlo study of diffuse reflectance at sourcedetector separations close to one transport mean free path" Journal of Optical Society of America, Vol. 16, pp. 2935–2945.
47. Boissieux L., Kiss G., Thalman N., and Kalra P. (2000) "Simulation of skin aging and wrinkles with cosmetics insight" Europraphics Workshop on Animation and Simulation, pp. 15–28.
48. Bruls W. A. G. and van der Leun J. C. (1984) "Forward scattering properties of human epidermal layers" Photochemistry and Photobiology, Vol. 40, pp. 231–242.
49. Brunsting A. and Mullaney P. (1972) "Light scattering from coated spheres: model for biological cells" Applied Optics, Vol. 11, pp. 675–680.
50. Chan E. K., Sorg B., Protsenko D., O'Neil M., Motamedi M., and Welch. A. J. (1996) "Effects of compression on soft tissue optical properties" IEEE Journal of Selected Topics in Quantum Electronics, Vol. 2, pp. 943–950.
51. Chen B., Stamnes K., and Stamnes J. J. (2001) "Validity of the diffusion approximation in bio-optical imaging" Applied Optics, Vol. 40, pp. 6356–6366.

52. Chung J. H., (2003) “Photo aging in Asians” Photo immunol. Phtomed., Vol. 19, pp. 109–121.
53. Claridge E., Cotton S., Hall P., and Moncrieff M. (2002) “From colour to tissue histology: physics based interpretation of images of pigmented skin lesions”, Medical image computing and computer assisted intervention, pp. 730–738.
54. Cook R. L. and Torrance K. E. (1982) “A reflectance model for computer graphics” ACM Transactions on Graphics, Vol. 1, issue. 1, pp.7–24.
55. Corcuff P., Leveque J. L., Grove G. L., and Kligman A. M. (1987) “The impact of aging on the microrelief of peri-orbital and leg skin” Journal of the Society of Cosmetic Chemists, Vol. 82, pp. 145–152.
56. Arda K., Ciledag N., Arıbas B. K., Aktas E., and Köse K. (2013) "Quantitative assessment of the elasticity values of liver with shear wave ultrasonographic elastography", Indian J Med Res., Vol. 137, issue. 5, pp. 911–915.
57. Rami K. K. and Simo S. (2011) “Biomechanics and Modeling of Skeletal Soft Tissues”, Theoretical Biomechanics, Dr Vaclav Klika (Ed.), ISBN: 978-953-307-851-9, InTech.
58. Liu J., Craig K. Michael A., Insana F. (2004) “Linear Approach to Axial Resolution in Elasticity Imaging”. IEEE Trans Ultrason Ferroelectr Freq Control, Vol. 51, issue. 6, pp. 716–725.
59. Diridollou S., Patat F., Gens F., Vaillant L., Black D., Lagarde J. M., Gall Y. and Berson M. (2000) “In Vivo Model of The Mechanical Properties Of the Human Skin Under Suction” Skin Res and Technol., Vol. 6, pp. 214-221.
60. Dobrev H.P (2002) “Mechanical Properties in Other Dermatological Diseases, Bioengineering of the Skin” Skin Biomechanics, pp .215-228.
61. Wang Q. and Hayward V. (2006) “In vivo biomechanics of the finger pad skin under local tangential traction,” J. Biomech., Vol. 40, pp. 851–860.
62. Diridollou S., Black D., Lagarde J. M., Gall Y., Berson M., Vabre V., Papat F., and Vaillant L. (2000) “Sex- and site-dependent variations in the thickness and mechanical properties of human skin in vivo” Int. J. Cosmet.Sci., Vol. 22, pp. 421–435.
63. Escoffier C., de Rigal J., Rochefort A., Vasselet R., Leveque J. L., and Agache P. G. (1989) “Age-related mechanical properties of human skin: An in vivo study” J. Invest. Dermatol., Vol. 93, pp. 353–357.
64. Oxlund H., Manschot J., and Viidik A. (1988) “The role of elastin in the mechanical properties of skin” J. Biomech., Vol. 21, pp. 213–218.
65. Pereira J. M., Mansour J. M., and Davis B. R. (1991) “Dynamic measurement of the viscoelastic properties of skin,” J. Biomech., Vol. 24, pp. 157–162.
66. Kirkpatrick S. J., Duncan D. D., and Fang L. (2004) “Low-frequency surface wave propagation and the viscoelastic behaviour of porcine skin” J. Biomed. Opt., Vol. 9, pp. 1311–1319.
67. Khatyr F., Imberdis C., Vescovo P., Varchon D., and Lagarde J.M. (2004) “Model of the viscoelastic behaviour of skin in vivo and study of anisotropy” Skin Res. Technol., Vol. 10, pp. 96–103.
68. Liang X. (2010) “Coherence Imaging Technologies for the Measurement of Tissue and Cell Biomechanics”, PhD Thesis, University of Illinois at Urbana-Champaign.
69. Yock P. G. (2001) “Intravascular ultrasound: novel pathophysiological insights and current clinical applications” Circulation, Vol. 103, pp. 604–616.
70. Yock P. G., and Fitzgerald P. J. (1998) “Intravascular ultrasound: State of the art and future directions,” American Journal of Cardiology, Vol. 71, no. 7A, pp. 27E–32E.

71. Oralkan O., Hansen S., Bayram B., Yaralioglu G. G., Ergun A. S. and Khuri-Yakub B. T. (2004) “High-frequency cMUT arrays for high-resolution medical imaging,” presented at the IEEE Intl. Ultrason. Symp., Montreal, Canada.
72. Querleux B. (1995) “Nuclear Magnetic Resonance (NMR) examination of the epidermis in vivo” In: Serup, J. and Jemec, G.B.E. (eds.) Handbook of Non-Invasive Methods and the skin. Boca Raton, CRC Press.
73. Ginefri J., Darasse L. and Crozat P. (2011) “High-temperature superconducting surface coil for in vivo microimaging of the human skin” Magnetic Resonance in Medicine, Vol. 45, pp. 376–382.
74. Zemtsov A. (1995) “Nuclear Magnetic Resonance (NMR) examination of the skin” In: Serup, J. and Jemec, G.B.E. (eds.) Handbook of Non-Invasive Methods and the skin. Boca Raton, CRC Press.
75. Barral J. K., Bangerter N. K., Hu B. S. and Nishimura D. G. (2010) “In vivo high-resolution magnetic resonance skin imaging at 1.5 T and 3 T” Magn Reson Med., Vol. 63, issue. 3, pp. 790–796.
76. Sun C., Standish B. and Yang V. X. D. (2011) "Optical coherence elastography: current status and future applications", J. Biomed. Opt., Vol. 16, pp. 043001.
77. Nischal K. C. and Khopkar U. “Dermoscope”, Department of Dermatology, Seth GS Medical College & KEM Hospital, Parel, Mumbai - 400012, India.
78. Ashfaq A., Marghoob A., Lucinda D., Swindle A., Claudia Z. and Moricz M. (2003) “Instruments and new technologies for the in vivo diagnosis of melanoma” J am acad dermatol, New York.
79. Nehal K. S., Gareau D. and Rajadhyaksha M., (2008) “Skin Imaging with Reflectance Confocal Microscopy” Sem. Cutan. Med. Surg., Vol 27, pp. 37-43.
80. Elgeti T., Laule M., Kaufels N., Schnorr J., Hamm B., Samani A., Braun J., and Sack I. (2009) "Cardiac MR elastography: comparison with left ventricular pressure measurement," J Cardiovasc Magn Reson., Vol. 11, pp. 44.
81. Rago T., Santini F., Scutari M., Pinchera A., and Vitti P. (2007) "Elastography: new developments in ultrasound for predicting malignancy in thyroid nodules," J Clin Endocrinol Metab, Vol. 92, pp. 2917-2922.
82. Pellot-Barakat C. (2004) “Ultrasound Elastography Based on Multiscale Estimations of Regularized Displacement Fields”, IEEE Transactions on medical imaging, Vol. 23, no. 2, pp. 153-163.
83. Gao L., Parker K. J., Lerner R. M. and Levinson S. F. (1996) “Imaging of the elastic properties of tissue- A review”, Ultrasound in Med. & Bio., Vol. 22, no. 8, pp. 959-977.
84. Luo J., Bai J., Wang W., Cui L. and J. W, (2006) “An experimental system for ultrasound elastography”, Chinese Journal of Scientific Instrument, Vol. 27, no. 5, pp. 541-550.
85. Taylor L. S., Porter B. C., Rubens D. J. and Parker K. J. (2000) “Three-dimensional sonoelastography: principles and practices”, Phys. Med. Biol, Vol. 45, pp. 1477-1494.
86. Morikawa H. and Kawada N. (2011) "The Current Status of Non-Invasive Assessment of Liver Fibrosis: Real Time Tissue Elastography", under CC BY-NC-SA.
87. Lindop J. E., Treece G. M., Gee A. H. and Prager R. W. (2005) “3D elastography using freehand ultrasound”, Academic Press, CUED/F-INFENG/TR, pp. 531.
88. University of Kuopio, “Ultrasound elastography”, seminar LUT2.
89. Luo J. and Bai J. (2003) “The principle and theoretical analysis of ultrasound elastograpgy”, International Biomedical, Vol. 26, issue. 3, pp. 97-102.

90. Zhao Z. and Luo B. (2008) “The principle and techniques of ultrasound elastography”, Medical instrument information of China, Vol. 14, issue. 4, pp. 5-8
91. Lee F., Bronson J. P., Lerner R. M., Parker K. J., Huang S. and Roach D. J. (1991) “Sonoelasticity imaging: Result in vitro specimens”, Radiology, Vol. 181, pp. 237-239.
92. Gao L., Parker K. J. and Alam S. K. (1995) “Elasticity imaging: Theory and experimental verification”, J. Acoust. Soc. Am, Vol. 97, no. 6, pp. 3875-3886.
93. Parker K. J., Fu D., Graceswki S. M., Yeung F., and Levinson S. F. (1998) “Vibration sonoelastography and the delectability of lesions”, Ultrasound in Med. & Biol., Vol. 24, no. 9, pp. 1437-1447.
94. Catheline S., Thomas J., Wu F. and Fink M. A. (1999) “Diffraction Field of a low frequency vibrator in soft tissue using transient elastography”, IEEE Transactions on Ultrasounics, Ferroelectrics, and frequency control, Vol. 46, no. 4, pp. 1013-1019.
95. Catheline S., Wu F. and Fink M. (1999) “A solution to different biases in sonoelasticity: The acoustic impulse technique”, J. Acoust. Soc. Am, Vol. 105, no. 5, pp. 2941-2950.
96. Sandrin L., Tanter M., Gennisson J., Catheline S. and Fink M. (2002) “Shear elasticity probe for soft tissue with 1-D transient elastography”, IEEE Transactions on Ultrasounics, Ferroelectrics, and frequency control, Vol. 49, no. 4, pp. 436-446.
97. Sarvazyan A. P. (1995) “Biophysical bases of elasticity imaging,” Acoust. Imaging, vol. 21, pp. 223–240.
98. Zhao Z. and Luo B. (2008). “Application of Ultrasonic Elastography Beside Breast Diseases”, Information of China medical instrument, Vol. 14, no. 4, pp. 9-12.
99. Pallwein L., Aigner F., Faschingbauer R., Pallwein E., Pinggera G., Bartsch G., Schaefer G., Struve P. and Frauscher F. (2008) “Prostate cancer diagnosis: value of real-time elastography”, Abdom Imaging, Vol. 33, pp. 729-735.
100. Krouskop T.A., Dougherty D.R., Vinson F.S. (1987) “A pulsed Doppler ultrasonic system for making noninvasive measurements of the mechanical properties of soft tissue” Journal of Rehabilitation Research, Vol. 24, pp. 1–8.
101. Schmitt C., Soulez G., , Maurice R. L., Giroux M. F. and Cloutier G., (2007) “Noninvasive vascular elastography: toward a complementary characterization tool of atherosclerosis in carotid arteries” Ultrasound Med. Biol, Vol. 33, issue. 12, pp. 1841–1858.
102. Schmitt C., Henni A. H., and Cloutier G. (2008) “ Dynamic micro-elastography applied to the viscoelastic characterization of a mimicking artery and a porcine aorta. ,” in Proc. of IEEE Ultrasonics Symp, pp. 643–646.
103. Schmitt J. M., Bao X., and Xiao S. (1999) “Micro-elastography of tissue with OCT” Proc. SPIE. 3598, pp. 47–55.
104. Adams S. B. Jr., Roberts M. J., Patel N. A., Plummer S., Rogowska J., Stamper D. L., Fujimoto J. G. and Brezinski M. E. (2003) “The use of polarization sensitive optical coherence tomography and elastography to assess connective tissue. ,” Conf. on Lasers and Electro-Optics, CLEO '03, pp.1–6.
105. Ford M., Dupps W. J., Huprikar N., Lin R., and Rollins A. M. (2006) “OCT corneal elastography by pressure-induced optical feature flow,” Proc. SPIE. 6138, pp. 1–7.
106. Liang X., Oldenburg A. L., Crecea V., Chaney E. J. and Boppart S. A. (2008) “Optical micro-scale mapping of dynamic biomechanical tissue properties. ,” Opt. Express, Vol. 16, pp. 11052–11065.

107. Chan R. C., Chau A. H., Karl W. C., Nadkarni S., Khalil A. S., Iftimia N., Shishkov M., , Tearney G. J., , Kaazempur-Mofrad M. R. and Bouma B. E., (2004) “OCT-based arterial elastography: Robust estimation exploiting tissue biomechanics. ,” Opt. Express, Vol. 12, pp. 4558–4572.
108. Liang X., Oldenburg A. L., Crecea V., Chaney E. J. and Boppart S. A. (2008) "Optical micro-scale mapping of dynamic biomechanical tissue properties," Opt Express, Vol. 16, issue. 15, pp. 11052-11065.
109. Wang R. K., Kirkpatrick S. and Hinds M. (2007) "Phase-sensitive optical coherence elastography for mapping tissue microstrains in real time," Appl Phys Lett, Vol. 90, issue. 16, pp. 164105-164103.
110. Kennedy B. F., Hillman T. R., McLaughlin R. A., Quirk B. C., and Sampson D. D. (2009) “In vivo dynamic optical coherence elastography using a ring actuator”, OPTICS EXPRESS, Vol. 17, issue. 24, pp. 21762-21772.
111. Kennedy B. F., Liang X., Adie S. G., Gerstmann D. K., Quirk B. C., Boppart S. A., and Sampson D. D., (2011) “In vivo three-dimensional optical coherence elastography”, Optical express, Vol. 19, issue. 7, pp. 6623-6634.
112. Bloch S. and Hales A.L. (1968) “New techniques for the determination of surface wave phase velocities”, Bulletin of the Seismological Society of America, Vol. 58, issue. 3, pp. 1021-1034.
113. Abbiss C. P. (1981) “Shear wave measurements of the elasticity of the ground”, Geotechnique, Vol. 31, pp. 91-104.
114. Clorennec D., Royer D., Walaszek H. (2002) “Nondestructive evaluation of cylindrical parts using laser ultrasonic”, Ultrasonics, Vol. 40, pp. 783-789..
115. White R. M. (1963) "Generation of Elastic Waves by Transient Surface Heating," Journal of Applied Physics, Vol. 34, pp. 3559-3567.
116. Yang J., DeRidder N., Ume C. and Jarzyniski J. (1993). "Non-contact Optical Fiber Phased Array Generation of Ultrasound for Nondestructive Evaluation of Materials and Processes," Ultrasonics, Vol. 31, issue. 6, pp. 387-394.
117. Coté G. L., Rastegar S. and Wang L. V. (2000) "Introduction to Biomedical Optics and Lasers," in Introduction to Biomedical Engineering, J. Enderle, S. Blanchard, and J. Bronzino, eds., pp. 843-903.
118. Wang H.C, Fleming S., Lee Y-C, Law S., Swain M. and Xue J. (2009) “Laser Ultrasonic surface wave dispersion technique for non-destructive evaluation of human dental enamel”, Optics Express, Vol. 17, issue. 18, pp. 15592-15607.
119. Ophir J., Cespedes I., Ponnekanti H., Yazdi Y. and Li X. (1991) “Elastography—a quantitative method for imaging the elasticity of biological tissues,” Ultrason. Imaging, Vol. 13, issue. 2, pp. 111–134.
120. Aki K., Richards P.G. (1980) “Quantitative seismology. Theory and methods” W.H. Freeman and Company.
121. Davies S. J., Edwards C., Taylor G. S., and Palmer S. B. (1993) "Laser-generated ultrasound: its properties, mechanisms and multifarious applications", Journal of Physics D: Applied Physics, Vol. 26, issue. 3I, pp. 329.
122. Krautkramer J., Krautkramer H. (1990) “Ultrasonic Testing of Materials” Berlin, Heidelberg, New York (Fourth Edition), Vol.13-14, pp. 533-534.
123. Balogun O., Huber R., Chinn D. and Spicer J. B. (2009) “Laser ultrasonic inspection of the microstructural state of thin metal foils”, J. Acoust. Soc. Am. Vol. 125, pp. 1437, DOI:10.1121/1.3068447.
124. Zhang H. F., Maslov K., Li M. L., Stoica G. and Wang L. V. (2006) "In vivo volumetric imaging of subcutaneous microvasculature by photoacoustic microscopy," Opt. Express Vol. 14, pp. 9317-9323.

125. Akesson A., Hesselstrand R., Scheja A. and Wildt M. (2004) “Longitudinal development of skin involvement and reliability of high frequency ultrasound in systemic sclerosis”, Ann. Rheum. Dis, Vol. 63, pp. 791-796.
126. Rittgers S.E., Putney W.N. and Barnes R.W. (1980) “Real-time spectrum analysis and display of directional Doppler ultrasound blood velocity signals” IEEE Trans. Biomed. Eng., BME-27, pp. 723–738.
127. Macé E., Montaldo G., Cohen I., Baulac M., Fink M. and Tanter M. (2011) "Functional ultrasound imaging of the brain", Nature Methods, Vol. 8, pp. 662–664,
128. Qiu Y., Huang Z., Slade A. and Thomson G. (2008) “Optimization of Ultrasonic Tool Performance in Surgery”, IFMBE Proceedings for ECIFMBE, Vol. 22, pp. 899-902.
129. Qiu Z., Gao J., Cochran S., Huang Z., Corner G. and Song C. (2009) "The development of therapeutic ultrasound with assistance of robotic manipulator," Engineering in Medicine and Biology Society, Annual International Conference of the IEEE, Vol. 3, issue. 6, pp. 733-736.
130. Kennedy J. E., Ter Haar G. R. and Cranston D. (2003) “High intensity focused ultrasound: surgery of the future?” The British Journal of Radiology, Vol. 76, pp. 590-599.
131. ter Haar G., Sinnett D., and Rivens I. H., (1989) “High-intensity focused ultrasound—a surgical technique for the treatment of discrete liver tumours.” Phys. Med. Biol., Vol. 34, pp. 1743-1750.
132. Xu M. and Wang L. V. (2006) "Photoacoustic imaging in biomedicine," Review of Scientific Instruments, Vol. 77, pp. 0411011–22.
133. Huang F., Maurudis A., Gamelin J., Aguirre A., Castillo D., Guo P. and Zhu Q. (2007) “A fast photoacoustic imaging system based on a curved ultrasound transducer array”, IEEE, pp. 47-48.
134. Park S., Aglyamov S. R. and Emelianov S. Y. (2007) “Beam forming for photo-acoustic imaging using linear array transducer”, IEEE Ultrasonics Symposium, pp. 856-859.
135. Wang Y. and Wang R. K. (2008) “Photoacoustic recovery of an absolute optical absorption coefficient with an exact solution of a wave equation”, Phys. Med. Biol, Vol. 53, pp. 6167-6177.
136. Kong F., Chen Y. C., Lloyd H. O., Silverman R. H., Kim H. H., Cannata J. M., and Shung K. K. (2009) “High-resolution photoacoustic imaging with focused laser and ultrasonic beams”, Applied Physics Letters, Vol. 94, pp. 033902.
137. Stein E. W., Maslov K., and Wang L. V. (2009) "Noninvasive, in vivo imaging of the mouse brain using photoacoustic microscopy," Journal of Applied Physics, Vol. 105, issue. 10, pp. 10202701–10202705.
138. Zhang E. Z., Laufer J. G., Pedley R. B. and Beard P. C. (2009) “In vivo high-resolution 3D photoacoustic imaging of superficial vascular anatomy”, Phys. Med. Biol., Vol. 54, pp. 1035-1046.
139. Wang B., Su J. L., Amirian J., Litovsky S. H., Smalling R., Emelianov S. (2010) “Detection of lipid in atherosclerotic vessels using ultrasound-guided spectroscopic intravascular photoacoustic imaging”, OPTICS EXPRESS, Vol. 18, issue. 5, pp. 4889-4897.
140. Fang H., Maslov K. and Wang L. V. (2007) “Photoacoustic Doppler flow measurement in optically scattering media”, Applied Physics Letters, Vol. 91, pp. 264103.

141. Sivaramakrishnan M., Maslov K., Zhang H. F., Stoica G. and Wang L. V. (2007) "Limitations of quantitative photoacoustic measurements of blood oxygenation in small vessels," Physics in Medicine and Biology, Vol. 52, issue. 5, pp. 1349–1361.
142. Li P. C., Huang S. W., Wei C. W., Chiou Y. C., Chen C. D., and Wang C. R. C. (2005) "Photoacoustic flow measurements by use of laser-induced shape transitions of gold nanorods", Optics Letters, Vol. 30, issue. 24, pp. 3341-3343.
143. Hu S., Maslov K., Wang L. V. (2009) "Noninvasive label-free imaging of microhemodynamics by optical-resolution photoacoustic microscopy", Optics Express, Vol. 17, issue. 9, pp. 7688-7693.
144. Povolo F. and Bolmaro R.E. (1983) "On the measurement of Young's modulus of tubes by propagation of longitudinal waves, Journal of Nuclear Materials", Vol. 116, issue. 2-3, pp. 166-171.
145. Sato M., Ishihara M., Kikuchi M. and Mochida J. (2011) "A Diagnostic System for Articular Cartilage Using Non-Destructive Pulsed Laser Irradiation", Lasers in Surgery and Medicine, Vol. 43, pp. 421-432.
146. Gao G., Yang S., and Xing D. (2011) "Viscoelasticity imaging of biological tissues with phase-resolved photoacoustic measurement", Optics Letters, Vol. 36, issue. 17, pp. 3341-3343.
147. Bercoff J., Tanter M. and Fink M. (2004) "Supersonic shear imaging: a new technique for soft tissue elasticity mapping," Ultrasonics, Ferroelectrics and Frequency Control, IEEE Transactions on, Vol. 51, issue. 4, pp. 396-409.
148. Deffieux T., Montaldo G., Tanter M. and Fink M. (2009) "Shear Wave Spectroscopy for In Vivo Quantification of Human Soft Tissues Visco-Elasticity", Medical Imaging, IEEE Transactions on, Vol. 28, issue. 3, pp. 313 – 322.
149. Nordez A. and Hug Fr. (2010) "Muscle shear elastic modulus measured using supersonic shear imaging is highly related to muscle activity level", Journal of Applied Physiology, Vol. 108, issue. 5, pp. 1389-1394.
150. Chen S., Urban M.W., Pislaru C., Kinnick R. and Greenleaf J.F. (2009) "Liver elasticity and viscosity quantification using shearwave dispersion ultrasound vibrometry ", Conf Proc IEEE Eng Med Biol Soc., pp. 2252-5.
151. Nightingale K., Mcaleavey S. and Trahey G. (2003) "Shear-Wave Generation Using Acoustic Radiation Force: In Vivo and Ex Vivo Results", Ultrasound in Med. & Biol., Vol. 29, issue. 12, pp. 1715-1723.
152. Sato Y. Y and Sato T. J, (1990) "Ultrasonic imaging of internal vibration of tissue under forced vibration". IEEE Trans. Ultrason. Ferroelec. Freq. Contr., Vol. 37, issue. 2, pp. 45-53.
153. Greenleaf J. F., Fatemi M., and Insana M., (2003) "Selected Methods for Imaging Elastic Properties of Biological Tissues", Annu. Rev. Biomed. Eng. Vol. 5, pp. 57-78.
154. Sarvazyan A. P., Rudenko O. V., Swanson S. D., Fowlkes J. B., and Emelianov S. Y. (1998) "Shear Wave Elasticity Imaging: a New Ultrasonic Technology of Medical Diagnostics", Ultrasound in Med. & Biol., Vol. 24, issue. 9, pp. 1419-1435.
155. Scruby C. S. and Drain L. E. (1990) "Laser Ultrasonics: Techniques and Applications".
156. Neubrand A. and Hess, P. (1992) "Laser generation and detection of surface acoustic waves: Elastic properties of surface layers" J. Appl. Phys., Vol. 71, issue. 1, pp. 227-238.

157. Schneider D. and Schwarz T. A. (1997) “Photoacoustic method for characterising thin films” Surface and Coatings Tech., Vol. l91, pp. 136-146.
158. Zhang X., Osborn T. G., Pittelkow M. R., Qiang B., Kinnick R. R. and Greenleaf J. F. (2011) “Quantitative assessment of scleroderma by surface wave technique”, Medical Engineering & Physics, Vol. 33, issue. 1, pp. 31-37.
159. Zhang X., Qiang B., Hubmayr R. D., Urban M. W., Kinnick R. and Greenleaf J. F. (2011) “Noninvasive ultrasound image guided surface wave method for measuring the wave speed and estimating the elasticity of lungs: A feasibility study.” Ultrasonics, Vol. 51, issue. 3, pp. 289-295.
160. Zhang X. M., Qiang B. and Greenleaf J. (2011) "Comparison of the surface wave method and the indentation method for measuring the elasticity of gelatin phantoms of different concentrations", Ultrasonics, Vol. 51, issue. 2, pp. 157-164.
161. Ruiz A. and Nagy P. B. (2003) “SAW dispersion measurements for ultrasonic characterization of surface treated metals” Measurement and Metrology, Vol.3, pp. 59-85.
162. Mi B., Michaels J. E. and Michaels T. E. (2005) “An ultrasonic method for dynamic monitoring of fatigue crack initiation and growth” J. Acoust. Soc. Am., Vol. 119, issue. 1, pp. 74-85.
163. Herrmann J., Kim J. Y. and Jacobs L. J. (2006) “Assessment of material damage in a nickel-base superalloy using nonlinear Rayleigh surface waves” Journal of Applied Physics, Vol. 99, pp. 124913.
164. Glorieux C., Gao W. M. and Kruger S. E., (2000) “Surface acoustic wave depth profiling of elastically inhomogeneous materials” Journal of Applied Physics, Vol. 88, pp. 4394-4400.
165. Xu B.Q., Shen Z.H. and Lu J. (2003) “Numerical simulation of laser-induced transient temperature field in film-substrate system by finite element method” International Journal of Heat and Mass Transfer, Vol. 46, pp. 4963–4968.
166. Xu B. Q., Shen Z. H., Ni X. W. (2004) “Finite element model of laser-generated surface acoustic waves in coating-substrate system” Journal of Applied Physics, Vol. 95, issue. 4, pp. 2109-2115.
167. L'Etang A. and Huang Z. Y. (2006) “FE simulation of laser generated surface acoustic wave propagation in skin”, Ultrasonics, Vol. 44, Suppl. 1, pp. e1243-e1247.
168. L'Etang A. and Huang Z. Y. (2005) “FE simulation of laser ultrasonic surface waves in a biomaterial model”, Appl. Mech. Mater. Vol. 3, issue. 4, pp. 85-90.
169. Agache P. G., Monneur C., Leveque J. L. and De Regal, J. (1980) “Mechanical Properties and Young’s Modulus of Human Skin in vivo”, Arch. Dermatol. Res., Vol. 269, pp. 221-232.
170. Li C. H., Huang Z. H. and Wang R. K. K. (2011) "Elastic properties of soft tissue-mimicking phantoms assessed by combined use of laser ultrasonics and low coherence interferometry," Opt Express, Vol. 19, issue. 11, pp. 10153-10163.
171. Li C., Guan G., Reif R., Huang Z. and Wang R. K. (2011) "Determining elastic properties of skin by measuring surface waves from an impulse mechanical stimulus using phase-sensitive optical coherence tomography," Journal of The Royal Society Interface, doi: 10.1098/rsif.2011.0583.
172. Wang H. C., Fleming S., Lee Y. C., Law S., Swain M. and Xue J. (2009) “Laser ultrasonic surface wave dispersion technique for non-destructive evaluation of human dental enamel,” Optics Express., Vol. 17, issue. 18, pp. 15592-15607.
173. Wang H. C., Fleming S. and Lee Y. C. (2009) “Simple, all-optical, noncontact, depth-selective, narrowband surface acoustic wave measurement system for

evaluating the Rayleigh velocity of small samples or areas," Journal of Optical Society of America A., Vol. 48, issue. 8, pp. 1444-1451.
174. Li C., Guan G., Huang Z., Johnstone M., and Wang R. (2012) "Noncontact all-optical measurement of corneal elasticity," Opt. Lett., Vol. 37, pp. 1625-1627.
175. Brockenbrough R. L., "STRUCTURAL STEELS, STEELMAKING, AND FABRICATION", R. L. Brockenbrough & Associates, Inc.
176. Yuan L., Shi Y., Shen Z. and Ni X. (2008) "Laser-induced ultrasonic waves in steels with gradient changes in elastic property" Optics and Laser Technology, Vol. 40, pp. 325-329.
177. Dziewonski A., Bloch S. and Landisman M. (1969) "A technique for the analysis of transient seismic signals", Bulletin of the Seismological Society of America, Vol. 59, pp. 427-444.
178. Dziewonski A.M. and Hales A.L. (1972) "Numerical analysis of dispersive seismic waves", in: B.A. Bolt (eds), Methods in computational physics, ISBN: 978-0-12-460817-7, Elsevier, Academic Press, Vol.11, pp. 271-295.
179. Herman G.T. (1980) "Image reconstruction from projections, the fundamentals of computerized tomography", ISBN 978-1-84628-723-7, Academic Press, New York, pp. 210-234.
180. Herrmann R.B. (1973) "Some aspects of band-pass filtering of surface waves" Bulletin of the Seismological Society of America, Vol. 63, pp. 663-671.
181. Herrmann R.B. (1994) "SURF: surface wave inversion program", Saint Louis University.
182. Herrmann R.B. and Al-Eqabi G.I. (1991) "Surface wave inversion for shear velocity", in: J.M.Hoven (eds), Shear waves in marine sediments, ISBN: 978-94-010-5581-9, Kluwer Academic Publisher, pp. 545-556.
183. Herrmann R.B. (1996) "Computer programs in seismology: an overview on synthetic seismogram computation", User's manual, StLouis University, Missouri.
184. Herrmann R.B. and Wang C.Y. (1985) "A comparison of synthetic seismograms", Bulletin of Seismological Society of America, Vol. 75, pp. 41-56.
185. Nolet G. and Panza G.F. (1976) "Array analysis of seismic surface waves: limits and possibilities" Pure and Applied geophysics, Vol. 114, pp. 776-790.
186. McMechan G. A. and Yedlin M. J. (1981), "Analysis of dispersive wave by wave field transformation", Geophysics, Vol. 46, pp. 869-874.
187. Terada T. and Tsubio C., "Experimental studies on elastic waves Part I," A manuscript of earthquake research institude, Japan.
188. Nitta T., Haga H., Kawabata K., Abe K. and Sambongi T. (2000) "Comparing microscopic with macroscopic elastic properties of polymer gel" Ultramicroscopy, Vol. 82, pp. 223-226.
189. Pavan T., Madsen E., Frank G., Carneiro A. and Hall T. (2010) "Nonlinear elastic behavior of phantom materials forelastography", Phys. Med. Biol., Vol. 55, pp. 2679–2692.
190. Kirkpatrick S. J., Wang R. K., and Duncan D. D. (2006) "OCT-based elastography for large and small deformations" Opt. Express, Vol. 14, issue. 24, pp. 11585–11597.
191. Hurley D. H. and Spicer, J. B. (2004) "Line source representation for laser-generated ultrasound in an elastic transversely isotropic half-space" J. Acoust. Soc. Am., Vol. 116, issue. 5, pp. 2914-2922.
192. Kenderian S., Djordjevic B. B. and Green, Jr. R. E. (2011) "Point and Line Source Laser Generation of Ultrasound for Inspection of Internal and Surface Flaws in Rail and Structural Materials", Res Nondestr Eval., Vol.13, pp. 189-200.